THE DISSOLUTION RATE CONSTANT OF MAGNETITE IN AMMONIATED WATER AT 140 °C AND A $pH_{25°C}$ of 9.2

by

Aaron Turner

B.Sc. in Engineering, University of New Brunswick, 2017

A THESIS SUBMITTED IN PARTIAL FULFILLMENT OF THE REQUIREMENTS FOR THE DEGREE OF

Master of Science

In the Graduate Academic Unit of Chemical Engineering

Supervisor(s):	Derek H. Lister, PhD, Chemical Engineering
Examining Board:	Yonghao Ni , PhD, Chemical Engineering
	Huining Xiao, PhD, Chemical Engineering
	Gobinda Saha, PhD, Mechanical Enginering

This thesis is accepted by the
Dean of Graduate Studies

THE UNIVERSITY OF NEW BRUNSWICK

October, 2019

Abstract

Corrosion of carbon steel components is a major problem in the power generation industry and has been proved to be reliant on the protective magnetite oxide layer. Predicting the corrosion rates and material transport with the use of developed models has indicated the importance of a reliable value for the dissolution rate of magnetite at various chemistry conditions. In this study an impinging jet test section was placed in a high pressure recirculating water loop to measure the dissolution of sintered magnetite pellets made from synthesized magnetite powder. The dissolution experiments were conducted under typical power plant feedwater conditions in ammoniated water at $pH_{25^\circ C}$ 9.2. The addition of film-forming amines to the coolant was also studied to determine their effect on the dissolution rate of magnetite. The findings in this study can be used to understand and reduce the dissolution and removal of the protective magnetite oxide layer, which will reduce flow-accelerated corrosion rates, fouling of heat transfer surfaces due to material transport and the level of radioactivity in nuclear power plants due to the deposition of radioactive corrosion products outside of the core.

Acknowledgements

To begin, I would like to thank my supervisor, Dr. Derek H. Lister, for giving me the opportunity to work and learn under his supervision. Without his guidance and support, the success of this project would not have been possible.

I would like to thank the members of UNB Nuclear for their support during my time spent with the group. This project could not be completed without the help of Dr. Sarita Weerakul and Naravit Leaukosol during the construction of the experimental loop and their ongoing support.

I would like to thank Dr. Lihui Liu for the help she provided in performing the surface analysis of all experimental samples.

I would also like to thank Siddharth Raval for all the help in the development of the CFD model for the jet impingement study.

To my family and friends, thank you for your continuous care and support, telling me to do great things everyday and making this achievement possible.

Table of Contents

List of Tables

List of Figures

List of Symbols and Nomenclature

C_b	Concentration of metal in bulk flow, g/cm^3
C_{eq}	Magnetite equilibrium concentration (Solubility), g/cm^3
D_{AW}	Diffusivity, m^2/s
d_i	Diameter of spherical particle number i, m
d_0	Jet nozzle diameter, m
d_{20}	Surface mean diameter, m
d_{30}	Volumetric mean diameter, m
d_{32}	Volume/surface mean diameter, m
f	Weight proportion of iron in magnetite
g	Spalling time constant, $g{\cdot}Pa/cm^4$
H	Jet to pellet distance, m
k	Overall transfer coefficient, mm/s
k_d	Dissolution rate constant, mm/s
k_m	Mass transfer rate coefficient, mm/s
r	Radial distance from jet impingement region, m
$r_{corrosion}$	Corrosion rate, $g/m^2{\cdot}s$
$r_{removal}$	Overall removal rate, $g/m^2{\cdot}s$
Re	Reynolds number
Sc	Schmidt number

Sh	Sherwood number
t	Temperature, $^{\circ}C$
T	Absolute temperature, K
t_{total}	Total time of experiment, s
V_A	Molar volume of species A, cm^3/mol
θ	Spalling time, s
ρ	Density, kg/m^3
τ	Shear stress, Pa

Abbreviations

AVT	All Volatile Treatment
BWR	Boiling Water Reactor
CANDU	Canada Deuterium Uranium Reactor
CFD	Computational Fluid Dynamics
CHA	Cyclohexylamine
FAC	Flow-Accelerated Corrosion
FFA	Film-Forming Amine
FFAP	Film-Forming Amine Products
FFP	Film-Forming Products
LWR	Light Water Reactor
ODA	Octadecylamine
OLA	Oleylamine
OLDA	Oleyl Propylenediamine
PTFE	Polytetrafluoroethylene
SCC	Stress Corrosion Cracking
SEM	Scanning Electron Microscope

Chapter 1

Introduction

Corrosion is a major problem in the power generation industry, in both fossil fuel and nuclear power plants where catastrophic failures can cause millions of dollars per year. Flow-accelerated corrosion is prevalent in carbon steel components with high flow rates and is the typical cause of pipe failures. During operation in plant conditions (high temperature, high pressure and high flow rates), corrosion becomes a very serious financial and safety concern.

Flow-accelerated corrosion is found to be rapid enough in certain areas based on flow conditions that pipe walls can thin to unsafe levels, leaving a distinctive surface characteristic. A scalloped pattern is widely recognized as the typical morphology on the corroded surface by high flow-accelerated corrosion (FAC) rates in single phase flow. The development of scallops related to FAC can be linked to the corrosion process and depends on several factors: hydrodynamics, pH, temperature, dissolved oxygen, fluid velocity and hydrogen concentration. Although a turbulent flow condition can be closely related to the scalloped appearance, the detailed process of scallop development is not fully known [1].

Magnetite (Fe_3O_4) dissolution and deposition are major factors and a problematic

issue in the electrical power generation industry. Magnetite is the typical by-product produced by flow-accelerated corrosion of carbon steels in contact with high temperature water. This layer of magnetite is typically a few micrometers thick and acts as a protective layer that slows further corrosion of the underlying metal. It has been shown that the dissolution rate of magnetite, dependent on the concentration gradients from the oxide to the bulk fluid, is a critical factor in the mechanisms of flow accelerated corrosion. Therefore, a reliable value of magnetite dissolution rate is key to the modeling process of flow-accelerated corrosion at certain temperatures, pH's, and other flow conditions.

The transport and deposition of magnetite and other metal oxides have serious effects on the coolant systems. Fouling is a major problem due to these oxides on heat transfer surfaces causing a decrease in efficiency of the steam generator and leading to an overheating of reactor core fuel elements in nuclear plants. Nuclear power plants face the problematic issue of this material transport becoming activated in the core with deposition outside the core. This phenomenon increases the radiation field, requiring higher levels of shielding for safe reactor use.

There have been few studies of the dissolution rate constant of magnetite [3, 4, 5, 6]. The data are only available at a select few chemistry and flow conditions with large differences in the collected data. In this study, a high temperature loop was used to experimentally measure the dissolution rate constant of magnetite at a select few chemistry conditions at a temperature of 140°C and a $pH_{25^\circ C}$ of 9.2, controlled with ammonia. The addition of film-forming amines to the coolant was also studied to determine their effect on the dissolution rate of magnetite. An impinging jet flow was used over a synthesized magnetite pellet and the mass loss was determined with surface characterization techniques. Computational fluid dynamics was utilized to determine the flow characteristics over the magnetite pellet to understand the effects

on the development of surface dissolution and the surface characteristics due to high temperature jet flow.

The theoretical background, details on the experimental procedures, test runs and quantified results of measured dissolution rate constants are presented in the following chapters.

Chapter 2

Literature Review

2.1 Definition of Corrosion

Corrosion can be defined as the deterioration of a metal due to chemical or electrochemical reactions with the surrounding environment. Corrosion occurs due to the natural tendency of a metal to return to a natural state by a chemical reaction in the surrounding environment [7]. Metals typically corrode on contact with water, moisture in the air, acids, bases, salts, and other oxidizing liquids or gases. Metals are also found to corrode when exposed to gaseous materials like acid vapors, formaldehyde gas, ammonia gas and sulfur-containing gases. The best-known case is that of the rusting of steel.

There are many harmful effects caused by the corrosion of metals which include the loss of mechanical strength and structural integrity which can lead to failures, accidents and the loss of valuable materials such as pipes and other equipment.

2.2 Flow Accelerated Corrosion

Flow-accelerated corrosion (FAC) is a phenomenon that typically occurs in the electric power generation industry and is defined as the process whereby the normally protective oxide coating dissolves into a rapidly moving water or two-phase mixture. The oxide layer becomes thinner and less protective and the corrosion rate increases. Eventually, a steady state is reached where the corrosion and dissolution rates are equal and stable corrosion rates are maintained. The corroded surface typically exhibits a black color representative of the magnetite oxide layer [8].

The FAC process of carbon steel occurs under very specific environmental conditions such as temperature, pH, oxygen content, flow geometry and flow velocity (Reynolds number). This is primarily a corrosion process enhanced by electro-chemical dissolution and mass transfer, rather than a mechanical process. It is an accelerated process of the general carbon steel corrosion process in stagnant water. The situation is accelerated and enhanced due to turbulence within the flow (downstream of flow restrictors) that increases the flow rate at localized regions [9].

Corrosive conditions along the flow path and the mass transfer coefficient at the structure surface can be calculated to identify high-risk FAC risk zones. Figure 2.1 shows the overlapping parameters that join to form the high-risk FAC zone.

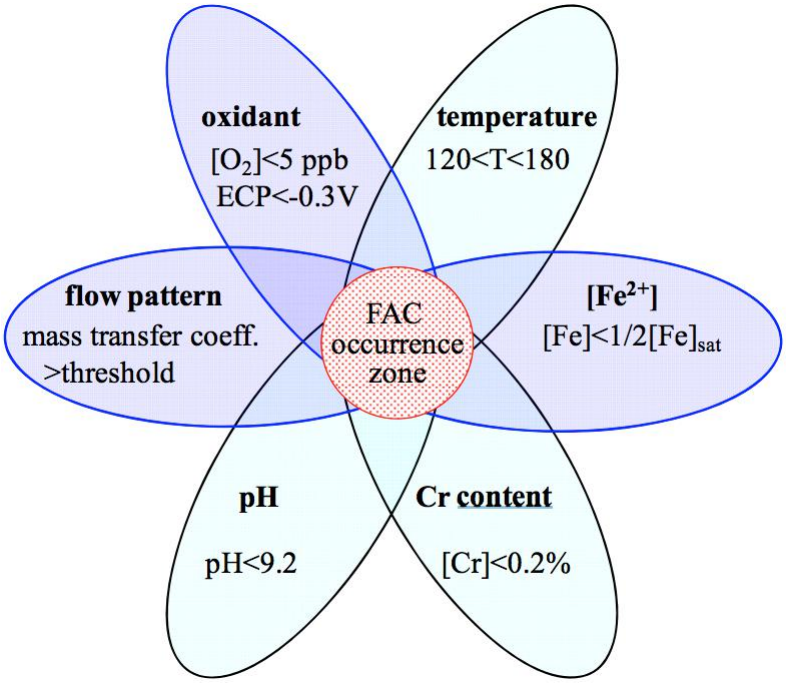

Figure 2.1: FAC risk zone [10]

2.3 Surface Scalloping

A scalloped pattern is widely recognized as the typical morphology on the corroded surface by high flow-accelerated corrosion (FAC) rates in single phase flow. Although a turbulent flow condition can be closely related to the scalloped appearance, the detailed process of scallop development is not fully known [1]. As the scallops begin to form the pipe surface roughness increases, which increases turbulence in the flow and causes an accelerated corrosion of the pipe. Scallops are influenced by the microscopic oxide structures that develop from the underlying metal grains; pearlite grains form lamellar oxides that predominate on scallop crests [11].

Elliptical concaves are formed in flows with low turbulence and low corrosion rates; concaves grow freely and without interference become the "horse-shoe type" scallops. However, in regions of higher corrosion rates, many elliptical concaves are formed,

and their growth is affected by neighboring concaves. The turbulence in these regions is increased, increasing the number of scallops but with smaller size and a shallow depth [1]. This indicates that the surface morphology of the pipe can be explained by the density of the elliptical concaves, which depends on the turbulence of flow inside the pipe.

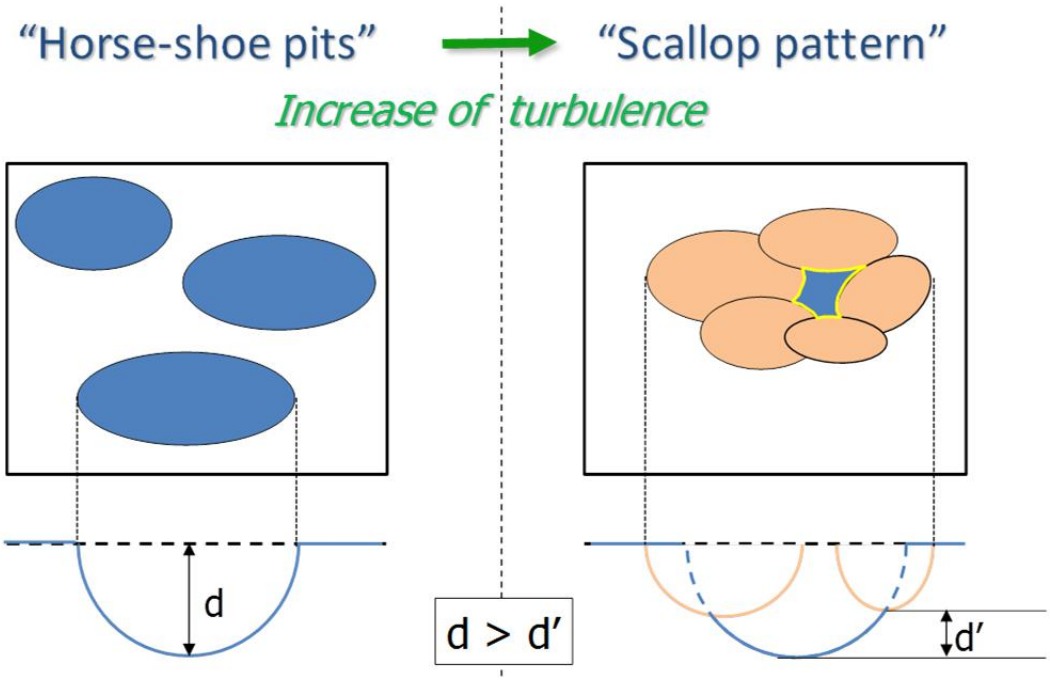

Figure 2.2: Schematic of scallop pattern development [1]

The passive bed theory of erosional marks assumes that the fundamental characteristics of the erosion marks are entirely determined by the dynamic properties of the fluid in contact with the surface. The properties of the material have therefore no influence on the formation of the scallops. The length of the erosion marks is assumed constant with time.

The defect theory assumes that the position of each erosional mark is due to the initial presence of an irregularity or a defect at the surface. It assumes an indepen-

dent evolution for each mark and an increase of length and amplitude with time, up to a limit set by the initial spacing of defects. Therefore, the characteristics of any collection of erosional marks depend on the duration of the eroding process, the spatial distribution, shape and dimensions of the defects and the character of the flow. The exact method for the development of scallops is still unknown but can be assumed to be independent of the substrates material if there is dissolution present.

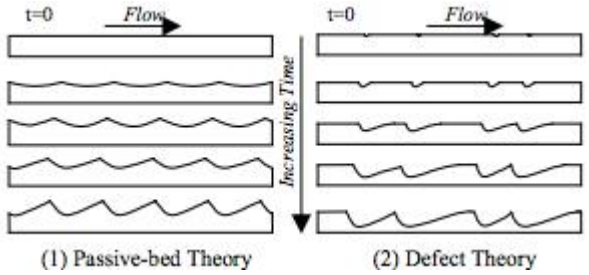

Figure 2.3: Evolution of surface according to passive-bed theory and defect theory [12]

Corrosion failures often occur in areas where the steady state flow patterns are disrupted, termed regions of disturbed flow. When the diffusion boundary layer is destroyed by the disrupted flow, the solution composition at the metal surface is close to that of the bulk solution. Fresh corrosives are brought into contact with the surface and corrosion products are swept away, modifying the steady-state process. This generates a kinetic disturbed condition and results in increased corrosion at the location of the flow disturbance. The steady state conditions for wall shear stress and mass transfer changes with a step change in the solids surface shown in Figure 2.4. This condition gives a disrupted hydrodynamic boundary layer and a disrupted diffusion boundary layer. A similar phenomenon is seen with a weld bead or defects on the pipe wall seen in Figure 2.5 or a pre-existing pit as seen in Figure 2.6 [13].

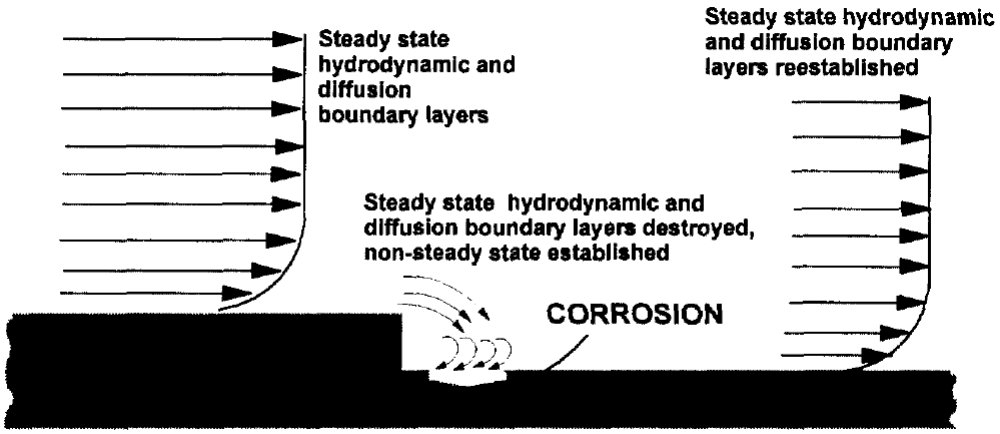

Figure 2.4: Flow over a step change [13]

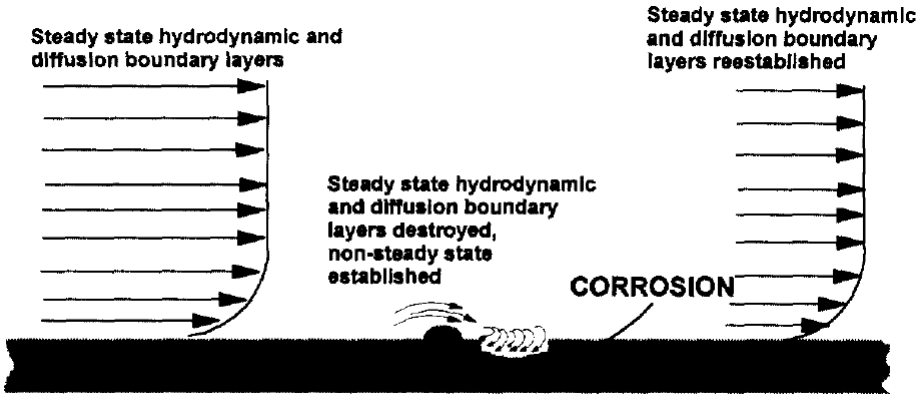

Figure 2.5: Flow over an internal weld bead [13]

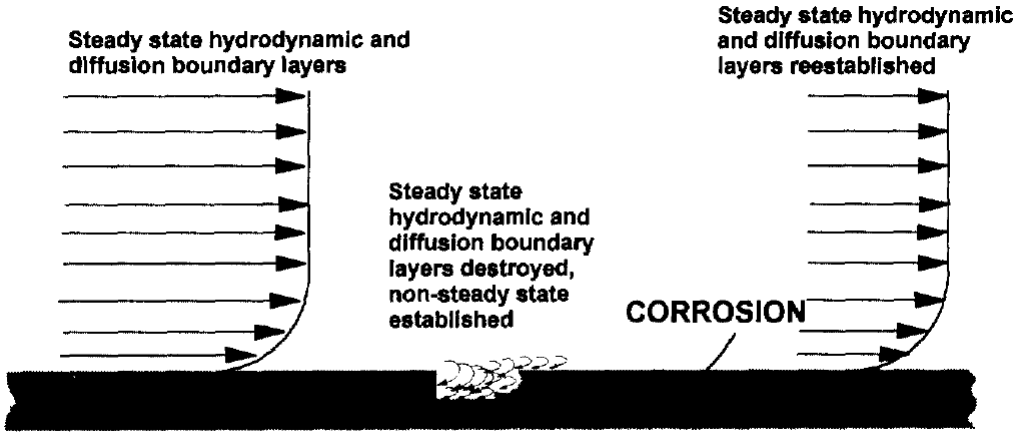

Figure 2.6: Disturbed wall shear stress and mass transfer coefficient [13]

Simulations have been completed by Bird with respect to the 1974 work from Blumberg and Curl on scallops in karst conduits. With the use of CFD, the flow in and above a scalloped surface was investigated as seen is in Figure 2.7.

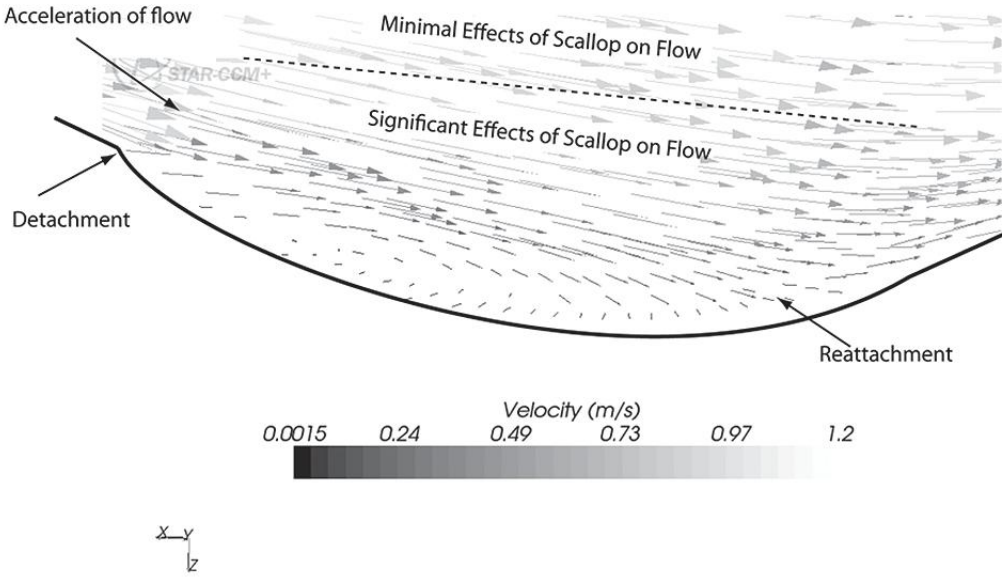

Figure 2.7: Vector plot flow in and above scallop [14]

The detachment of the flow in the scallop occurs where the acceleration is highest, which is at the leading edge. Reattachment occurs at a location approximately

2/3-scallop length downstream from the leading edge. Experimental observations suggest this to be the location where scallop propagation (significant dissolution) occurs within the scallop morphology [14].

2.4 Mechanisms of Carbon Steel Corrosion and the Effect of Magnetite

Carbon steel is the most used material in electrical power generating plants as CANDU reactor systems utilize carbon steel components for most of the primary and secondary coolant circuits. Fossil fuel plants also use carbon steel components for a majority of the boiler components and deal with corrosion related issues, similar to nuclear plants. Large corrosion rates of roughly 150 μm/a were observed in the outlet feeders of all CANDU-6 reactors in Canada with a coolant velocity between 8-16 m/s. This is far higher than the predicted rate of 10 μm/a or the corrosion rates observed in the inlet feeders, which led to further research on these high corrosion rates [15]. The corrosion of carbon steel in contact with high-temperature water with a low concentration of oxygen takes place with the attack of oxygen-bearing species at the metal/oxide interface. One of the earliest studies done on the magnetite oxide layer and the effect of corrosion was done by Potter and Mann [16], where a two-layer magnetite layer was found on the corroded carbon steel. The mechanism proposed for the development of these magnetite layers involves approximately half of the metal ions being neutralized by the oxygen-bearing anions at the metal/oxide interface and form the inner magnetite layer. The other half of the ferrous ions move outwards, and when the coolant becomes saturated with soluble iron, an outer magnetite layer precipitates to form the double oxide layer.

Castle and Masterson proposed that the corrosion process is controlled by the dif-

fusion of iron species in the solution contained in the pores of the oxide layer [17]. This model does not explain why the iron precipitates only on the outside layer and not within the pores. Bignold, Garnsey and Mann then proposed that the magnetite varies in stoichiometry across the oxide layer and is in equilibrium with iron in solution in the pores [18]. A diffusion gradient of soluble iron can then exist within the pores without pore blockage.

Robertson [19] looked at the problems with the solution-pores model and concluded that the observed pores in the magnetite oxide are much too small to account for the measured corrosion rates. The similar corrosion rates seen in water or steam systems could not be explained by this previous model and the Arrhenius activation energy for the corrosion process was much higher than typical diffusion process values. A new model, referred to as the "grain boundaries-pores" model was therefore proposed where the corrosion rate is controlled by the outward diffusion of ions along the grain boundaries. The oxygen-bearing species is transported to the metal/oxide interface due to the porous magnetite oxide. The growth of these magnetite layers has been reported to follow cubic or logarithmic kinetics. The species involved in the corrosion of carbon steel, with single layer magnetite oxide can be seen in Figure 2.8.

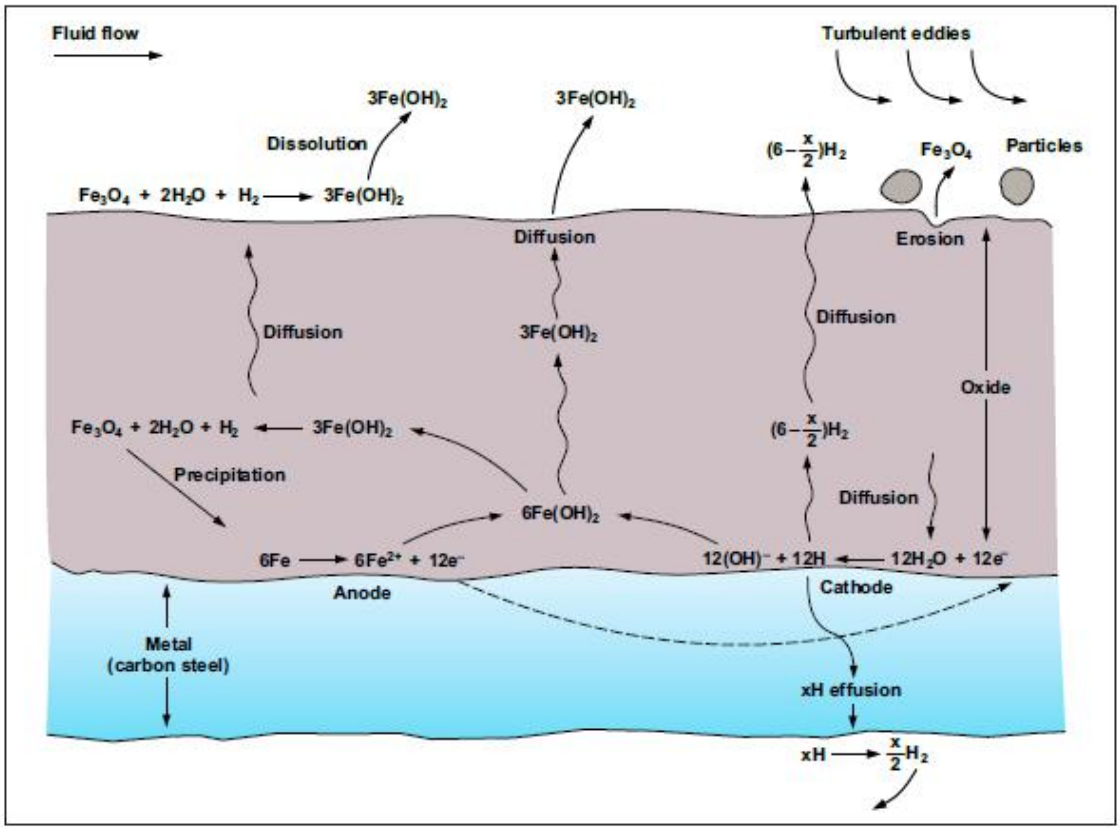

Figure 2.8: Schematic of the mechanism of FAC at steady-state, showing the associated stoichiometrically balanced chemical reactions and transport processes [20]

The formation of the duplex magnetite layer has been observed in the inlet feeders of CANDU reactors, at high temperature with alkaline chemistry conditions. The inner layer has a very small magnetite grain structure with an overall thickness of less than 1 μm but the outer magnetite layer shows magnetite crystals of 1 μm with an overall thickness of a few micrometers [21]. The outlet feeders of CANDU reactors were found to have only a single magnetite oxide layer due to the coolant not being saturated in iron species and therefore the outer layer will not precipitate. The single layer in the outlet feeders also correlates to a higher measured corrosion rate than the inlet feeder, suggesting that the magnetite acts as a protective layer for the carbon steel pipe.

Models have been developed to predict corrosion rates of carbon steel when dealing with flow-accelerated corrosion. Bignold et al. [22] produced a relatively simple model to predict FAC by accounting for the dissolution and mass transfer processes in series together. From this model the corrosion of carbon steel can be predicted from Equation 2.1.

$$r_{corrosion} = \frac{dm_{metal}}{dt} = \frac{(C_{eq} - C_b)}{\frac{1}{2k_d} + \frac{1}{k_m}} \tag{2.1}$$

Where $r_{corrosion}$, $\frac{dm_{metal}}{dt}$ is the corrosion rate (g/cm^2·s), C_{eq} is the equilibrium concentration of iron (g/cm^3), C_b is the concentration of iron in bulk solution (g/cm^3), k_d is the dissolution rate constant (cm/s) and k_m is the mass transfer coefficient (cm/s).

Lister et al. have developed a more in-depth model for the prediction of carbon steel corrosion rates under flow-accelerated conditions. The model includes the formation and removal of magnetite layers, electrochemical conditions, chemistry conditions, flow conditions at specific locations, and empirical terms including a term to predict erosion from spalling effects [23, 24]. The material effects can be taken into account with factors for the concentration of chromium, molybdenum and copper raised to powers less then one, with chromium having the largest impact. In both the models presented above to predict an accurate carbon steel corrosion rate, an accurate dissolution rate constant for each condition must be available from previous literature to create a working model.

2.5 Water Chemistry in Power Generating Plants

Controlling the coolant chemistry of power generating stations is vital in controlling important processes and to maintain the integrity of the plant systems. The major objective of water chemistry control is to reduce corrosion of power plant components,

to prevent fouling on heat transfer surfaces and the reduction of radioactive material transport to reduce occupational radiation exposure.

Fossil fuel power generating plants experience corrosion related issues as most of the boiler components are constructed from carbon steel. The coolant's chemistry for each type of boiler used in fossil fuel generating plants is shown in Table 2.1.

Table 2.1: Fossil fuelled electricty generating plant chemistry conditions [25]

	$pH_{25^\circ C}$	Conductivity (μS/cm)	O_2 (ppb)	Phosphate (mg/kg)
Low Pressure Boiler	10-10.5	-	<5	30-50
Medium Pressure Boiler	10-10.5	2500-10000	<5	10-20
High Pressure Boiler	9.5-10	<20	15	25-35
Makeup Water	7	<0.1	<10	0

Low-pressure boilers typically operate from 1.5-2 MPa with alkalinity being the controlling parameter to protect and to reduce corrosion. An excess in alkalinity can lead to scaling, which is reduced with the use of ion exchange resins. Medium-pressure boilers operate from 2-6 MPa and maintain a protective oxide layer by maintaining alkalinity with sodium hydroxide and by removing dissolved oxygen with the use of

hydrazine. High-pressure boilers operate over 6 MPa, but caustic gouging occurs when sodium hydroxide is used to control alkalinity due to high concentration factors of NaOH building up under the porous oxide deposit. To combat this corrosion problem, high-pressure boilers use either phosphates or an All Volatile Treatment (AVT) method that uses chemicals such as ammonia, morpholine and hydrazine to control the coolant's pH.

Nuclear power generating plants have different reactor types with varying chemistry conditions to optimize the working conditions of each reactor such as the Pressurized Water Reactor (PWR), Boiling Water Reactor (BWR) or the Canada Deuterium Uranium (CANDU). PWR's are a very common nuclear reactor design that are part of the Light Water Reactor (LWR) category as primary pressurized water (15.5 MPa) enters the reactor core at 275°C and exits at 325°C. Heat is transferred across the U-tubes in the steam generator to lower-pressure water that is turned to steam that powers the turbine to generate electricity. A diagram of the PWR design can be seen in Figure 2.9.

PWR primary coolant pH is controlled with a combination of lithium, by the addition of lithium hydroxide, and boron, by the addition of boric acid that is used to control neutron levels in the reactor core. The pH control arose from the necessity to minimize corrosion products in the primary coolant, which minimizes deposited radioactive material on surfaces and the crud on the fuel cladding. The optimum pH for the primary coolant is between 6.9-7.4 at 300°C. Hydrogen is added to the primary coolant to reduce oxygen production from water radiolysis to reduce stress corrosion cracking (SCC) of stainless steels in the primary circuit [27]. The PWR secondary side coolant chemistry is controlled by AVT with the addition of volatile amines like ammonia or hydrazine due to the two-phase coolant system. The addition of these chemicals is often optimized for a $pH_{25^{\circ}C}$ of 9.2 that minimizes corrosion

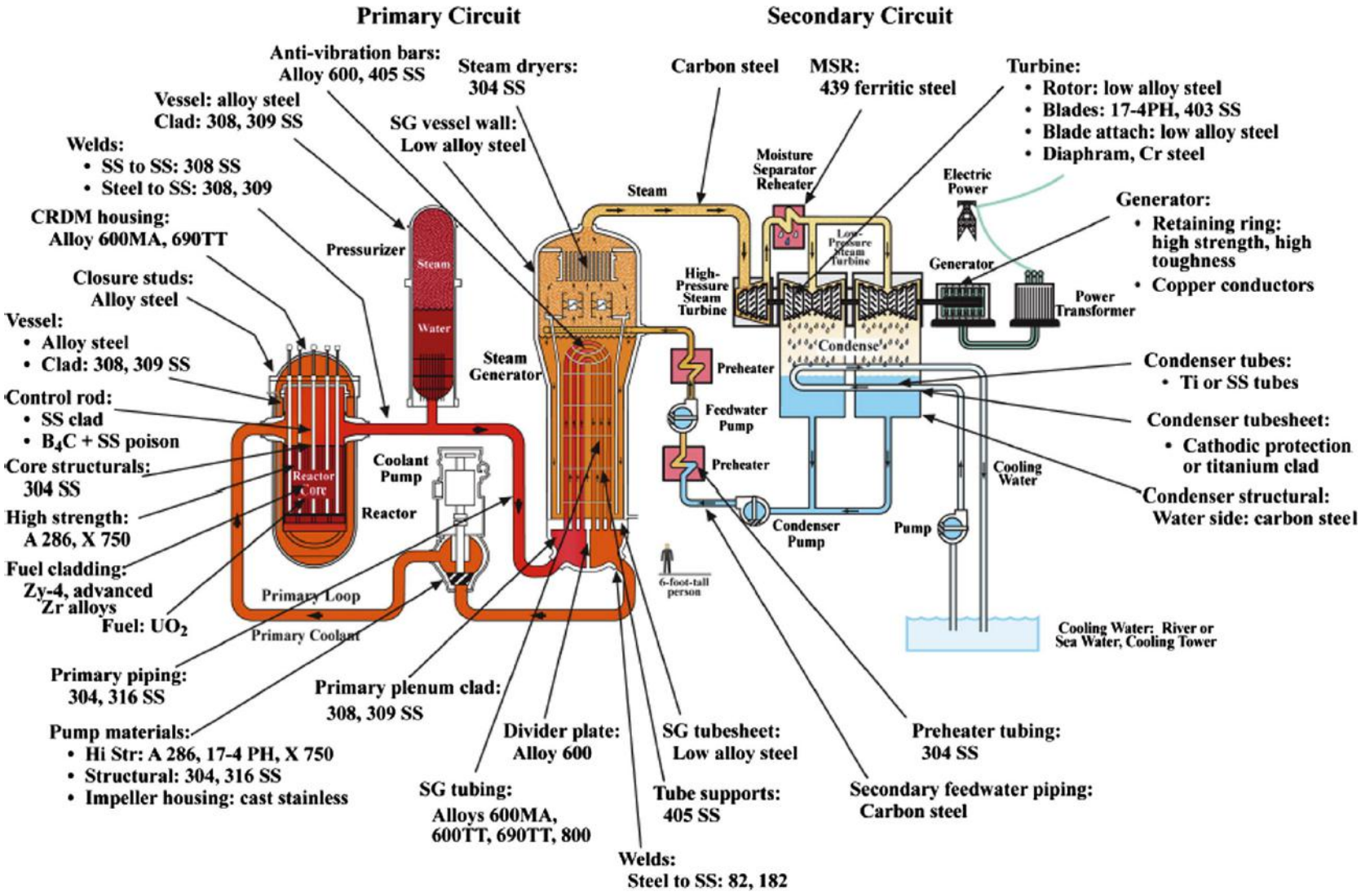

Figure 2.9: PWR plant diagram [26]

and crud build up on heat transfer surfaces.

CANDU reactors share many features with the PWR design except the primary coolant uses heavy water allowing the use of unenriched natural uranium fuel due to the heavy water not absorbing neutrons like light water. This change in the primary coolant system allows the pH to be controlled by only lithium. The pH of CANDU primary coolant system is maintained at 10.3 to reduce the corrosion of carbon steels where magnetite production becomes a system problem. A diagram of a CANDU reactor design can be seen in Figure 2.10.

BWR's operate with only a single coolant system and are designed to boil the light water in the reactor core before being transported to the turbines to generate electricity. This design feature allows the removal of steam generators and pressurizers seen in PWR designs. A BWR design diagram can be seen in Figure 2.11. Water purity control is important in BWRs to control out of core radiation levels, and due to the single coolant system radiation can spread through the entire plant. The pH is maintained between 6.8 to 7.2 with highly pure water with the addition of hydrogen, more recently, to reduce the radiolysis of water to reduce oxygen production and SCC [28]. The addition of zinc, oxygen and noble metals has also shown some improvements [25].

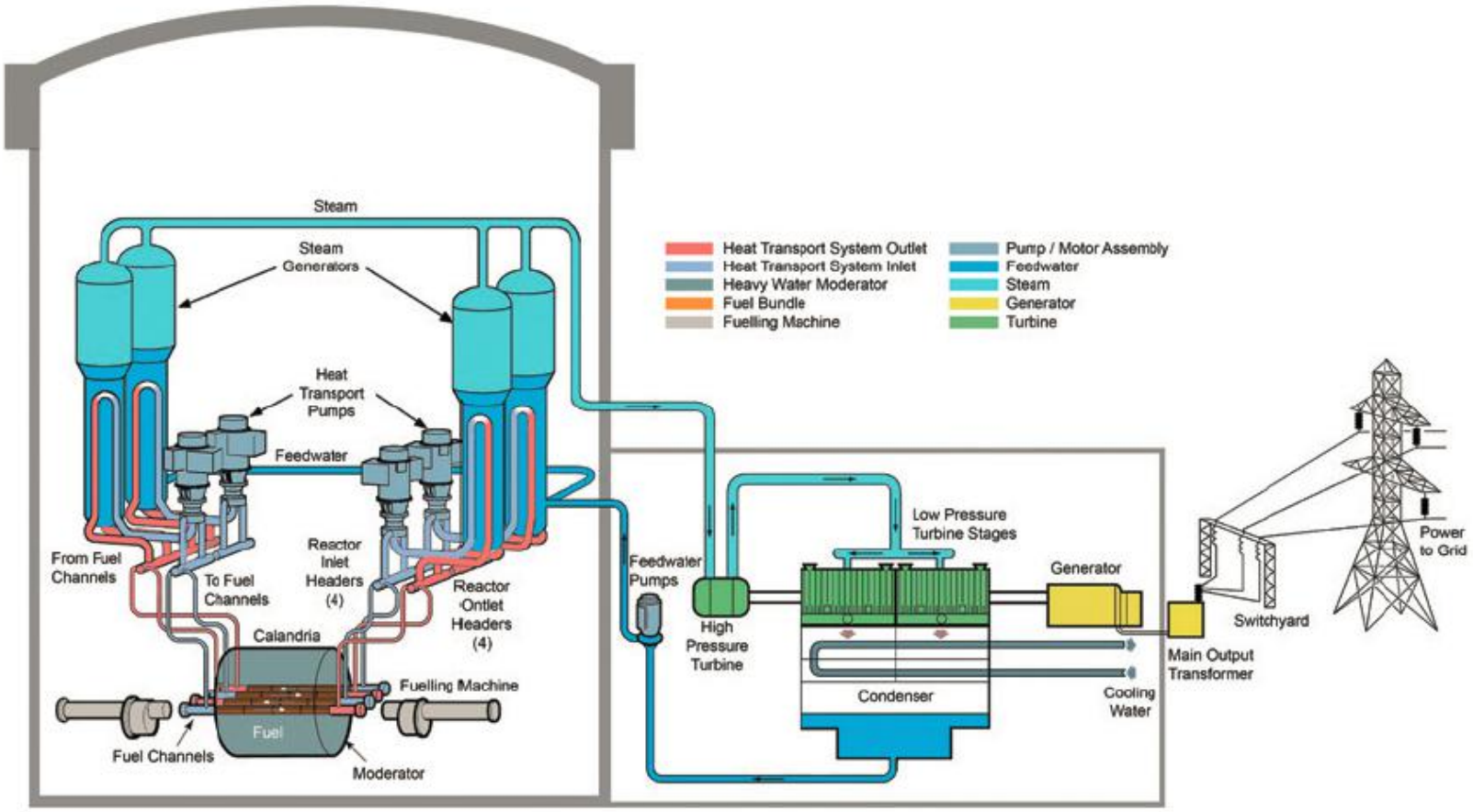

Figure 2.10: Simplified CANDU reactor design [29]

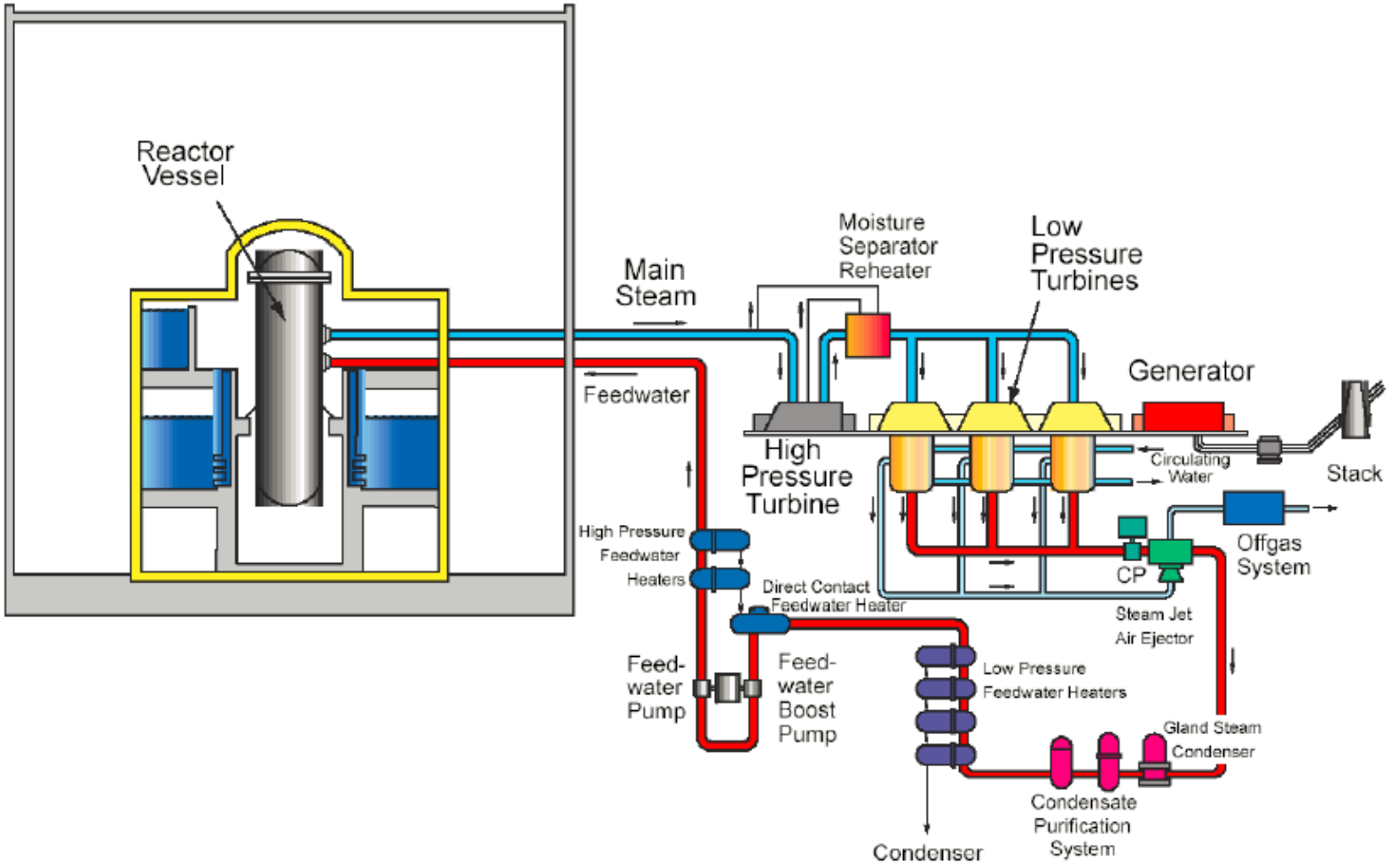

Figure 2.11: Simplified BWR reactor design [30]

2.6 Magnetite

Magnetite oxide typically denoted by Fe_3O_4 is one of the most commonly found ferromagnetic minerals on earth. It is a member of the inverse spinel class of minerals formulated by $A^{2+}B_2^{3+}O_4^{2+}$ and has a face-centered cubic structure [31]. Magnetite is typically recognized in flow-accelerated corrosion by the greyish/black color left on corroded surfaces. Magnetite is naturally ferromagnetic with a molecular weight of 231.54 g/mol, and an iron content of 72.4% and an average density of 5.2 g/cm^3. In the crystal structure of magnetite both divalent and trivalent iron ions are distributed between the octahedral and tetrahedral sites.

2.7 Magnetite Synthesis

Many different solutions for the synthesis of magnetite have been studied [32] to determine a simple and highly repeatable method for synthesizing high purity magnetite. Many parameters should be considered when comparing synthesized magnetite to the magnetite formed naturally due to corrosion in the electrical power generating industry. It is important that synthesized magnetite is monodisperse as the particle size can affect many mechanical (strength, hardness, etc.), magnetic and electrical properties. Sugimoto and Matijevic studied the parameters affecting crystal growth of magnetite and their effect on the particle size distribution [33].

One method studied by Matijević and Sugimoto [34] was an alternative sol-gel method. Magnetite particles form due to the aging, at 90°C in an oxygen-free environment, of a ferrous hydroxide gel formed from the interaction of ferrous sulfate with potassium hydroxide in the presence of nitrate ions. The final magnetite particle's size and size distribution were controlled by many experimental parameters

including temperature, time and concentrations. This method was used by a UNB study [35].

Lu [36] carried out a series of experiments to electrochemically deposit magnetite on an inert substrate from Fe_3O_4 solution. It was believed that this method was not a feasible solution for dissolution experiments as the film adherence and cohesion between magnetite particles could not withstand the erosion seen during these experiments. Hematite was also present in synthesized magnetite which suggests that this method does not produce highly pure magnetite [36].

Solid-phase reactions at high temperatures were found to produce the best results for synthesizing monodisperse magnetite [32]. The simplest dry (non-aqueous) method to produce magnetite, consists of heating a stoichiometric mixture of iron and hematite, according to Equation 2.2.

$$4Fe_2O_3 + Fe \longrightarrow 3Fe_3O_4 \tag{2.2}$$

This must occur under an inert atmosphere or in a vacuum to avoid oxidation of magnetite into hematite at high temperature. Iljinas and Tamulevičius [37] deposited thin layers of magnetite by annealing Fe_2O_3 and Fe multilayer in vacuum at 450°C for 120 minutes. De Pierrefeu [5] studied the parameters to synthesize spherical magnetite particles, from a solid-phase reaction to determine the influence of temperature, time and heating rate on the particle size and morphology. It was found that as the temperature increases above 600°C the particle shape deviates from sphericity due to non-uniform and anisotropic diffusion that leads to the formation of distinct faces on particles. The particle size also increases from 0.5 μm at 600°C to a wide range of larger particles (1 μm to 50 μm) at 1100°C. Temperature was found to be the dominant experimental factor as the heating rate and time of heating have

little efect over the particle size and shape.

2.8 Magnetite Solubility

In a study completed by Sweeton and Baes, the solubility of magnetite was measured in aqueous solutions saturated with H_2 at 1 atm with varying pH levels. The measurements were made by creating a continuous flow of solution over a bed of magnetite and then using a cation ion exchange to collect the dissolved iron ions. An equilibrium equation (2.3) was assumed where magnetite is in equilibrium with ferrous complexes. The solubility of the magnetite is then the sum of the ferrous species of Equation 2.3 in equilibrium with magnetite.

$$\frac{1}{3}Fe_3O_4 + (2-b)H^+ + \frac{1}{3}H_2(g) \longleftrightarrow Fe(OH)_b^{2-b} + (\frac{4}{3} - b)H_2O \tag{2.3}$$

where b = 0,1,2,3,4.

The equilibrium constant (K_b) for each value of b is related to the concentration of the involved species as shown in Equation 2.4.

$$K_b = \frac{[Fe(OH)_b^{2-b}]}{[H^+]^{2-b}[H_2]^{\frac{1}{3}}} \tag{2.4}$$

By using iteration and charge neutrality the distribution of species in equilibrium solution was determined. Figure 2.12 shows the total measured solubility of magnetite and the distribution of ferrous species [38].

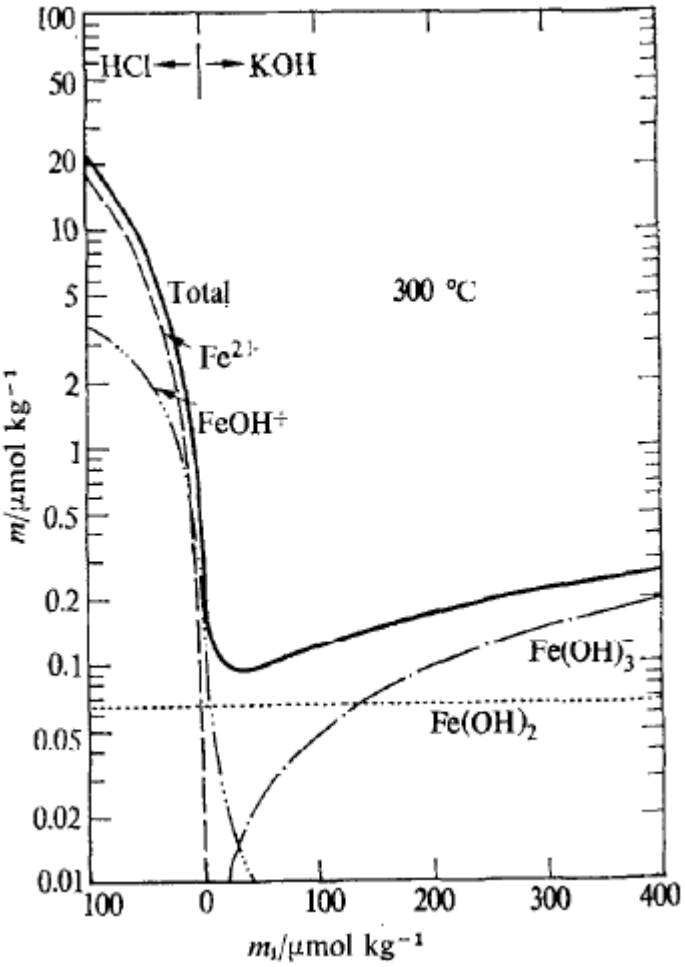

Figure 2.12: Distribution of species assuming only ferrous species are in equilibrium with magnetite [38]

Tremaine and Leblanc completed a similar study to that of Sweeton and Baes on the solubility of magnetite in dilute aqueous solutions saturated with H_2. The results were similar to those of the previous study at low pH, but at high pH the results were much lower than those achieved by Sweeton and Baes. They therefore assumed that the reaction in Equation 2.5 must also take place in addition to Equation 2.3 when calculating thermodynamic values and the distribution of ferrous species [39]. It is important to note that the magnetite solubility is dependent of H^+ solubility,

which is directly impacted by the dissociation of water.

$$\frac{1}{3}Fe_3O_4 + (3-b)H^+ \longleftrightarrow Fe(OH)_b^{3-b} + (\frac{4}{3}-b)H_2O + \frac{1}{6}H_2 \tag{2.5}$$

where b = 0,1,2,3,4.

The equilibrium constant (K_b) for each value of b is related to the concentration of the involved species as shown in Equation 2.6.

$$K_b = \frac{[Fe(OH)_b^{3-b}][H_2]^{\frac{1}{6}}}{[H^+]^{3-b}} \tag{2.6}$$

Figure 2.13 shows the comparison of the work completed by Tremaine and Leblanc against previous studies [39].

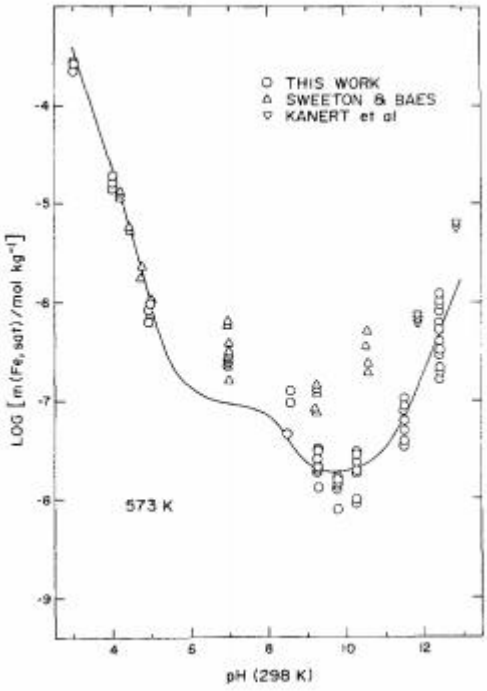

Figure 2.13: Experimental magnetite solubilities at 573 K in saturated H_2 [39]

2.8.1 Effect of pH

Magnetite solubility in previous studies has been found to rely greatly on the pH of the water. This can be seen from previously derived relationships seen in Equations 2.4 and 2.6 where H^+ is directly involved. In Figure 2.14 the magnetite solubility was found at a constant temperature with saturated H_2.

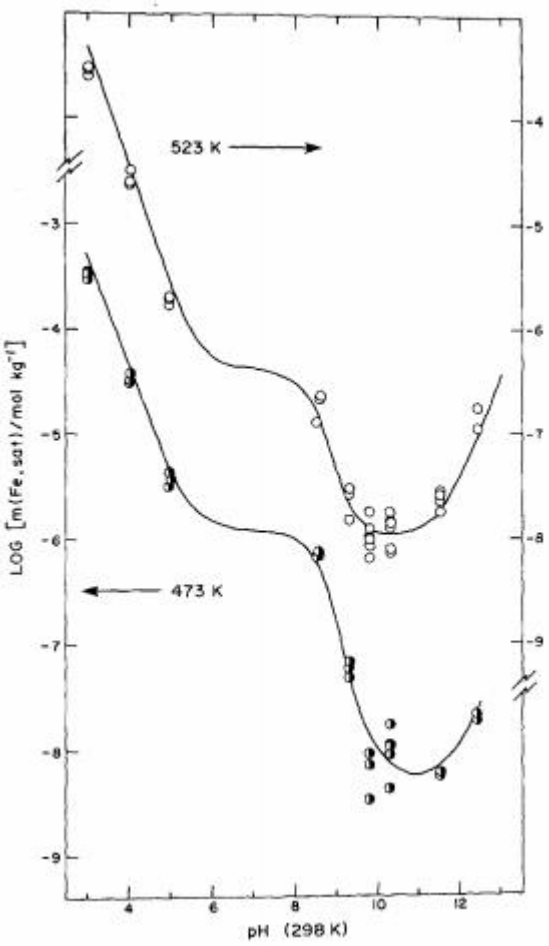

Figure 2.14: Experimental magnetite solubility values at varying pH levels at 473 and 523K [39]

It can be seen from Figure 2.14 that the solubility of magnetite is extremely depen-

dent on the pH as the solubility is found to increase as the feed water becomes more acidic. The solubility shows an almost constant value in regions of neutral pH (6-8) but decreases with more alkaline chemistry conditions. The solubility of magnetite is found to be a minimum in regions of $pH_{25^\circ C} \approx$10-11.5 depending on the temperature of the system. This is the area that corresponds to the lowest solubilities which correlates to the minimum corrosion rates by maximizing the effect of the protective oxide film. Due to these findings, the CANDU primary coolant pH is set somewhere in the optimal range based on the working fluid temperatures to reduce corrosion rates [39].

2.8.2 Effect of Temperature

Tremaine and LeBlanc also looked at the effect of temperature on the solubility of magnetite at constant pH with saturated H_2 seen in Figure 2.15.

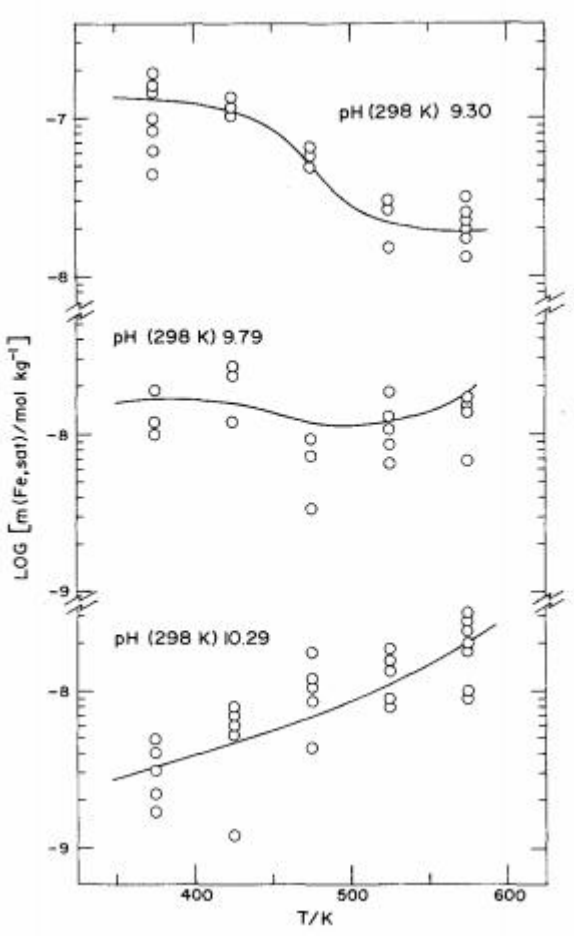

Figure 2.15: Experimental magnetite solubility at varying temperatures with constant pH [39]

From Figure 2.15 it is shown that at low pH values the magnetite solubility decreases as the working temperature increases. This trend begins to change at pH of 9.8, as the magnetite solubility remains constant as the temperature increases. As the pH increases above this value, the magnetite solubility increases with the increasing temperature [39].

2.8.3 Effect of Hydrogen

Studies have been completed by Berge on the effect of hydrogen on steel corrosion rates in high-temperature water. By assuming a constant pH and temperature system the equilibrium constant then becomes,

$$\frac{[Fe(OH)]_b^{2-b}}{[H_2]^{\frac{1}{3}}} \tag{2.7}$$

by removing the $[H^+]^{2-b}$ term. At constant pH and temperature, the solubility of magnetite becomes dependent on the third root of hydrogen partial pressure. The results found in this study agree with this hypothesis as a linear relation was found between $[H_2]^{1/3}$ and the concentration of soluble iron [40].

Tremaine and LeBlanc also looked at the effect of hydrogen on magnetite solubility. By assuming that both Equations 2.3 and 2.5 are involved in the dissolution of magnetite, they proposed Equation 2.8.

$$log\ m_2(Fe, sat) = log\ m_1(Fe, sat) + \frac{m_2(H_2)^{\frac{1}{3}} + \frac{1}{Km_2(H_2)^{\frac{1}{6}}}}{m_1(H_2)^{\frac{1}{3}} + \frac{1}{Km_1(H_2)^{\frac{1}{6}}}} \tag{2.8}$$

where m is the molarity and K is a constant determined by pH and temperature. They found a very weak influence of hydrogen partial pressure in the range of 1-11 atm on the solubility of magnetite [39].

2.9 Magnetite Dissolution

2.9.1 Magnetite Dissolution Measurements

There have been a few experimental studies investigating the kinetics of magnetite dissolution in high temperature and pressure systems. Three studies by Balakr-

ishnan [3], Tizzard et al. [4] and Thornton [41], all measured the dissolution of granular or powdered magnetite. Balakrishnan's technique consisted of passing high-temperature alkaline water, at a pH of 10.2-11 through a column packed with the magnetite oxide, that had been previously made radioactive by neutron irradiation. The solution was passed through another column, packed with a non-radioactive magnetite acting as an ion-exchanger. A representative sample of the magnetite from the second column was then counted in a Ge(Li) gamma spectrometer to determine the concentration of the dissolved magnetite. The water was pre-saturated with iron species and therefore the dissolution rate corresponds to an equilibrium condition. Tizzard et al. used a similar approach while considering variables such as temperature (200 to 317°C), hydrogen partial pressure (0 to 1 atm) and pH (5 to 11.6). Thornton used the same approach to study the dissolution rate of magnetite with a temperature range of 150°C to 300°C in 0.006 molar boric acid solution. The comparable data are from these studies are presented in Table 2.2.

Table 2.2: Magnetite dissolution rates from radiochemical techniques [3, 4, 41]

$pH_{25°C}$	Temperature(°C)	Dissolution Rate (g/cm^2s)		
		Balakrishnan	Tizzard	Thornton
5.76	150	-	-	2.08E-10
5.34	230	-	-	2.73E-11
5.32	300	-	-	1.46E-12
6.8	300	-	1.98E-10	-
7-7.5	300	-	1.77E-10	-
10.2	150	7.1E-14	-	-
10.2	200	2.3E-13	-	-
10.2	250	7.3E-13	1.25E-10	-
10.2	300	-	5.38E-10	-
10.3	250	-	1.6E-10	-
11.0	250	6.26E-13	-	-

These studies only considered the dissolution of powdered or granular magnetite, and not the cohesive magnetite films found in flow-accelerated corrosion and only considered equilibrium conditions when the coolant is fully saturated with iron species. Another method was implemented and refined by de Pierrefeu [5] that utilized an impinging jet with a recirculating water loop to measure the dissolution rate of sintered magnetite pellets. This method would provide high rates of mass transfer, allowing the dissolution to be the rate controlling process and to be easily measured. Mohajery [6] continued on the research by de Pierrefeu by studying the dissolution of magnetite at different coolant chemistry conditions. An attempt was made to measure the dissolution rate of magnetite at important CANDU operating conditions,

for use in the development of a flow-accelerated corrosion model. The dissolution rates of each study are presented in Table 2.3.

Table 2.3: Magnetite dissolution rates from jet impingement techniques [5, 6]

$pH_{25^\circ C}$	Temperature(°C)	Dissolution Rate (g/cm^2s)	
		de Pierrefeu	Mohajery
10.5	310	1.47E-11	
10.5	310	5.85E-11	
10.5	310	7.23E-11	
7	25	-	2.04E-9 ±4.37E-10
7	55	-	7.54E-9
7	140	-	2.45E-8
7	140	-	1.90E-8
9.2	140	-	3.50E-11
9.4	200	-	3.08E-10
10.4	265	-	6.52E-11

2.9.2 Magnetite Dissolution Rate Coefficient

Magnetite dissolution from a solid interface to a bulk solution consists of dissolution and mass transfer processes in series. The total process consists of the dissolution of magnetite from the surface into the fluid boundary layer, followed by the mass transfer of the dissolved species at the oxide-solution interface towards the bulk solution. The dissolution of magnetite can be said to be proportional to the difference between the magnetite solubility and the magnetite concentration at the oxide-solution inter-

face (first order model). The dissolution and mass transfer processes are described by equations 2.9 and 2.10 respectively.

$$r_{dissolution} = \frac{dm}{dt} = k_d(C_{eq} - C_{OS}) \tag{2.9}$$

$$r_{masstransfer} = \frac{dm}{dt} = k_m(C_{OS} - C_b) \tag{2.10}$$

When these two steps are in series and at steady state, the surface reaction and mass transfer rates are equal and the concentration differences can be added as in Equation 2.11.

$$C_{eq} - C_b = (C_{eq} - C_{OS}) + (C_{OS} - C_b) = \frac{1}{k_d}\frac{dm}{dt} + \frac{1}{k_m}\frac{dm}{dt} \tag{2.11}$$

Rearranging gives the overall removal process of Equation 2.12.

$$r_{removal} = \frac{dm}{dt} = k(C_{eq} - C_{OS}) \tag{2.12}$$

Where $r_{removal}$ is the overall removal rate (g/cm^2·s), k_d is the dissolution rate constant (cm/s), k_m is the mas transfer coefficient (cm/s) and k is the overall transfer coefficient (cm/s). C_{eq} is the solubility of magnetite, C_{OS} is the iron concentration at the oxide-solution interface and C_b is the iron concentration in bulk solution. The dissolution is related to the mass transfer coefficient and the overall transfer coefficient from Equation 2.13.

$$\frac{1}{k} = \frac{1}{k_d} + \frac{1}{k_m} \tag{2.13}$$

The overall removal of magnetite is therefore controlled by the slower process. This allows the use of a high-velocity jet impingement study to provide high mass transfer

rates, allowing the dissolution rate constant to be measured.

2.10 Impinging Jet Study

Jet impingement provides an experimental method to measure the important parameters related to flow-accelerated corrosion by providing high rates of heat and mass transfer. In this study, jet impingement is used to increase the mass transfer to an order of magnitude higher than the dissolution rate to ensure the mass transfer rate is not the limiting process in the overall removal of the magnetite sample. There are many different types of impinging jet studies depending on the nozzle shape (circular or slot), and if the jet is submerged or unsubmerged. A submerged jet consists of the fluid leaving the nozzle to a stagnant fluid which is often the same as the jet fluid while an unsubmerged jet is surrounded by gas. There have been many experimental studies completed utilizing jet impingement techniques with many numerical models to describe the flow characteristics and important mass/heat transfer rates.

2.10.1 Jet Flow Characteristics

The flow field created when a circular jet impinges on a flat surface with its central axis normal to the surface is shown in Figure 2.16.

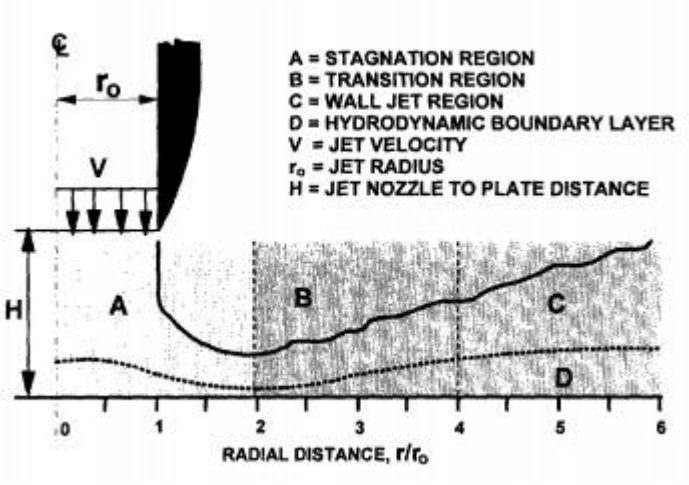

Figure 2.16: Hydrodynamic characteristics of submerged jet impingement on a flat plate [13]

The jet flow seen in Figure 2.16 can be separated into three distinct regions of interest beginning in Region A where the flow is in the stagnation region. The flow is laminar and produces a high-pressure region up to $r/r_0 = 2$, which is the area of maximum velocity. There are rapid changes in the flow that cause the region to be poorly defined based on wall shear stress. Region B (transition region) is a zone of rapidly increasing turbulence intensity, where the flow develops into the wall jet region. This occurs between $r/r_0 = 2$ to $r/r_0 = 4$ where the flow has large velocity gradients at the wall and high values of wall shear stress. Region C (wall jet region) is the area of interest in a jet impingement study as the flow velocity and turbulence decrease as the thickness of the wall jet increases. In this region, the primary flow vectors are parallel to the surface and can be numerically modeled to determine the important corrosion parameters [13].

2.10.2 Mass Transfer of Impinging Jet

Mass and heat transfer have been derived by many authors and have been found to be dependent on many dimensionless quantities including Sherwood number (Sh), Reynolds number (Re), Schmidt number (Sc), the relative jet length (H/d_0) and the relative radial distance from the stagnation point (r/d_0). These correlations also become dependent on the nozzle geometry and flow confinement. The mass transfer coefficient can be found from Equation 2.14.

$$Sh = \frac{k_m d_0}{D_{AW}} \tag{2.14}$$

where k_m is the mass transfer coefficient, d_0 is the nozzle diameter and D_{AW} is the diffusivity of magnetite in water (m^2/s). The Reynolds number for jet impingement studies is described by Equation 2.15.

$$Re = \frac{\rho u d_0}{\mu} \tag{2.15}$$

where u is the jet velocity, ρ is the fluid density and μ is the dynamic viscosity of the fluid (Pa·s). Chin and Tsang studied the mass transfer from an impinging jet to a circular electrode. The experimental results revealed a property of uniform accessibility where the mass transfer is independent of the radial distance up to 0.5 nozzle diameters for laminar jets and 1 nozzle diameter for turbulent jet flow [43]. They proposed Equations 2.16 and 2.17 for jet lengths $0.2 \leq H/d_0 \leq 6$.

$$Sh = 1.51 Re^{1/2} Sc^{1/3} g(Sc)(H/d_0)^{-0.054} \tag{2.16}$$

for laminar flow (Re<2000, and 0.1< r/d_0 <0.5).

$$Sh = 1.12Re^{1/2}Sc^{1/3}g(Sc)(H/d_0)^{-0.057} \tag{2.17}$$

for turbulent flow (4000< Re <16000 and 0.1< r/d_0 <1). g(Sc) is the asymptotic series of Sc given by Equation 2.18.

$$g(Sc) = 1 - \frac{0.084593}{Sc^{1/3}} - \frac{0.016368}{Sc^{2/3}} - \frac{0.0057398}{Sc} + \frac{0.0014288}{Sc^{4/3}} + \frac{0.0013088}{Sc^{5/3}} + ... \tag{2.18}$$

Studies have been completed by Chin and Hsueh on the mass transfer of submerged and unsubmerged jets on flat and cylindrical surfaces. They concluded that there is only a small difference in the local mass transfer between submerged and unsubmerged impinging jets from 0.1< r/d_0 <5 [44]. In another study by Chin and Hsueh on the mass transfer to a flat surface from an unsubmerged impinging jet they proposed Equations 2.19 and 2.20 for the average mass transfer rate of an unsubmerged impinging jet in the region of 0.1< r/d_0 <4 [45]. For r/d_0 <0.8:

$$\bar{Sh} = 0.9Re^{1/2}Sc^{1/3}\left(\frac{H}{d_0}\right)^{-0.09} \tag{2.19}$$

For 0.8< r/d_0 <4:

$$\bar{Sh} = 0.77Re^{1/2}Sc^{1/3}\left(\frac{r}{d_0}\right)^{-1/2} \tag{2.20}$$

where 0.5< H/d_0 <5 and 2500< Re <20000.

A recent study by Hofmann, Kind and Martin [46] investigated the flow structure and the heat/mass transfer from a single round jet impinging perpendicular to a flat plate. Empirical correlations were proposed to predict the local mass transfer rates with the surface-averaged mass transfer rate coefficients that cover a wide range of experimental parameters. The correlations have a simple form for convenience in

practical application while showing no strong deviations from the experimental data from previous literature, even at the stagnation point of the impinging jet. The influence of many parameters was investigated in this study including the nozzle-to-plate distance, Reynolds number, the shape of the nozzle and the radial distance. Equation 2.21 shows the proposed correlation for the local mass transfer rate for a submerged impinging jet.

$$Sh = 0.055(Re^3 + 10Re^2)^{0.25} Sc^{0.42} e^{-0.025(r/d_0)^2} \tag{2.21}$$

Equation 2.21 was integrated over the surface to determine the surface-averaged mass transfer rate correlation in Equation 2.22.

$$Sh = 0.055(Re^3 + 10Re^2)^{0.25} Sc^{0.42} \frac{1 - e^{-0.025(r/d_0)^2}}{0.025(r/d_0)^2} \tag{2.22}$$

Where 14000< Re <230000, 0.5< H/d_0 <10 and 0< r/d_0 <8.

2.11 Computational Fluid Dynamics

Computational fluid dynamics is a branch of fluid mechanics that uses numerical analysis based on the Navier-Stokes equations. The system of equations, which are partial differential equations, fully describes the fluid flow in a pre-set domain. These fundamental equations describe the conservation of mass, momentum and energy for a Newtonian fluid.

$$Mass \rightarrow \frac{\partial \rho}{\partial t} + div(\rho U) = 0 \tag{2.23}$$

$$X_{Momentum} \rightarrow \frac{\partial(\rho u)}{\partial t} + div(\rho u U) = \frac{\partial p}{\partial x} + div(\mu grad(u)) + S_{mx} \tag{2.24}$$

$$Y_{Momentum} \rightarrow \frac{\partial(\rho v)}{\partial t} + div(\rho v U) = \frac{\partial p}{\partial y} + div(\mu grad(u)) + S_{my} \quad (2.25)$$

$$Z_{Momentum} \rightarrow \frac{\partial(\rho w)}{\partial t} + div(\rho w U) = \frac{\partial p}{\partial z} + div(\mu grad(u)) + S_{mz} \quad (2.26)$$

$$Internal\ Energy \rightarrow \frac{\partial(\rho i)}{\partial t} + div(\rho i U) = -Pdiv(U) + div(kgrad(T)) + \Phi + Q_i \quad (2.27)$$

$$Equation\ of\ State \rightarrow P = P(\rho, T) \quad (2.28)$$

$$Equation\ of\ State \rightarrow i = i(\rho, T) \quad (2.29)$$

where ρ (kg/m^3) is the fluid density, k (W/m·K) is the thermal conductivity, U (m/s) is the fluid velocity, S (N/kg) accounts for the body forces, P (Pa) is the pressure, T (K) is the temperature, i (J/kg) is the internal energy, Φ (J/m^{3}s) is the viscous dissipation term, Q (J/m^3) is the volumetric heat generation while u,v and w (kg·m/s) are the momentum terms in their respective directions.

The system of equations has seven unknowns (pressure, u/v/w- momentum, internal energy, temperature and density) and with the use of two auxiliary thermodynamic relationships (equations of state) and the five conservation equations, the system of equations may be solved. By creating a discrete grid (mesh) for a finite amount of control volumes in the fluid domain, these equations may be solved with commercial CFD software such as ANSYS Fluent or CFX to fully describe the fluid flow within the domain.

2.12 Film-Forming Amines

Film-forming products can be divided into two separate groups; Film-Forming Amine Products (FFAPs) that contain one or more FFAs as their surface active substance, or Film-Forming Products (FFPs) that contain non-amines as their active ingredient

[47]. Film-forming amines (FFAs) contain one or several primary and/or secondary amine groups and aliphatic carbon chains (10 to 22 atoms long) that can be saturated or unsaturated. The amine group in the FFA molecule bonds to the metal or oxide surface, pointing the aliphatic part of the molecule towards the coolant as seen in Figure 2.17. This makes the metal/oxide surface hydrophobic and will further protect the metals surface. Three commonly used FFAs are Octadecylamine (ODA), Oleylamine (OLA) and Oleyl Propylenediamine (OLDA). Ammonia is typically added as an alkalizing component as the FFA is not a strong base, and does not necessarily increase the coolant pH. Other examples of alkalizing amines include 2-aminoethanol, cyclohexylamine, morpholine and 3-methylpropylamine.

FFAs have been claimed to reduce corrosion during operation and shutdown/layup, minimize corrosion product transport and create the formation of clean, smooth heat transfer surfaces. Some of the commercial FFA products available have been tested in power plants and are claimed to have an impact on several corrosion mechanisms but this has not been scientifically established, besides a few studies [47]. Some of the various FFA brands include Cetamine, Helamine and ODACON but unfortunately the ingredients of these commercial mixtures are non-disclosed.

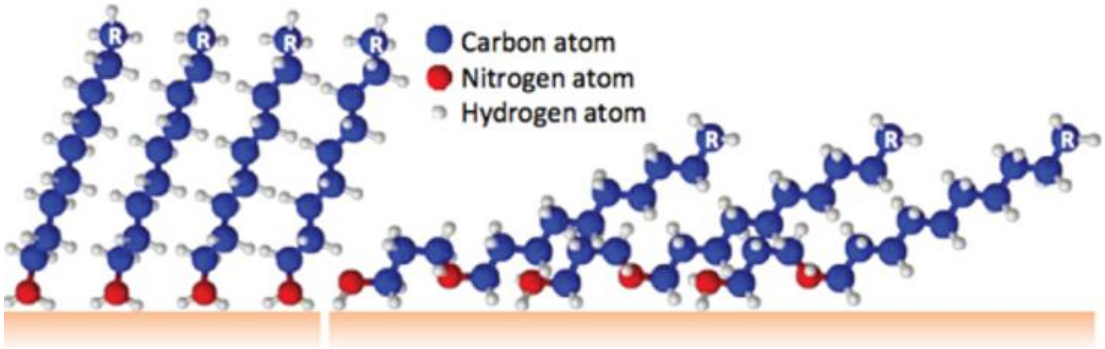

Figure 2.17: Schematic reprsentation of FFA films: monoamine (left), polyamine (right)

The adsorption takes place on metal surfaces including steel, copper, stainless steel and any of the protective oxides that form on these metal surfaces. Studies suggest that an initial thin layer forms on the surface rapidly followed by a second slower adsorption of the FFA. The durability of the film under plant water/steam conditions is not completely understood but experience shows that a system with an established film is protected for roughly two weeks of a wet storage shutdown period. Trial FFA applications have occurred in Almaraz Unit 1 and Unit 2 (PWR, Spain) since 2011 to further reduce the feedwater iron transport into the steam generators. Under PWR power plant conditions, the injection of ODA created a non-wettable film (Figure 2.18) that lowers the corrosion rate while reducing the number of harmful chemicals like hydrazine. Iron concentrations were found to be reduced below 2 ppb during normal power operation as shown in Figure 2.19 [48].

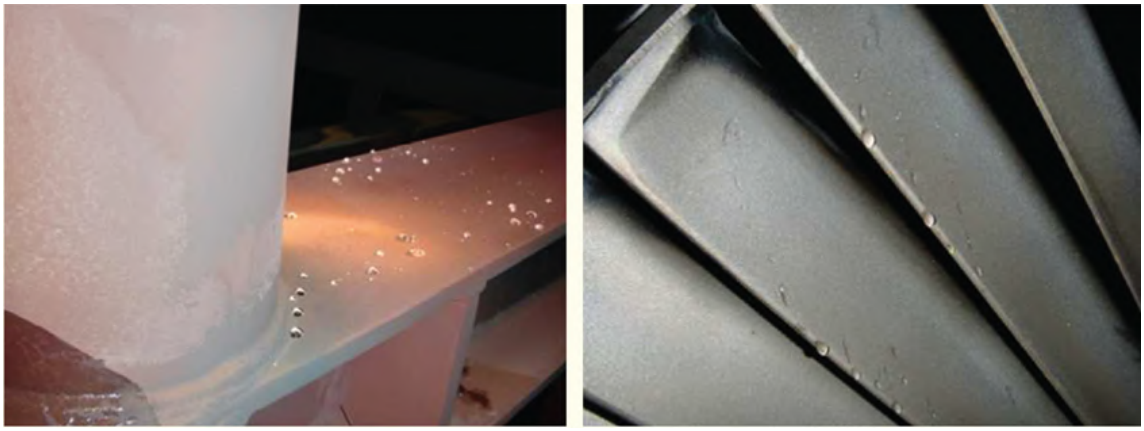

Figure 2.18: Hydrophobic surface on condenser (left) and turbine (right)

Figure 2.19: Iron reduction into steam generators in Almaraz Unit 1 [49]

Chapter 3

Experimental Procedure

3.1 Magnetite Synthesis

The first step in the experimental procedure to measure the dissolution rate of magnetite is to synthesize high-quality magnetite, similar to the magnetite formed due to corrosion of carbon steel. There are several different methods for synthesizing highly pure magnetite but the solid-phase reaction of heating a stoichiometric mixture of iron and hematite was chosen. The reaction of Equation 3.1 was proven to give pure magnetite with a monodisperse particle size by de Pierrefeu [5].

$$4Fe_2O_3 + Fe \longrightarrow 3Fe_3O_4 \tag{3.1}$$

Hematite (ferric oxide anhydrous from Fisher Chemicals, 99.5%) and iron (325 mesh iron from Alfa Inorganics Ventron, 98%) were mixed in stoichiometric amounts in a ceramic mortar with a small amount of ethanol to ensure they have been mixed thoroughly. The mixture was vacuum sealed in a piece of quartz glassware and heated in a furnace (Carbolite RHF 1500 Furnace). The temperature and heating/cooling rates are crucial for the suitable pelletization of the magnetite powder. From de

Pierrefeu, the optimal parameters to synthesize magnetite was at a heating/cooling rate of 0.5°C/min to a temperature of 600°C for 12 hours. This method was proved to provide small particle size (micron range), narrow size distribution and a spherical particle shape. The purity of the magnetite powder was tested with Raman spectroscopy (Renishaw inVia Raman Microscope) with the particle size observed with a Scanning Electron Microscope (SEM). Twenty grams of highly pure magnetite was synthesized in each batch to provide large enough amounts of powder for the pelletization of multiple magnetite pellets.

3.2 Magnetite Pelletization

To measure the dissolution rate of magnetite, similar to the oxide formed during carbon steel corrosion, the powder must be formed into high quality magnetite pellets. The pellets must by highly pure with no chemical additives, highly dense structure with little porosity and a strong erosion resistant surface. The process of magnetite pelletization was adapted and refined from that of de Pierrefeu [5]. The synthesized magnetite powder was placed in a cylindrical mold constructed of 1144 carbon steel seen in Figure 3.1.

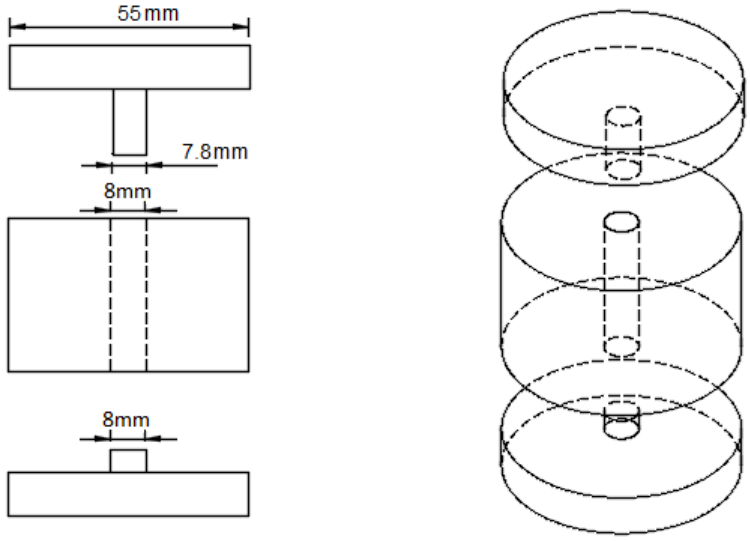

Figure 3.1: Cylindrical mold for making magnetite pellets

A pressure of 500 MPa was applied with the use of a Carver laboratory hydraulic press for 10 minutes to make a compact pellet. The sintering of magnetite pellets has been studied by de Pierrefeu but a higher sintering temperature was recommended to get full densification and to minimize porosity. From Mohajery [6], 1100°C was shown to not properly sinter smaller grain magnetite powder leaving a granular pellet interior that leads to drastically high dissolution rates compared to a well-sintered pellet. The difference between a poorly sintered and well-sintered magnetite pellet is shown in Figure 3.2.

Magnetite pellets were sintered at 1300°C for 5 hours under an argon atmosphere to avoid oxidation of magnetite to hematite at high temperatures. Figure 3.3 shows the experimental set up for pellet sintering.

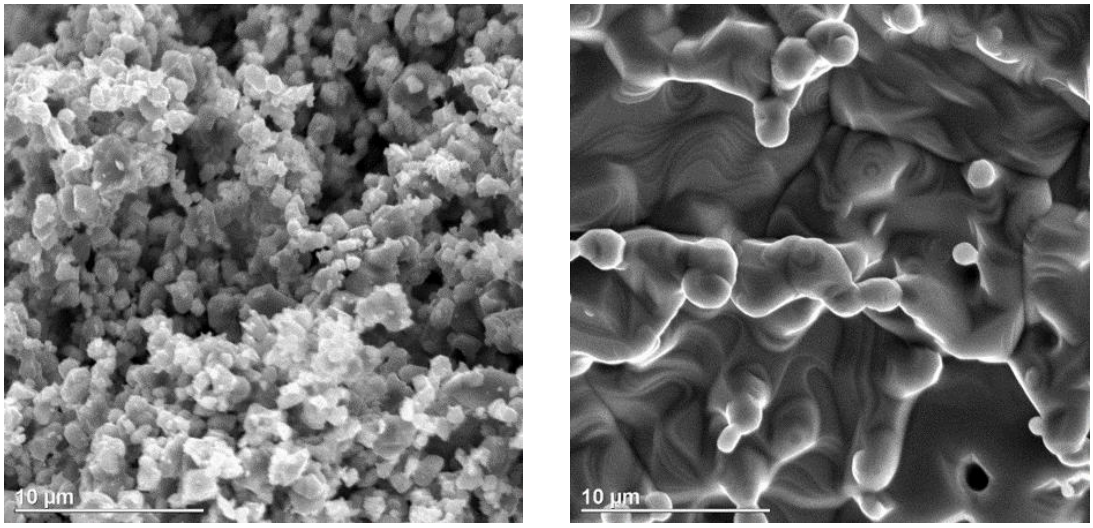

(a) Poorly sintered magnetite pellet (b) Well sinterered magnetite pellet

Figure 3.2: Difference between poorly and well sintered magnetite pellets

Pellets were analyzed with Raman to confirm the pellet remained pure magnetite during the sintering process, and with SEM to determine if the pellet interior was sintered properly. To get ready for dissolution experiments, the pellet's top surface must be polished to remove loose particles and to decrease roughness in order to reduce eddies and turbulence that could cause an increased erosion effect. The top surface is then analyzed with a Taylor-Hobson Surtronic 25 mechanical profilometer for comparison of the surface after the dissolution experiment. Finally, the pellet was wrapped with Swagelok PTFE tape that allows for a tight fit in the test section and leaves only the top surface to be exposed to the jet flow.

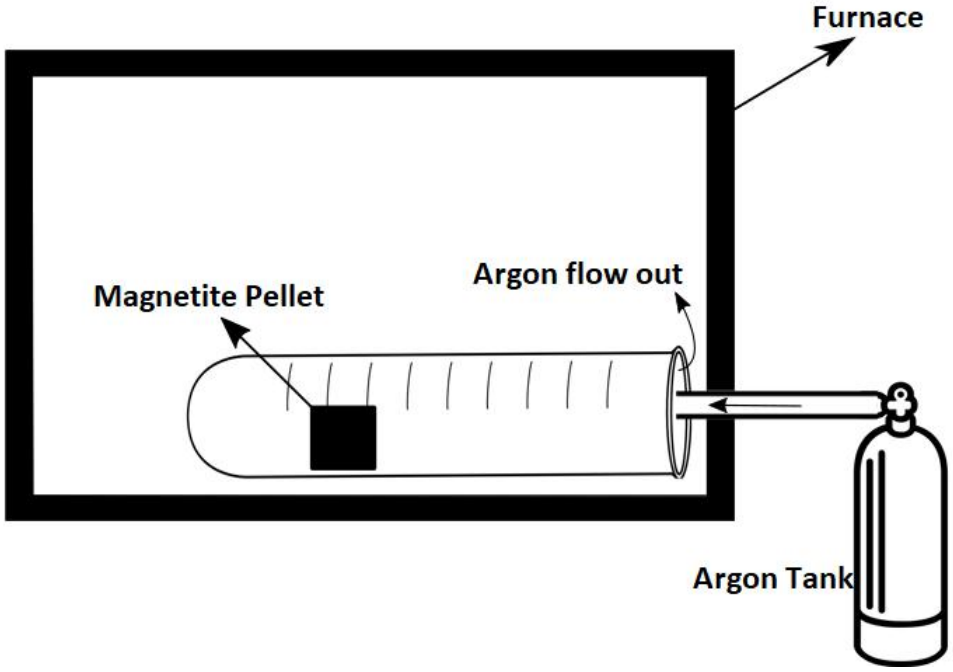

Figure 3.3: Furnace set up for sintering

3.3 Experimental Loop

Dissolution experiments were conducted in two different recirculating water loops due to a pump failure following Run 1.2 in the original loop II and therefore loop III was used for Runs 1.3, 2.1, 3 and 4. Loop II was repaired for the remaining experimental runs (Run 2.2 and 5). Table 3.1 shows the conditions during each experimental run.

Table 3.1: Experimental run conditions

Run No.	[Time] (h)	Flow Rate (mL/s)	Temperature (°C)	$pH_{25°C}$	Purge Gas	$[O_2]$ (ppb)
1.1	672	2.33	140	9.2	Ar	0
1.2	240	1.89	140	9.2	Ar	20
1.3	336	4.0	140	9.2	Ar	0
2.1[1]	336	4.0	140	9.2	Ar	0
2.2 [1]	336	3.0	140	9.2	Ar	0
3[2]	336	4.0	140	Neutral	Ar	0
4[3]	336	4.0	140	Neutral	Ar	0
5[2]	336	3.0	140	9.2	Ar	0

[1] $[N_2H_4]$ = 200 ppb

[2] FFA Injection

[3] FFA Equilibrium

Loop II is mostly constructed out of 316L stainless steel, with the reservoir being constructed from 304L stainless steel, with the loop diagram seen in Figure 3.4. The loop begins with the 60-litre reservoir that is filled with deionized water that is chemically adjusted via an injection septum and purged with argon to remove any dissolved oxygen. A rubber gasket is installed between the tank and the cover to ensure no oxygen leaks into the loop water. Coolant flows from the tank to the Milton Roy XT11 positive displacement pump, with a maximum flow rate of 8.3 L/h and a pressure limit of 2000 psi, and then to the interchanger. The interchanger consists of a tube-in-tube, counter-current heat exchanger where fluid from the test section transfers heat to the cold coolant coming from the pump. The hot fluid is contained in the inner tubes while the cold fluid flows in the annular space and then flows to

be heated by the preheater. The preheater is used to heat the inward coolant and consists of a high-pressure and high-temperature pressure vessel that uses three 1 kW cartridge heaters. The preheater uses a Eurotherm 3216 process controller with the use of type K thermocouples to measure the temperature upstream and downstream of the pre-heater. The coolant flows from the pre-heater through the rope heater that accounts for lost heat and then passes through the jet impingement test section. The impinging jet test section consists of a 19 mm stainless steel Swagelok tee with a nozzle made of Inconel 600 with a 0.5 mm diameter orifice. The jet impinges on the surface of the magnetite pellet inside the tee section and exits from the horizontal section of the Swagelok fitting. The pellet is fitted inside a Teflon holder with a distance of 1 mm between the jet orifice and the pellet surface. The cross-sectional jet diagram can be seen in Figure 3.5. The flow then passes through the interchanger once again and to the cooler, which is a shell-tube heat exchanger with the building cooling water at the shell side. The cooler returns the coolant to room temperature where it passes through a Swagelok 4TF Tee-Type filter and a Swagelok R3A high-pressure proportional relief valve, which is used to control the loop pressure. Flow finally passes through the ion exchange section that is packed with Purolite NRW-37 mixed bed resin and then through one more filter section on the way back to the reservoir.

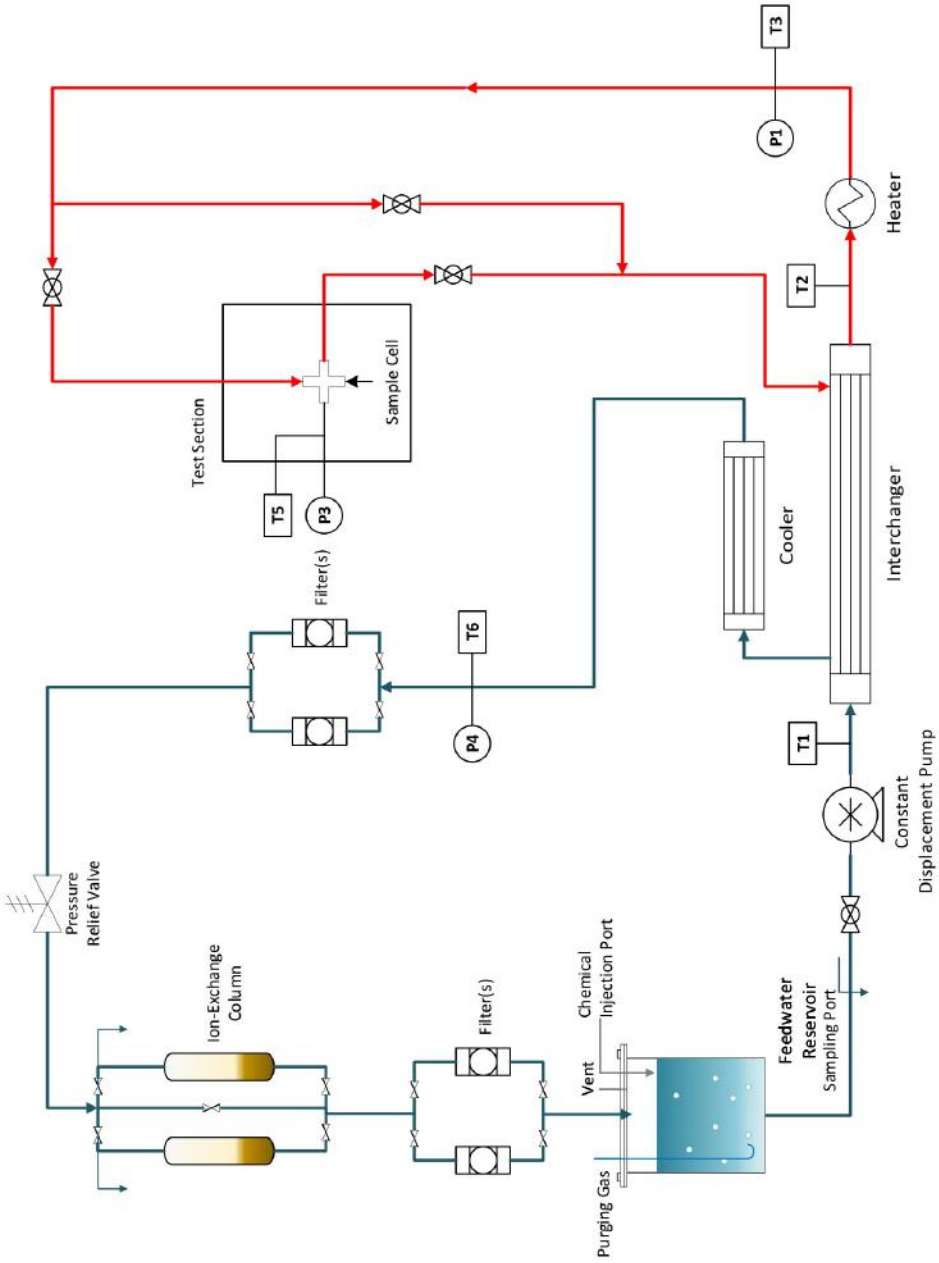

Figure 3.4: Loop II diagram

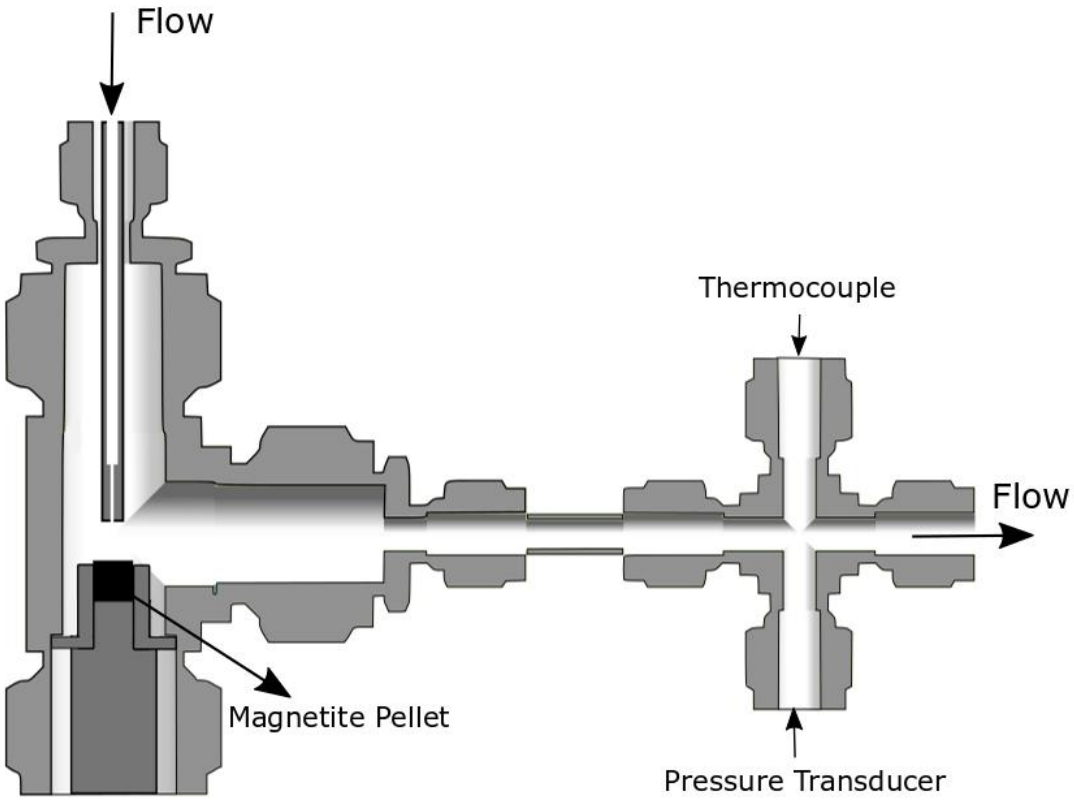

Figure 3.5: Jet impingement test section

Loop III is constructed from 316L stainless steel and operates with a maximum temperature of 320°C, maximum pressure of 12.5 MPa and a maximum flow rate of 0.6 L/min. The loop III diagram seen in Figure 3.6 has a very similar setup to loop II but was constructed for high flow rate experiments with much more complexity. A detailed analysis of the loop operation can be referenced from Lertsurasakda [50]. The loop utilizes a preheater with a 6 kW jacket heater and four 1 kW cartridge heaters and a main heater with a 9 kW jacket heater and six 1 kW cartridge heaters. A Hach Orbisphere is installed in a bypass line off the return line to the tank to measure the oxygen concentration and is capable of measuring a residual signal with high accuracy (±0.1 ppb). Pressure in the test section and in the loop is controlled

with a Tescom pneumatic control back-pressure regulator with the controlling sensor located just downstream of the test section. The final components that are used in loop III and not in loop II include the rotameter to measure the flow rate in the low-pressure region and the pulsation dampener that is located downstream of the Milton Roy positive displacement pump to eliminate flow oscillation.

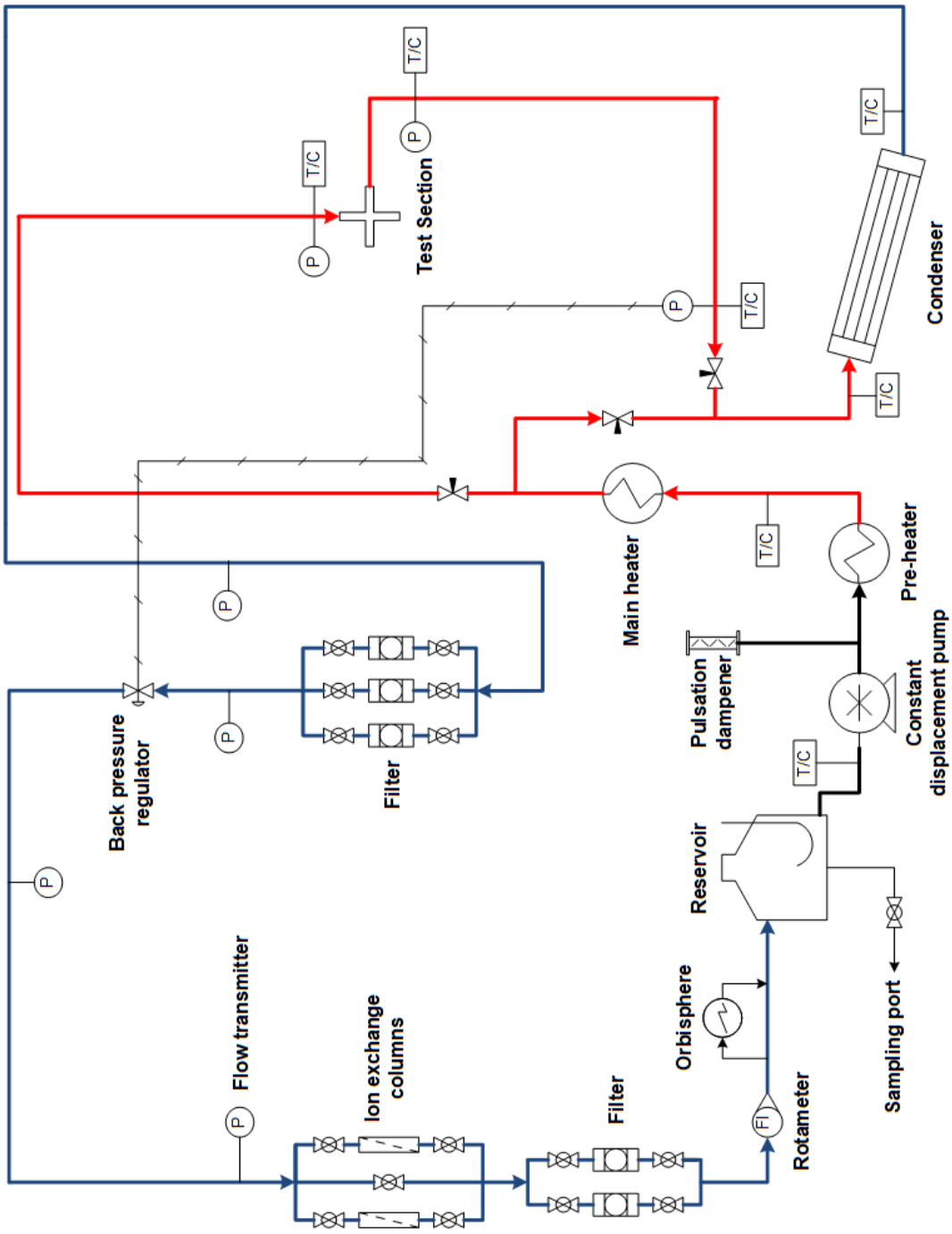

Figure 3.6: Loop III diagram

3.4 Profilometry Technique

To measure the dissolution of the magnetite pellets that have been exposed to the flow from the jet impingement, a profilometry technique is used. A Taylor-Hobson Surtronic 25 mechanical profilometer (2μm stylus tip) with MBT616/M positioning stage is used to measure the volume of magnetite removed, with the set-up seen in Figure 3.6. To accurately measure the surface profile these steps must be followed:

- Secure the pellet on the positioning stage.
- Adjust the traveling distance of the profilometers stylus to a value appropriate for the area of dissolution.
- Use the positioning stage to position the stylus over the starting point on the pellet surface and to regulate the pellet so the tip of the stylus touches the surface.
- Record the first measurement with the use of Taly-profile software of the surface profile. The overall slope of the surface is removed by the software.
- Remove the stylus from the surface and adjust the position by moving the stylus 50 μm and record another measurement.
- These measured surface profiles are then integrated to give the volume of dissolved magnetite. The dissolution rate can be calculated knowing the density, exposure time and the calculated volume.

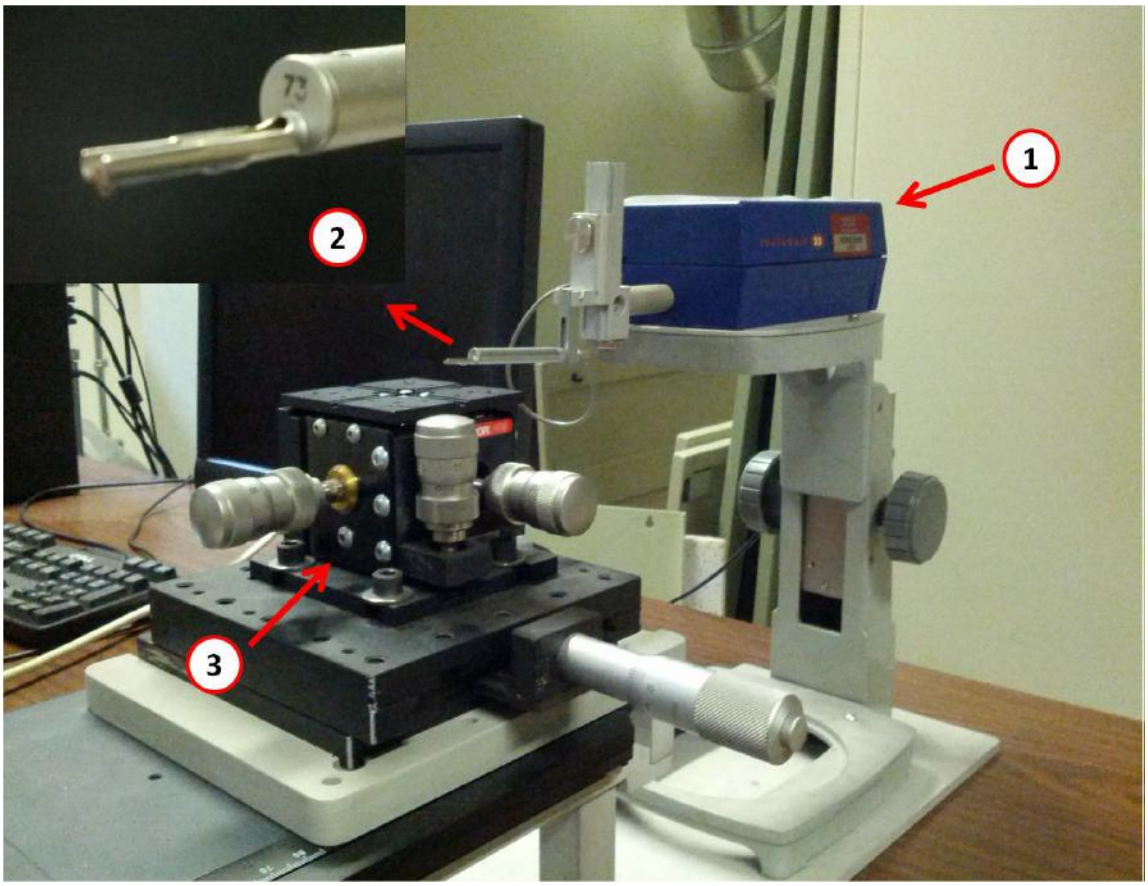

Figure 3.7: 1- Surtronic 25 profilometer, 2- stylus, 3- positioning stage [6]

Chapter 4

Results and Discussion

4.1 Run 1: $pH_{25°C}$ 9.2 (NH_3), 140°C

4.1.1 Run 1.1: flow rate 2.33 mL/s, exposure time 672 hours, sinter at 1100°C for five hours

The first jet impingement study was completed at a $pH_{25°C}$ of 9.2 at 140°C, controlled with ammonia, while purging Argon to remove dissolved oxygen. Magnetite has a maximum solubility at 140°C and correlates to the highest rates of FAC. This condition caused the feedwater line rupture at the Mihama-3 PWR in 2004. This run continues on the work completed by Mohajery [6] and is used for comparison of magnetite dissolution rates at similar chemistry conditions. The magnetite pellet used for Run 1.1 is shown before exposure in Figure 4.1. These conditions were studied by Mohajery, and dissolution was small and difficult to measure, therefore the exposure time was increased to 672 hours to show measurable dissolution.

After the exposure, a crater of 1.1 mm in diameter (2.2 times the jet diameter) was formed due to the removal of magnetite. The SEM pictures of the magnetite pellet

after exposure are seen in Figure 4.2.

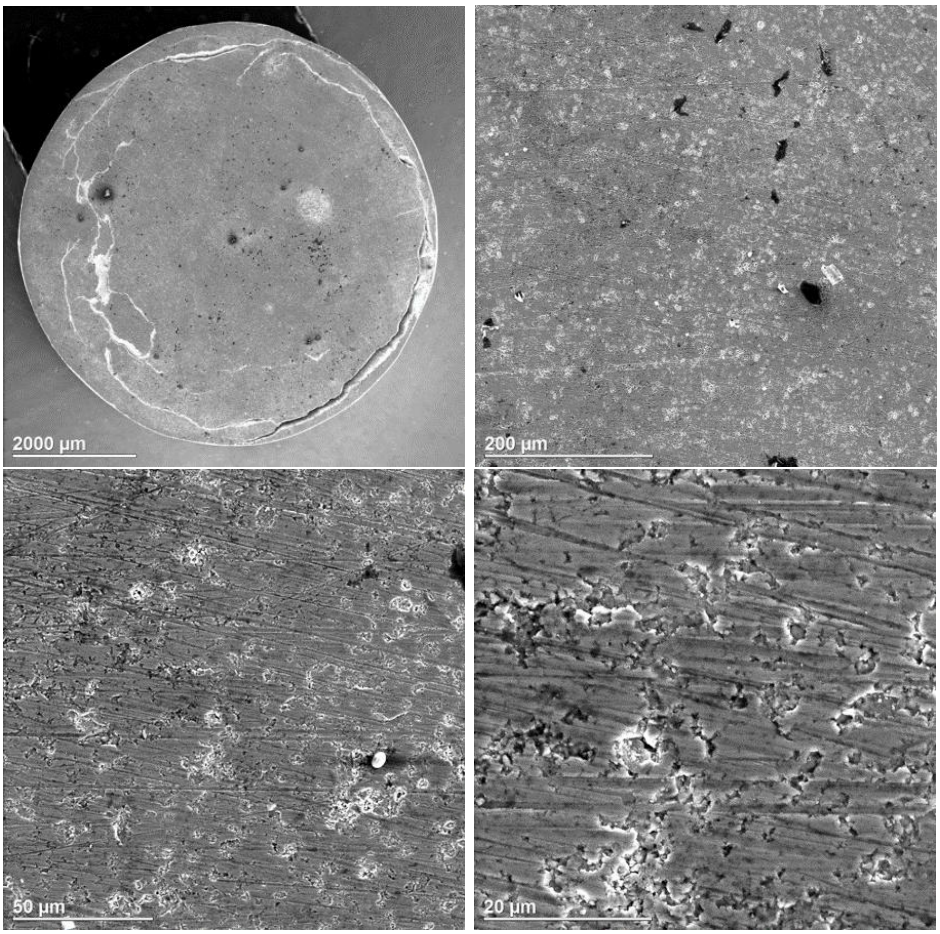

Figure 4.1: Magnetite pellet before exposure in Run 1.1

The crater was unexpected due to the low solubility of magnetite at this coolant chemistry condition and due to the lack of dissolution observed in the experiments completed by Mohajery. This presented a problem with poor sintering that has been dealt with in previous studies. This magnetite pellet was sintered at 1100°C for five hours and the pellet after polishing seems to show proper sintering in Figure 4.1. After jet impingement exposure, and the removal of the polished surface, the interior of the pellet shows poor sintering with only initial steps of sintering neck growth between magnetite particles. The pellet was broken to observe the pellet

interior that can be seen in Figure 4.3. The interior of the pellet shows a granular structure, that will lead to a higher removal rate of magnetite due to the removal of entire particles from erosion. The erosion of the poorly sintered pellets is discussed further in Section 4.9.

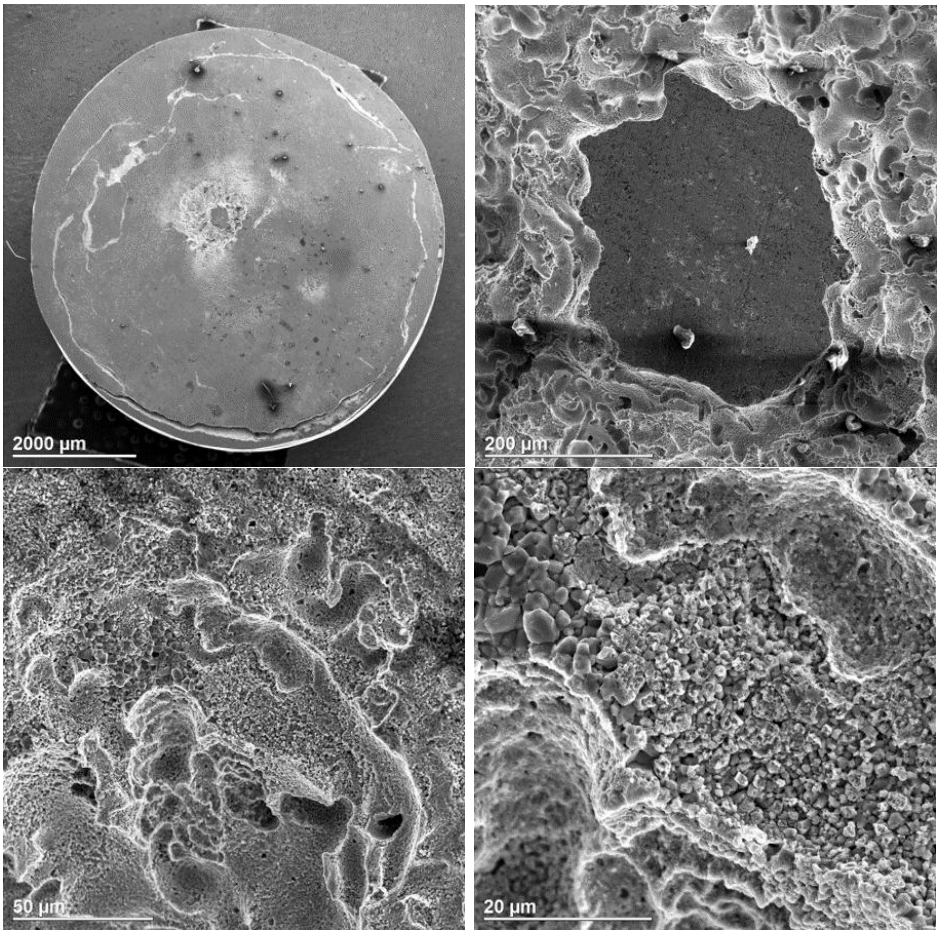

Figure 4.2: Magnetite pellet after exposure in Run 1.1

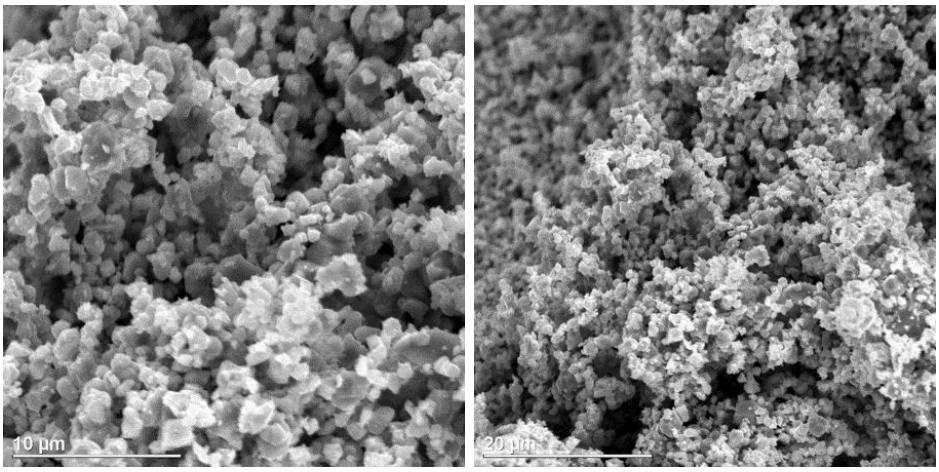

Figure 4.3: Interior of magnetite pellet used for Run 1.1

4.1.2 Run 1.2: flow rate 1.89 mL/s, exposure time 240 hours, sinter at 1200°C for six hours

Run 1.2 followed the same coolant chemistry conditions as the previous run with a magnetite pellet that was sintered at 1200°C for 6 hours to properly sinter the pellet to withstand the high erosion from the jet impingement. An unexpected crater was present after 240 hours of jet impingement exposure with a diameter of 1 mm (2 times the jet diameter). The flow rate of the loop decreased over the duration of the run due to a faulty pressure relief valve that also caused an increase in the concentration of dissolved oxygen from 0 to above 20 ppb. The surface was covered in a layer of hematite due to the oxidation of magnetite at high levels of oxygen.

The SEM pictures of the magnetite pellet after exposure can be seen in Figure 4.4. Due to the crater and the large rate of magnetite removal, the pellet was broken to observe the quality of the sintering that can be seen in Figure 4.5. The pellet interior shows more complete sintering then the pellet used in Run 1.1 with the development of small grains of roughly 10 μm.

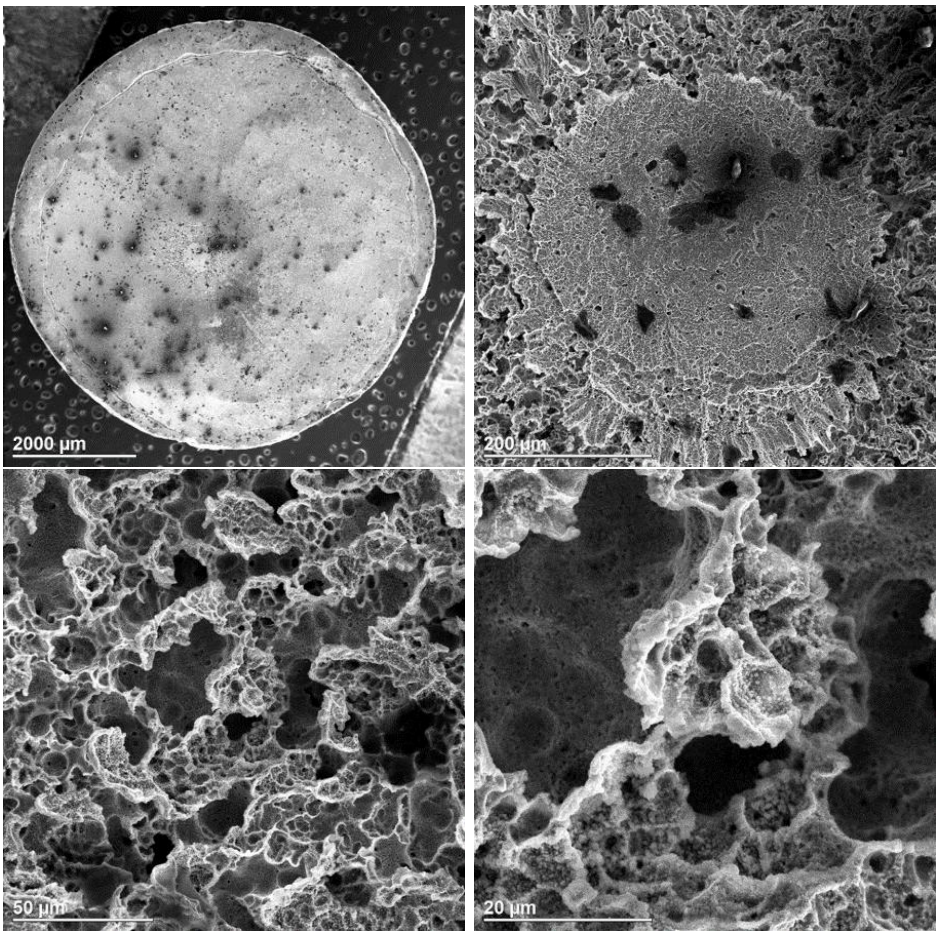

Figure 4.4: Magnetite pellet after exposure in Run 1.2

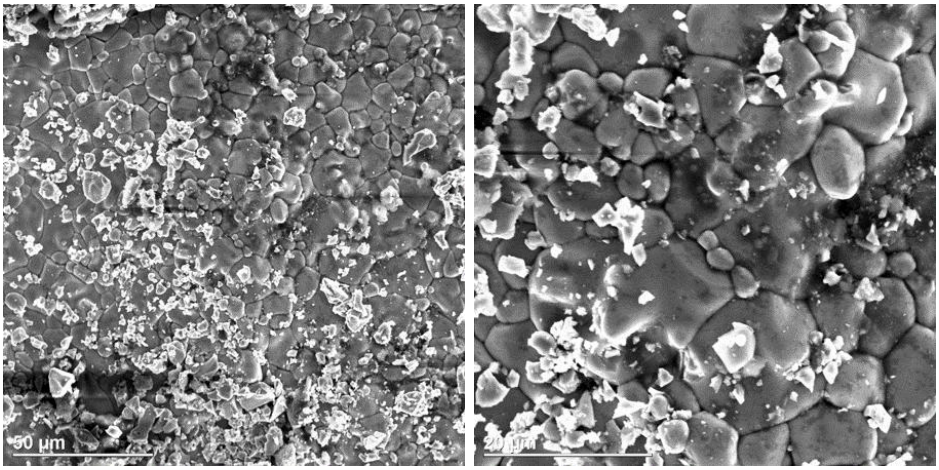

Figure 4.5: Interior of magnetite pellet used for Run 1.2

To complete the sintering, that can withstand the high rates of erosion and shear stress from the jet impingement flow, a higher temperature must be utilized to manufacture properly sintered magnetite pellets.

4.1.3 Run 1.3: flow rate 4.0 mL/s, exposure time 336 hours, sinter at 1300°C for five hours

Following Run 1.2 the oxygen concentration of the loop was increased to high concentrations, which was previously thought to come from a faulty pressure relief valve. After replacement of the pressure relief valve, the oxygen concentration did not decrease leading to finding a ruptured O-ring and faulty threads on the pump's discharge connection.

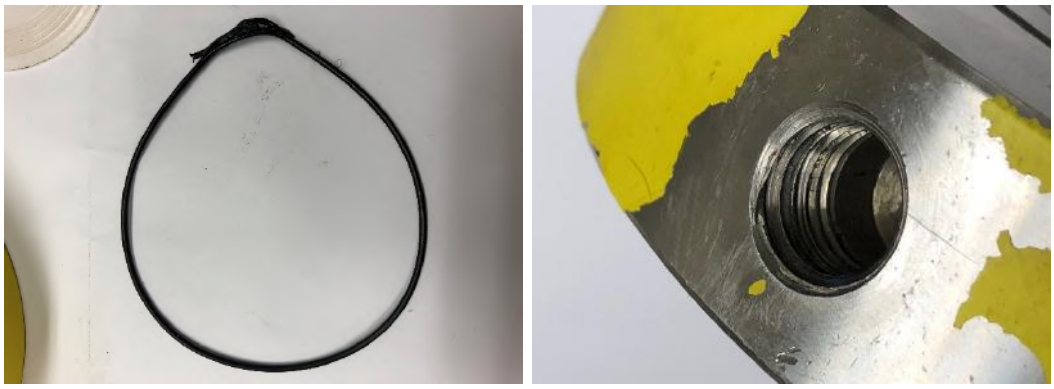

Figure 4.6: Faulty O-ring and thread from loop II pump

To continue the experiment while the pump was undergoing maintenance the test section was moved to experimental loop III that is described in Section 3.3. Run 1.3 followed the same chemistry conditions used in the previous runs but the new experimental loop allowed the flow rate to be increased to 4 mL/s, that is closer to the previous UNB magnetite dissolution studies [5, 6]. The pellet used for Run 1.3 was sintered at 1300°C for 5 hours with a small piece broken on the bottom of the

pellet to inspect the sintering of the pellet before the dissolution experiment. The pellet interior can be seen in Figure 4.7 and shows good sintering with large 50 μm grains.

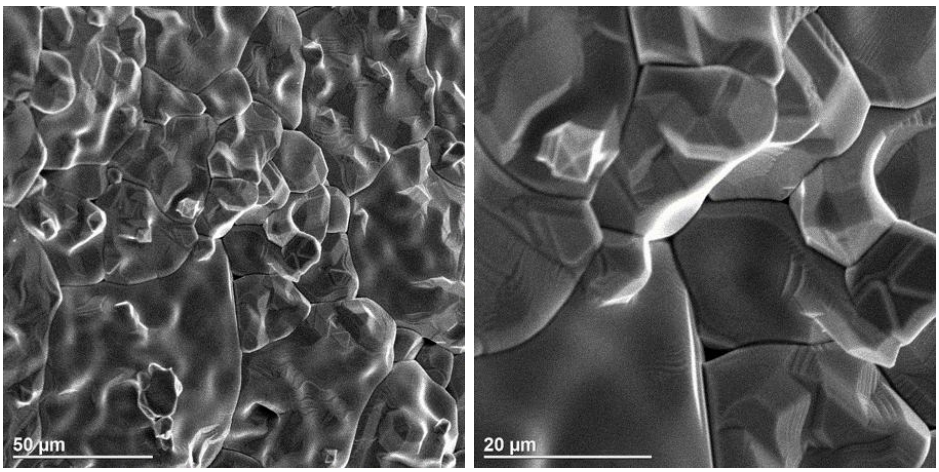

Figure 4.7: Interior of magnetite pellet used for Run 1.3

The magnetite pellet was exposed under jet impingement conditions for 336 hours and the post-exposure SEM pictures can be seen in Figure 4.8. The pellet shows significantly less oxide removal then the previous two runs and suggests that the pellets sintering was acceptable to withstand the aggressive erosion conditions due to the jet impingement. Raman analysis shows that the center of the small dissolution area was a mixture of hematite and magnetite while outside the area remained pure magnetite. Figure 4.9 shows the Raman analysis.

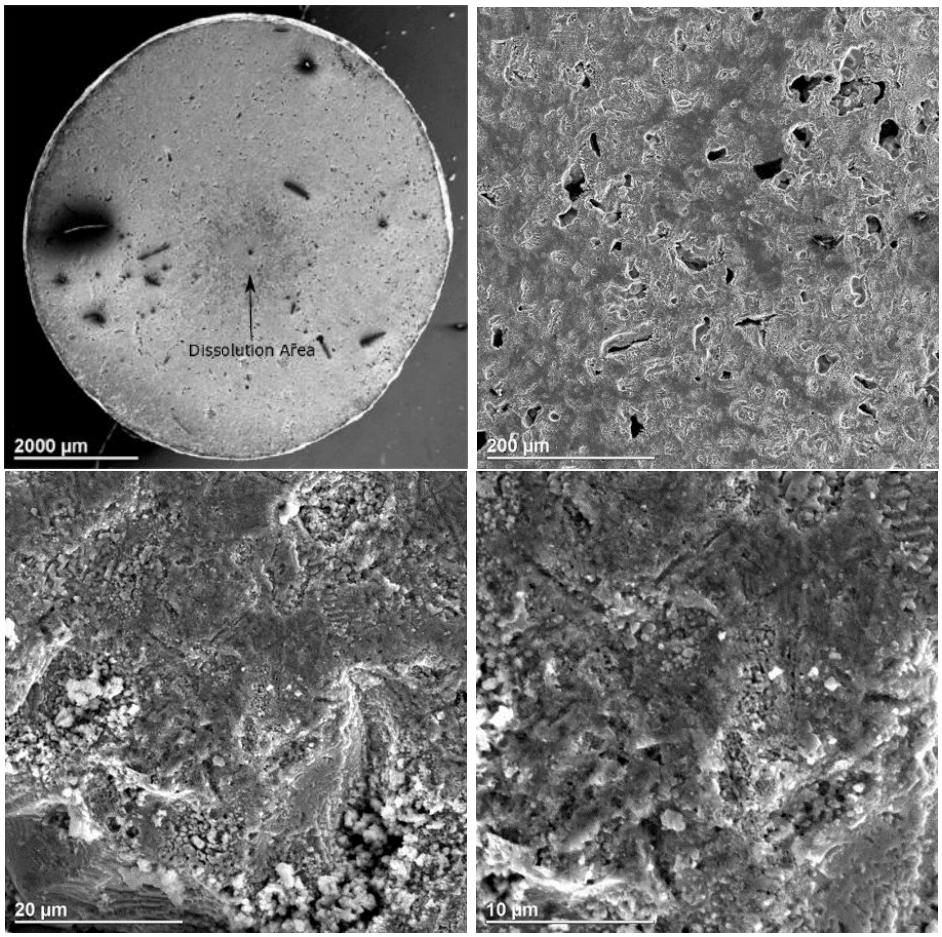

Figure 4.8: Magnetite pellet after exposure in Run 1.3

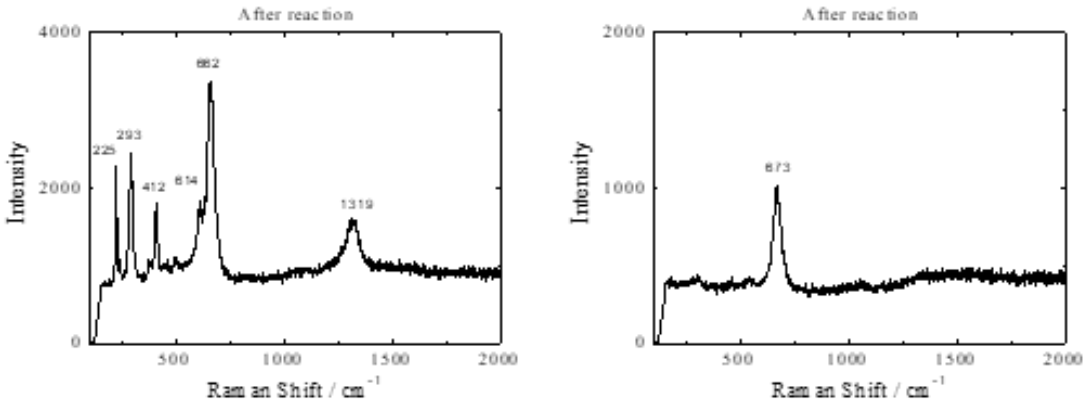

(a) Hematite/Magnetite in dissolution area (b) Magnetite outside dissolution area

Figure 4.9: Raman analysis of Run 1.3

4.2 Run 2: $pH_{25°C}$ 9.2 (NH_3), 140°C,[N_2H_4] 200 ppb

4.2.1 Run 2.1: flow rate 4.0 mL/s, exposure time 336 hours, sinter at 1300°C for five hours

Run 2.1 was completed in ammoniated water with a $pH_{25°C}$ of 9.2 at 140°C with an excess of hydrazine at a concentration of 200 ppb. Hydrazine is typically used to remove oxygen from feedwater systems. Argon was used as the purging gas to help with the removal of dissolved oxygen alongside the use of hydrazine. The magnetite pellet used for Run 2.1 is shown before exposure in Figure 4.10. The magnetite pellet used was sintered at 1300°C for 5 hours, which was sufficient for Run 1.3.

After the exposure of 336 hours, a large circular area of hematite was present with a smaller area dissolution area on the outer edge of the developed hematite oxide. The oxygen concentration for the run was zero for the duration of the experiment but with

similar conditions Mohajery [6] and McLaughlin [42] experienced the development of hematite with zero oxygen. The formation of hematite could result from an increased oxygen concentration during the inital stages of the experiment when the test section is placed in the experimental loop.

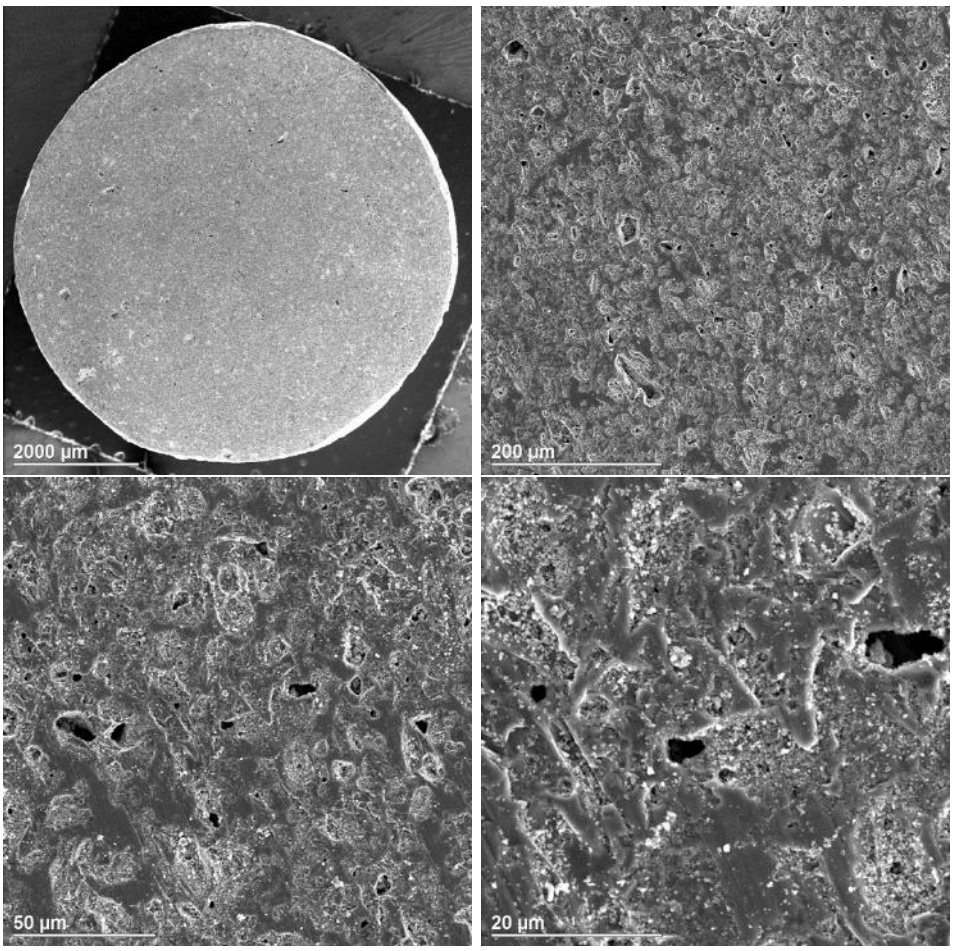

Figure 4.10: Magnetite pellet before exposure in Run 2.1

The post-exposure SEM pictures can be seen in Figure 4.11. The pellet sintering was of similar quality to Run 1.3 but the results are drastically different with much larger dissolution than Run 1.3 and Run 2 by Mohajery at the same experimental conditions. Run 2.2 must be completed to see if these results can be duplicated or if an unknown factor caused an increase in the dissolution rate at these conditions.

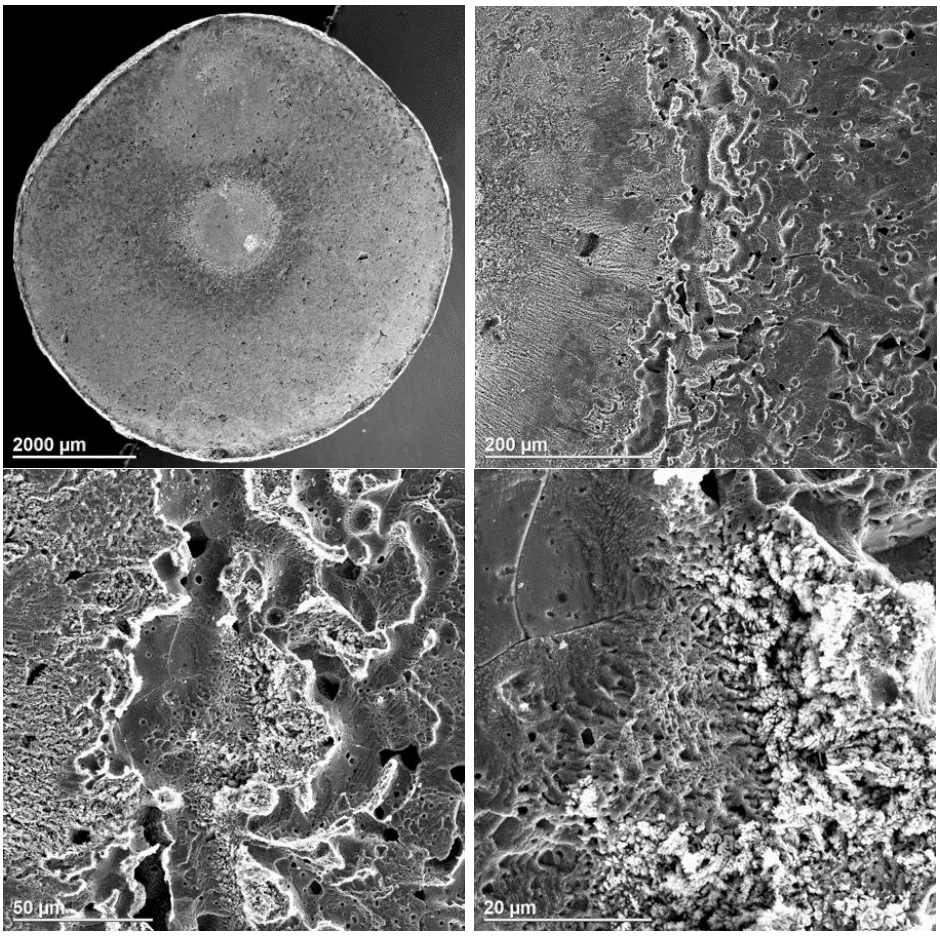

Figure 4.11: Magnetite pellet after exposure in Run 2.1

4.2.2 Run 2.2: flow rate 3.0 mL/s, exposure time 336 hours, sinter at 1300°C for five hours

Run 2.2 was completed at the same conditions as Run 2.1 with a $pH_{25°C}$ of 9.2 at 140°C with an excess of hydrazine at a concentration of 200 ppb. This run was completed to determine if an unknown factor caused the unexpected results of the previous Run 2.1. The same pellet as Run 1.3 was used for this test, which proved to be well-sintered and withstood the erosion from the jet impingement test section. Argon was used to remove any dissolved oxygen alongside the excess of hydrazine

which kept the oxygen concentration at zero ppb for the duration of the experiment. This run was completed on the repaired Loop II with an increased flow rate of 3 mL/s.

After the exposure of 336 hours, a very small dissolution area was found on the magnetite pellet shown with the post exposure SEM pictures in Figure 4.12. The dissolution area is difficult to notice with the SEM photos and shows even less dissolution then Run 1.3, with only a slight decrease in the depth of polishing lines.

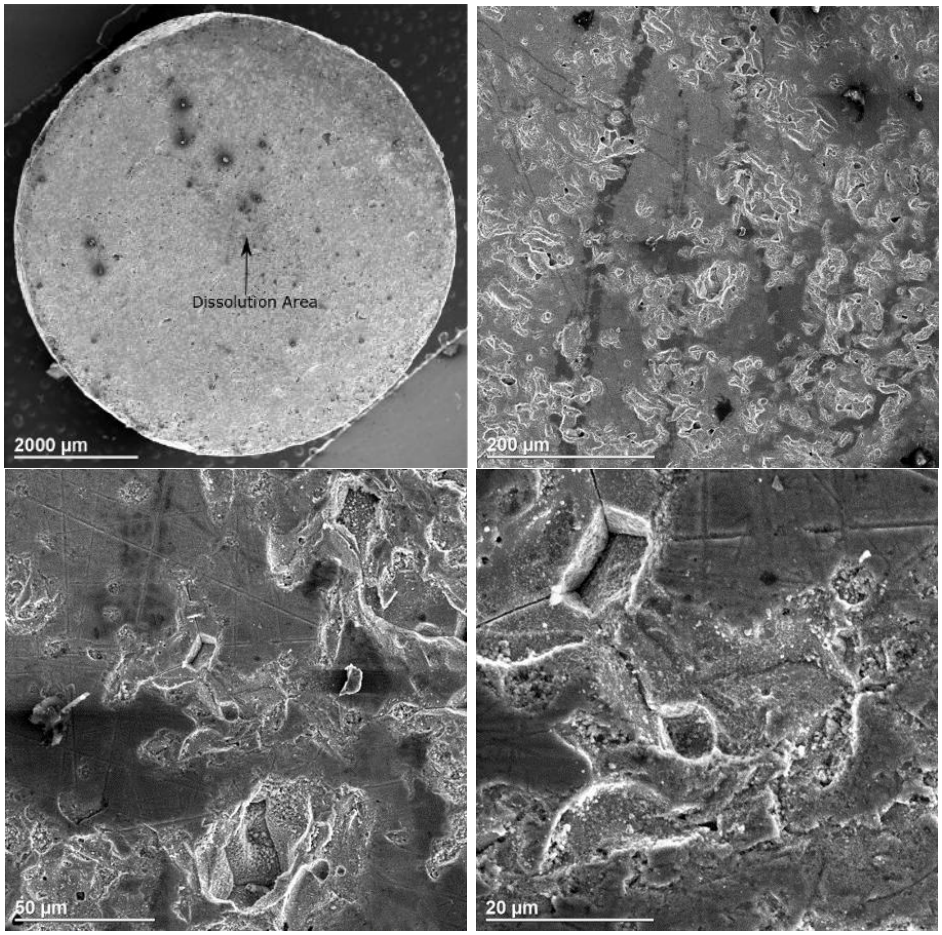

Figure 4.12: Magnetite pellet after exposure in Run 2.2

A mixture of hematite and magnetite was again found in the dissolution area with magnetite still present at the outer edge of the pellet. Oxygen was controlled at

0 ppb for the duration of the experiment with the use of argon and the excess of hydrazine but could be increased for a short period of time when the test section is placed in the experimental loop.

4.3 Run 3: $pH_{25°C}$ Neutral, 140°C, Cetamine® V219 injection, flow rate 4.0 mL/s, exposure time 336 hours, sinter at 1300°C for ten hours

Runs 3 and 4 were completed to investigate the effects of film-forming amines on the dissolution rate constant of magnetite. Run 3 was completed at a neutral pH at 140°C due to the solubliity of magnetite being roughly 10 times higher under these conditions than the previous experiments. Argon was used as the purging gas for oxygen control and the oxygen remained at zero for the duration of the experiment. Cetamine® V219, provided by Kurita Water Industries Ltd., contains oleylpropylene diamine (OLDA) as a film-forming component and cyclohexylamine (CHA) as an alkalizing component. If left undisturbed, the product will separate into two liquid layers; the FFA is the yellowish top layer and the alkalizing agent is the clear bottom layer. The product must therefore be mixed thoroughly to create a homogeneous mixture before each use. FFA research is being completed at UNB on its effectiveness to reduce flow-accelerated corrosion but this is the first study investigating the effect of FFA on the dissolution rate constant of magnetite with a jet impingement study.

Run 3 was completed during the initial injection phase of Cetamine® V219 to the experimental loop coolant seen in Figure 4.13. The CHA component caused the coolant's pH to be slightly increased from neutral conditions, which will cause a

slight decrease in the magnetite solubility. Since the CHA concentration is unknown in Cetamine® V219 it is difficult to predict the amount that the pH will increase. The magnetite pellet used for Run 3 was sintered at 1300°C for 10 hours to reduce the porosity seen in the pellets used for Run 1.3 and 2 and the pre-exposure SEM pictures can be seen in Figure 4.14.

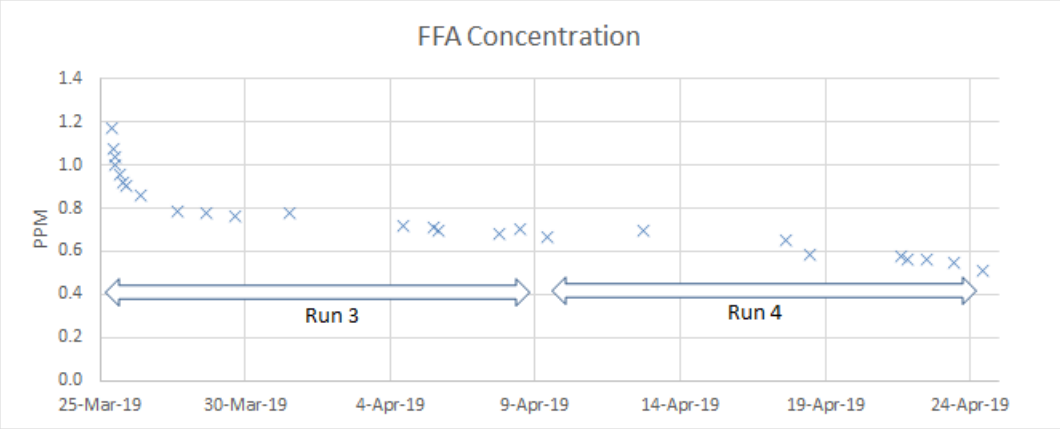

Figure 4.13: Measured loop FFA concentration for Runs 3 and 4

The pellet was exposed for 336 hours under jet impingement conditions where a dissolved crater area was found with a diameter of 1.1 mm as seen in Figure 4.15. The dissolution patterns seemed to follow a radial flow pattern with dissolution pits seen in the higher magnification pictures with a maximum depth of dissolution of 120 μm. At the edge of the dissolution area, the surface of the pellet is covered with hematite precipitates with the underlying original surface showing no signs of dissolution. The hematite precipitates could be explained by spikes in oxygen when the test section is valved into the experimental loop and is not detected by the oxygen sensor or oxygen measurements via Chemets dissolved oxygen measuring kits. Determining if the FFA was adsorbed during the aggressive jet impingement conditions was done with a hydrophobicity test. As seen in Figure 4.16 the magnetite surface shows a hydrophobic surface indicating the presence of an adsorbed film. The

pellet from Run 1.3 was used for comparision and showed a hydrophilic surface.

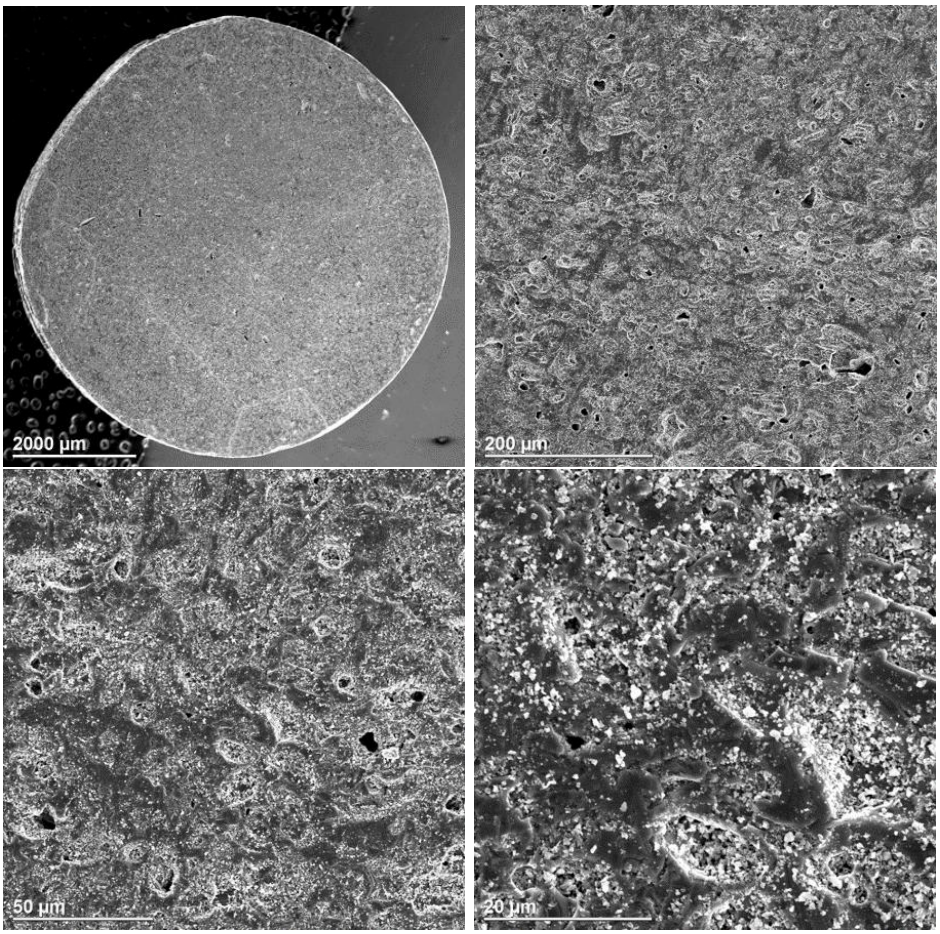

Figure 4.14: Magnetite pellet before exposure in Run 3

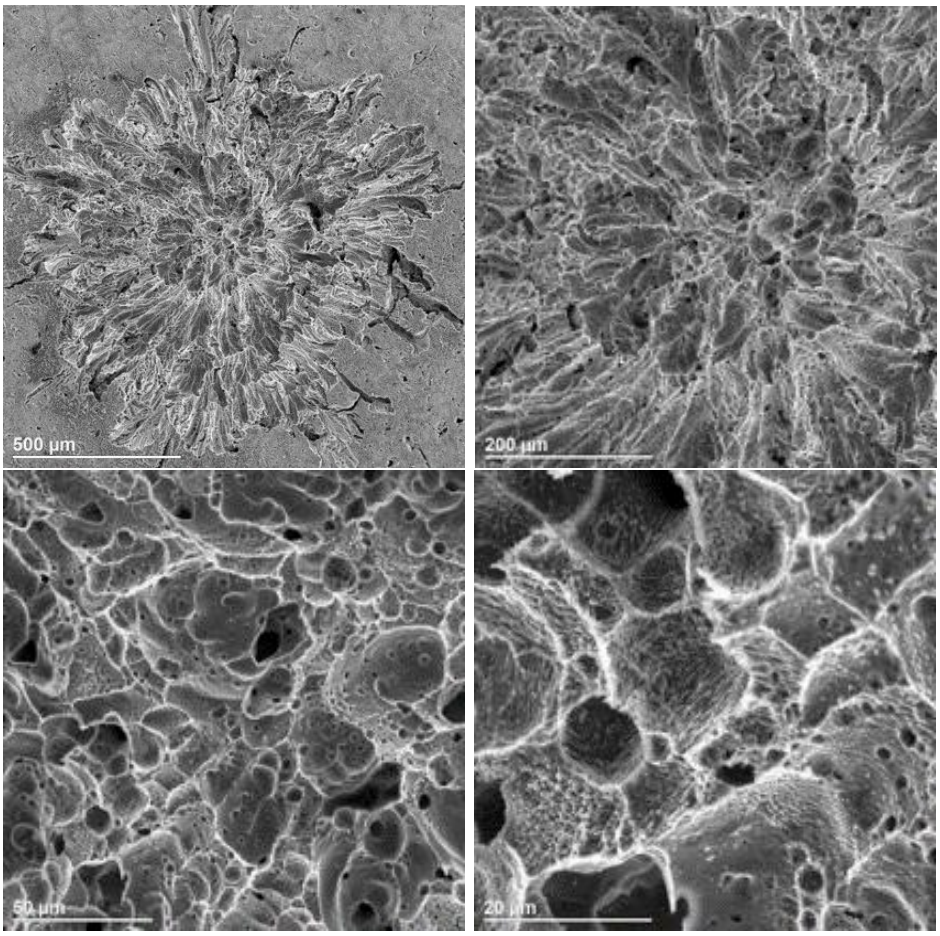

Figure 4.15: Magnetite pellet after exposure in Run 3

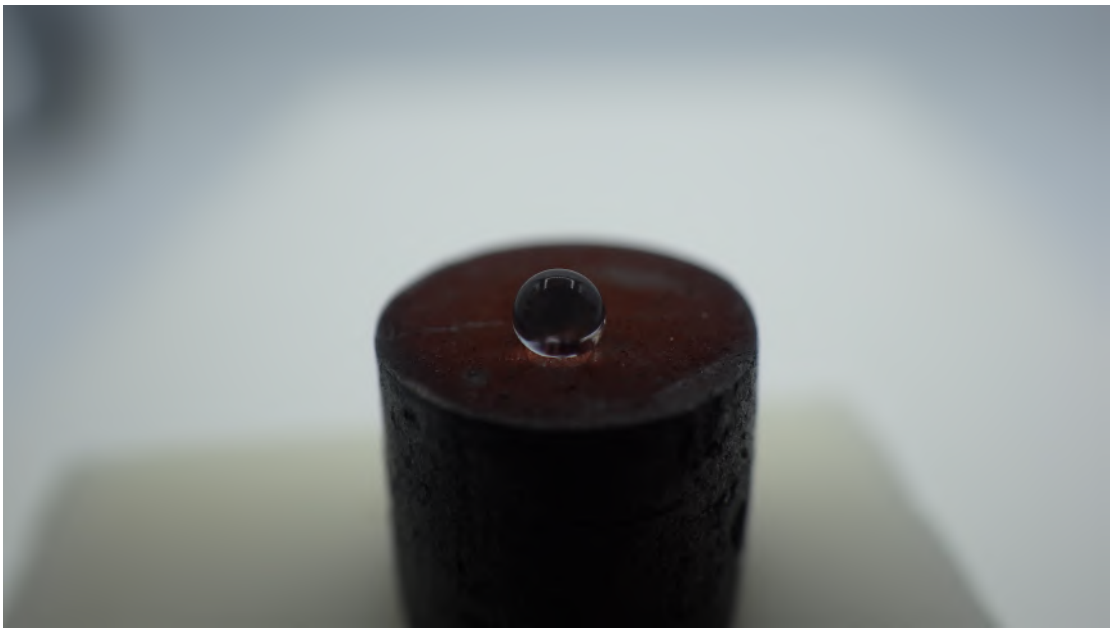

Figure 4.16: Hydrophobic magnetite pellet surface after Run 3

4.4 Run 4: $pH_{25°C}$ Neutral, 140°C, Cetamine® V219 equilibrium, flow rate 4.0 mL/s, exposure time 336 hours, sinter at 1300°C for ten hours

Run 4 was completed after Run 3 to investigate the effect of FFA on the dissolution rate constant of magnetite during the equilibrium concentration of the FFA, seen in Figure 4.13. After the initial injection phase of the Cetamine® V219, the concentration will remain constant unless the surface area of the experimental loop increases or is removed with the use of the ion-exchange column. The magnetite pellet used for Run 4 was sintered at 1300°C for 10 hours and was exposed to jet impingement for 336 hours at 140°C with argon being used as the purging gas for oxygen control. The CHA component caused the coolant pH to be slightly increased from neutral

conditions, which will cause a slight decrease in the magnetite solubility. The post-exposure SEM pictures of the magnetite pellet can be seen in Figure 4.17 where a dissolved crater of 1 mm diameter developed. The radial dissolution patterns with dissolution pits have a very similar appearance to the dissolution of Run 3 but only indicates a maximum dissolution depth of 100 μm. At the edge of the dissolution area, hematite precipitates are covering the underlying magnetite surface with no signs of dissolution of the original magnetite surface. In Figure 4.18, the hydrophobic magnetite surface can be seen, which suggests the absorbed film is present on the surface.

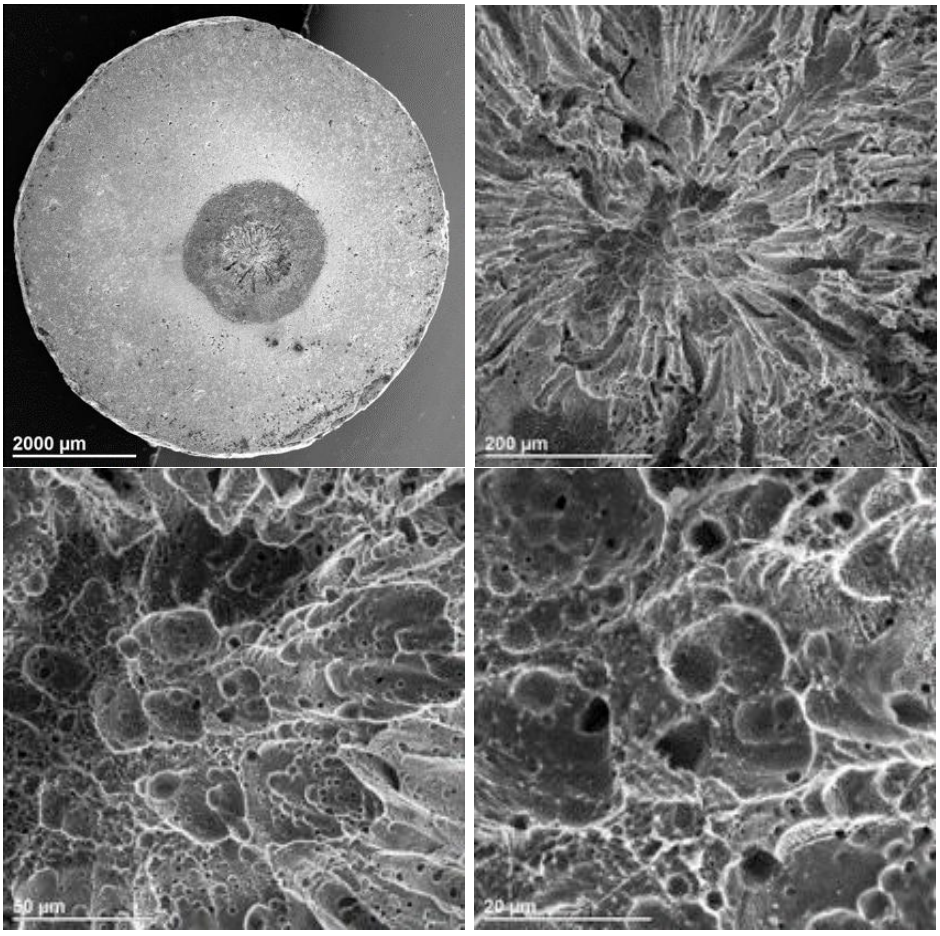

Figure 4.17: Magnetite pellet after exposure in Run 4

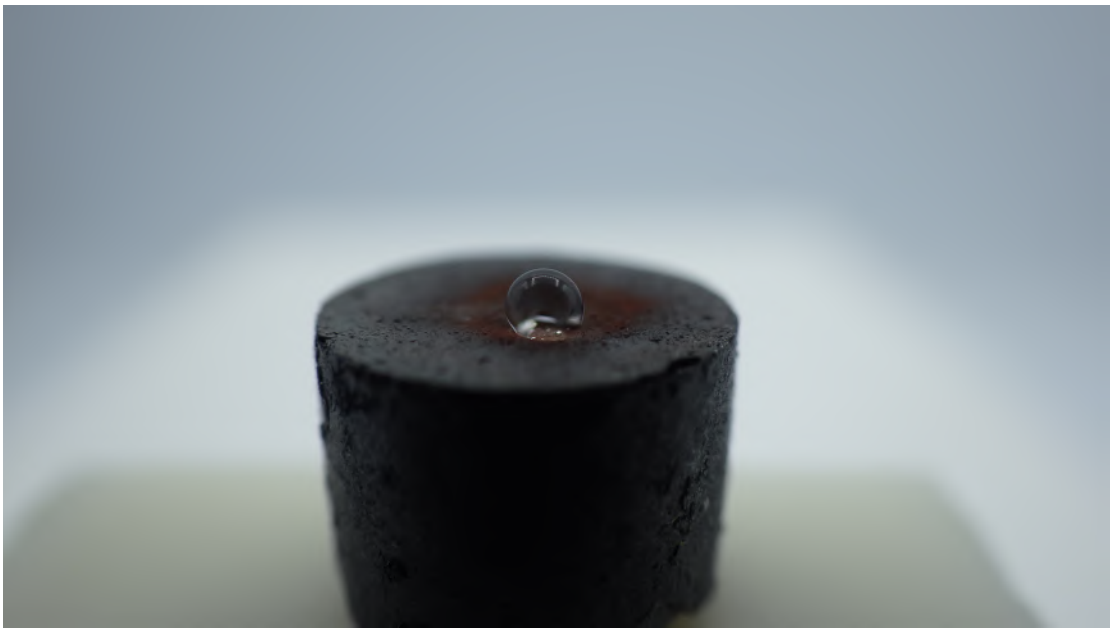

Figure 4.18: Hydrophobic magnetite pellet surface after Run 4

4.5 Run 5: $pH_{25°C}$ Neutral, 140°C, Cetamine® V219 equilibrium, flow rate 3.0 mL/s, exposure time 336 hours, sinter at 1300°C for five hours

Run 5 was completed to further investigate the effects of film-forming amines on the dissolution rate constant of magnetite but at typical feedwater conditions and not the neutral conditions used in the previous experiments. The $pH_{25°C}$ was 9.2 and controlled by ammonia at 140°C, while argon was used as the purging gas to control oxygen for the duration of the experiment. Run 5 was completed at the equilibrium phase of the Cetamine® V219 injection and FFA measurements could only be taken every 3-4 days to preserve the 60L recirculating water supply. The measured FFA concentration throughout the experiment can be seen in Figure 4.19. The same pel-

let that was used in Runs 1.3 and 2.2 was used for this experiment and was exposed to jet impingement conditions for 336 hours. The post-exposure SEM pictures seen in Figure 4.20 show no measurable dissolution of the magnetite pellet which was expected due to the already low magnetite solubility at this condition. As seen in Figure 2.21 the FFA was absorbed on the pellet surface to create a hydrophobic surface that proved to further protect the magnetite from dissolution. The magnetite pellet only shows a slightly hydrophobic surface unlike the surface in Runs 3 and 4. This is important in corrosion research as these FFAs can significantly decrease the corrosion of power generating station components. This study could be completed over a longer duration to show a removal that is above the measurable limit with SEM and profilometry techniques.

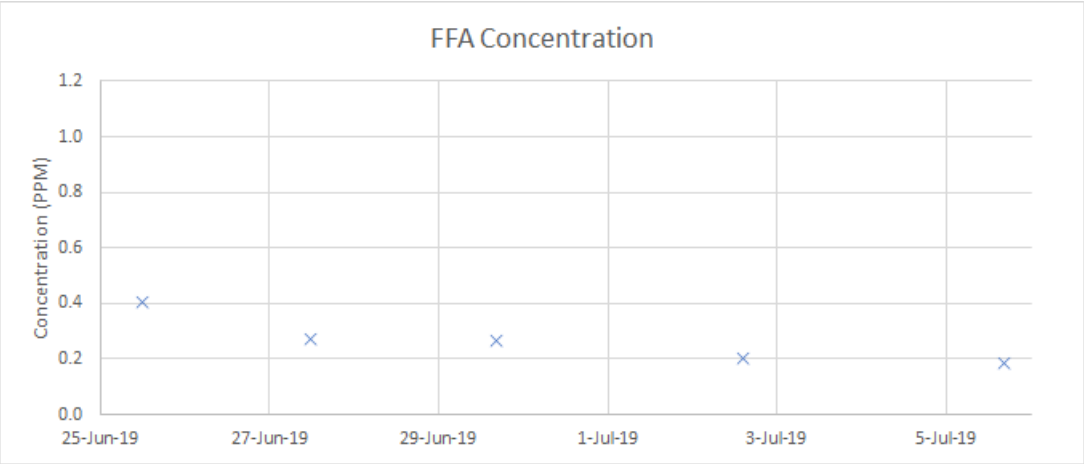

Figure 4.19: Measured loop FFA concentration for Run 5

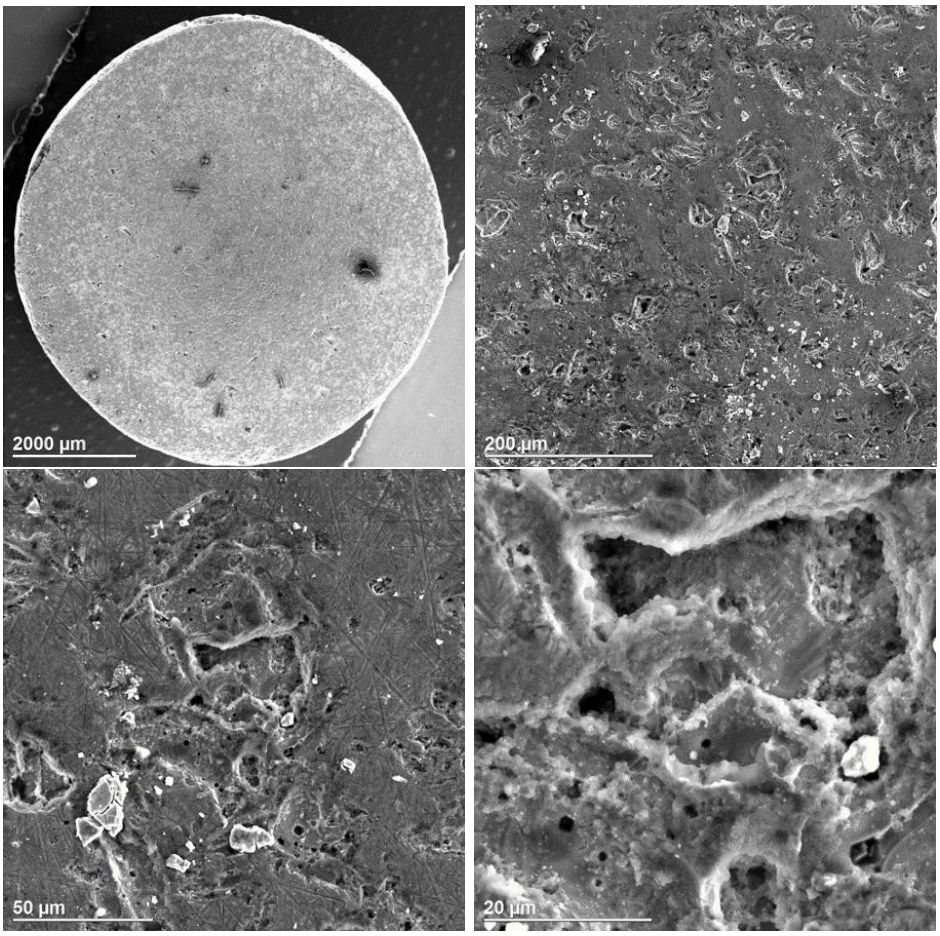

Figure 4.20: Magnetite pellet after exposure in Run 5

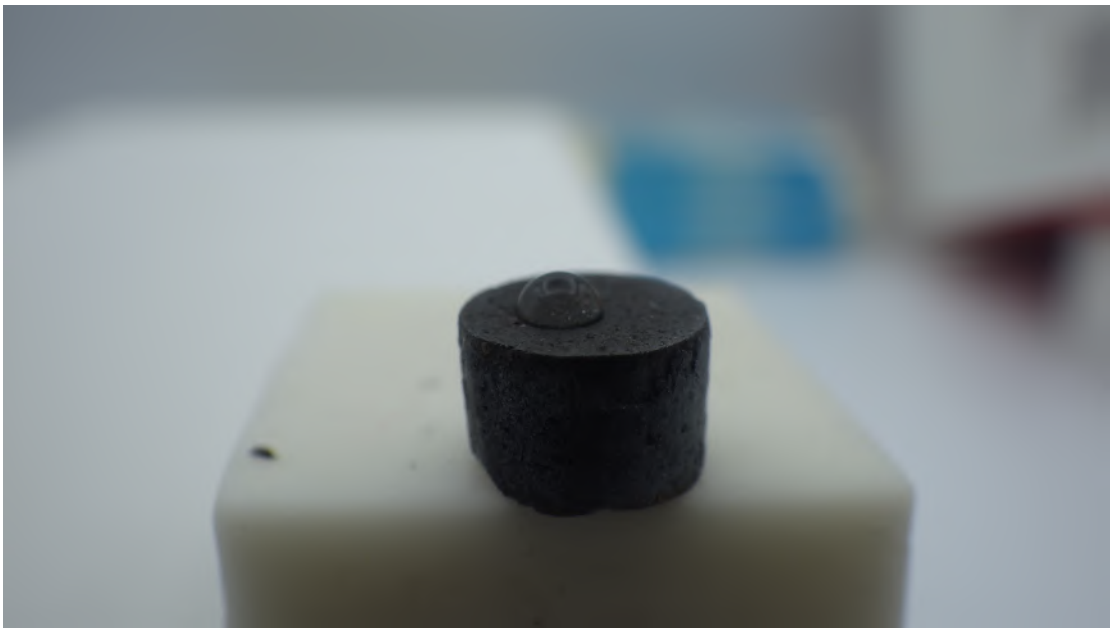

Figure 4.21: Hydrophobic magnetite pellet surface after Run 5

4.6 Mass Transfer Calculations

The mass transfer coefficient must be calculated to ensure that the overall removal of magnetite is dissolution controlled. With Equation 2.10 the dissolution rate constant can be calculated by measuring the overall removal rate constant. The overall removal rate constant is calculated with Equation 2.9 by having the bulk iron concentration (assumed to be zero) and the saturation concentration (solubility) of the coolant, which is extracted from [51]. There are several empirical mass transfer coefficients for a submerged jet, and it is essential to use a correlation that is valid for a large range of Reynolds numbers, is of simple form and shows no strong deviations from experimental data. Equation 2.18 was used to determine the theoretical mass transfer coefficient where the dissolution experiment fits the wide range of parameters studied for the empirical correlation. Detailed calculations for the mass transfer

coefficient can be found in Appendix A with a summary of the results displayed in Table 4.1.

Table 4.1: Mass transfer coefficient for jet impingement experiments

Run No.	Temp (°C)	Jet Velocity (m/s)	Reynolds Number	k_m (mm/s)
1.1	140	11.9	28000	6.15
1.2	140	9.5	22000	5.21
1.3, 2, 3, 4	140	20.4	48000	9.22
2.2, 5	140	15.3	36000	7.43

4.7 Dissolution Rate Constant Calculation

Table 4.2 summarizes the calculated dissolution rate constant for all jet impingement experimental runs from Equations 2.9 and 2.10, where the mass transfer coefficients can found in Table 4.1.

Table 4.2: Dissolution rate constant for jet impingement experiments

Run No.	Temperature (°C)	$pH_{25°C}$	Solubility (ppb)	Dissolution Rate (g/cm^2s)	k_d (mm/s)
1	140	9.2	13	4.88E-11	0.037
[1]2	140	9.2	13	2.94E-11	0.022
[2]3	140	Neutral	129	1.06E-8	0.76
[3]4	140	Neutral	129	8.48E-9	0.61
[3]5	140	9.2	13	< measurable limit	

[1] $[N_2H_4]$ = 200 ppb

[2] FFA Injection

[3] FFA Equilibrium

Run 1 at a pH of 9.2 at 140°C led to discovering problems with the quality of sintering that had been a problem in previous jet impingement studies. With the low solubility of magnetite at this condition a large crater still developed due to the granular interior of the pellet in Runs 1.1 and 1.2. These values are not used for dissolution rate constants and differ greatly from the values found from properly sintered magnetite oxide pellets. The granular pellets used in Runs 1.1 and 1.2 show 160 times larger removal rates than seen in Run 1.3. The erosion of granular pellets will be further discussed in Section 4.9. No quantitative measurement of the dissolution rate could be completed for Run 1.3 as the dissolution is very small with only subtle decreases in the depth of the polishing lines detected with SEM pictures. The roughness of the pellet before exposure over several chords was measured and compared to the roughness after exposure in the affected area. A measured chord was the length from one side of the dissolution area to the other and was measured with the profilometer.

From SEM pictures and roughness measurements it was estimated that the pellet had an average of 0.15 μm decrease in height over the affected area. The dissolution rate constant value of 0.037 mm/s can be compared to the work of Mohajery [6] of 0.03 mm/s to find a $\pm$ 0.007 mm/s difference between the two studies at the same conditions.

Run 2 showed two drastically different results for Runs 2.1 and 2.2. For Run 2.1, it was assumed that an unknown factor caused the large mound of hematite to form at the center of the pellet and then a large dissolution area to form around this mound. Run 2.2 showed similar results to previous experiments completed with very little dissolution and was used to determine the dissolution rate constant at this condition. Similar to Run 1.3, no quantitative measurement of the dissolution could be completed as only subtle changes in the depth of the polishing lines could be detected by the SEM photos. By measuring the roughness of several chords before and after the jet impingement experiment and using the SEM photos it was assumed that the pellet had an average of 0.05 μm decrease in height over the affected area. The dissolution rate constant of 0.022 mm/s can be compared to the work of Mohajery [6] of 0.02 mm/s to find a $\pm$ 0.002 mm/s difference between the two studies at the same conditions. A comparision of Runs 1 and 2 with the work of Mohajery is presented in Table 4.3.

Table 4.3: Dissolution rate constant comparision with Mohajery [6]

$pH_{25^\circ C}$	Temperature (°C)	[O2] (ppb)	kd (Mohajery) (mm/s)	kd (Turner) (mm/s)	Error (± mm/s)
[1]9.2	140	0	0.03	0.037	0.007
[2]9.2	140	0	0.02	0.022	0.002

[1] Controlled with ammonia

[2] Controlled with ammonia and hydrazine

The results found from this study are very similar to the results that Mohajery found at typical feedwater conditions with a small absolute error between the two measured dissolution rate constants. The two studies were completed in a reliable manner to produce similar results that can now be used reliably in FAC models. To improve the reliability of the dissolution studies for Runs 1 and 2, the study must be completed over a duration that will provide easy to measure dissolution. The results from Mohajery and this study were estimates from SEM photos and by measuring the roughness before and after exposure. Hematite was present on the magnetite surface for all of these runs, which could act as a source of error by covering possible dissolved areas on the pellet surface. Sasaki and Burstein [53] used a fluid jet system to measure the erosion-corrosion of 304L stainless steel and found that the steel experienced oxidizing potentials, with the highest potentials during the beginning of the experiment. They found this result by measuring the open-circuit potential, which was also completed by Mohajery to find a similar result where the potentials peak near the beginning of the experiment. This oxidizing potential could cause the formation of hematite on the pellet surface.

Runs 3 and 4 dissolution was measured by measuring the dissolved area profile

at 50 μm intervals and determining the volume of removed magnetite oxide. The solubility for neutral conditions was used for both of these runs even though the $pH_{25^\circ C}$ was slightly raised to 7.65-7.70 due to the addition of Cetamine® V219 to the loop coolant. The solubility at neutral conditions (pH 6-8) remains relatively constant and is shown in Figure 2.14. Both Runs 3 and 4 can be compared to a study completed by Mohajery at the same chemistry conditions without the addition of FFA to determine their effect on the dissolution rate of magnetite. Run 3 ($k_d = 0.76$ mm/s) and Run 4 ($k_d = 0.61$ mm/s) show a decrease of 65% and 72% respectively from Mohajery's measured dissolution rate constant of 2.2 mm/s. This large decrease in the dissolution rate constant shows the effectiveness of decreasing the dissolution rate of magnetite with the addition of film-forming amines. The addition of FFA has been shown to protect the oxide surface by significantly decreasing the dissolution rate of magnetite at neutral conditions where the solubility is 10 times higher than typical feedwater conditions. The dissolution rate at feedwater conditions is very small, therefore any reduction will significantly reduce the FAC rate in generating plants.

Run 5 was completed at feedwater conditions with the addition of FFA to determine if the dissolution rate can be decreased further, which will be useful in reducing FAC rates. At these conditions the magnetite pellet was found to have an even smaller dissolution then Run 2.2 and was therefore assumed to be below the measurable limit. This proves that the addition of FFA will reduce the dissolution rate at feedwater conditions but does not show the amount of decrease in the dissolution rate. The experiment must be run over a much larger duration to determine the amount that the FFA reduce the dissolution rate constant of magnetite at $pH_{25^\circ C}$ 9.2 and 140°C. This shows a promising result for future dissolution studies and FAC research.

4.8 Computational Fluid Dynamics

Numerical simulations were completed to study the hydrodynamics of the impinging jet study that was used to experimentally measure the dissolution of magnetite. This was done to understand the flow and how the test section design affects the flow characteristics over the pellet. The flow rates varied from study to study and were all simulated using Ansys CFX software to determine the fluid velocity and shear stress profiles on the pellet's surface. The modelled shear stress values were used in Section 4.8 to model the effect of erosion of the overall magnetite removal.

The mesh was created using Pointwise software with structural mesh making up a majority of the fluid domain and non-structural mesh in the complicated geometry areas. A total of 4071979 nodes and 5398940 elements were created to model the jet impingement flow. At the pellet surface the first node was created with a thickness of 0.025 mm with 40 nodes in the 1 mm region above the pellet to model the boundary layer flow.

There are several turbulence models to simulate the effects of the turbulent flow created from the impinging jet. Shear Stress Transport (SST) was chosen due to being shown to produce the best results in simulating the impinging jet flow and predicting heat transfer coefficients [52]. The shear stress transport model combines the advantages of the $\kappa - \epsilon$ and $\kappa - \omega$ with a blending function that activates the $\kappa - \epsilon$ model in the core of the flow and changes to the $\kappa - \omega$ model for the near wall region of the flow.

Shear stress profiles were created for each experiment depending on the mass flow rate that varied over a majority of trials. Figure 4.22 shows how an increase in the mass flow rate and the jet velocity causes an increase in the shear stress over the magnetite pellet surface.

Figure 4.23 shows the crater profile from Run 1.2 superimposed over the shear stress

profile obtained by CFD simulation. The position of maximum shear stress matches with the position of maximum crater depth for the poorly sintered pellet.

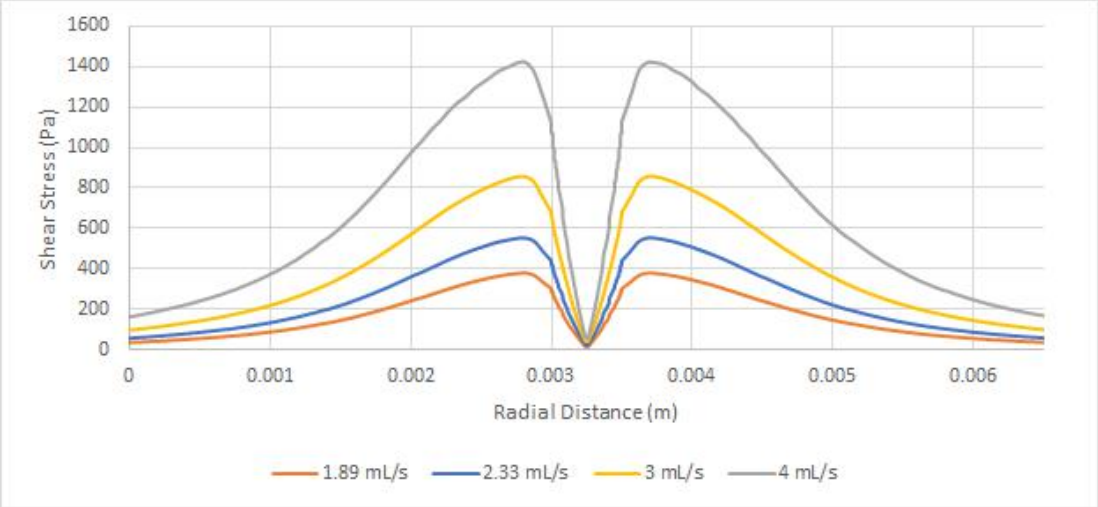

Figure 4.22: Shear stress profile along radial distance at 140 degrees at varying jet velocities

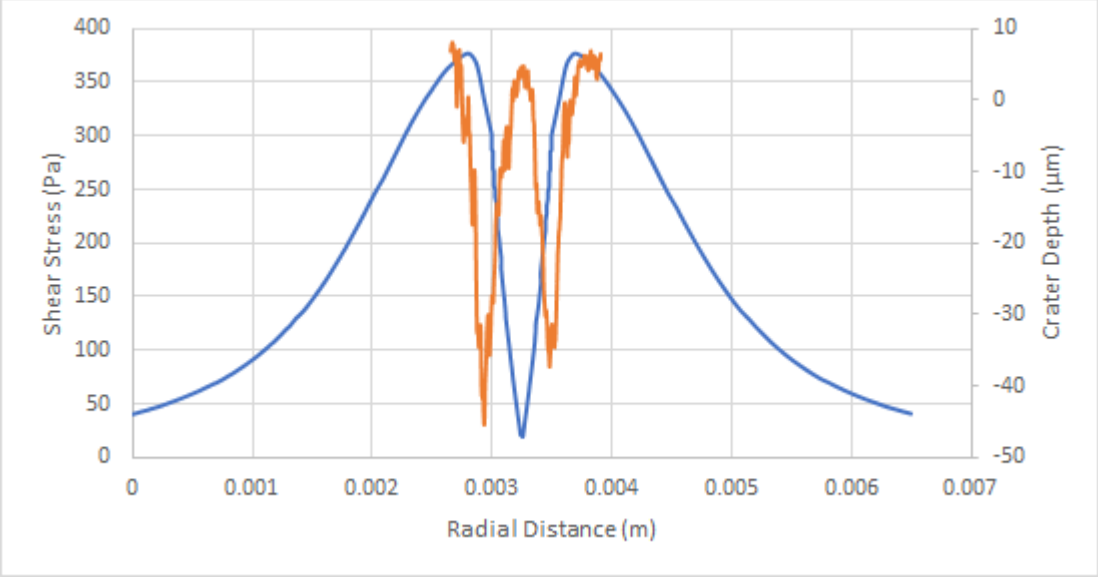

Figure 4.23: Crater profile superimposed over shear stress profile in Run 1.2

Figure 4.24 shows the velocity vectors for the CFD simulation of Run 1.1, with the

magnitude of the velocity vectors being the only difference between each Run. The velocity vectors have been normalized to simplify the figure and therefore the magnitude of the velocity is determined by the colour of each vector. The left-hand side shows a very similar flow pattern to the right-hand side even though it is the dead-end side of the test section. The large amount of flow circulation that can be seen in Figure 4.24 creates many problems in simulating jet flow as the re-circulating flow can cause the solution to become unstable with too large of a time step. In order to produce a stable solution an upwind scheme must be used while initially using a time step of 1E-6 and gradually increasing to 1E-4, to develop the flow while maintaining a stable solution. An upwind scheme uses the value upstream to evaluate a property on the boundary of the node and then use them to compute the value at the center of the cell and is designed for strong convective flows. The minimum hydrodynamic boundary layer thickness occurs at r/d_0=1.6 according to Figure 4.24, that corresponds to [13], that the minimum boundary layer thickness will fall between r/d_0=1 and r/d_0=2.

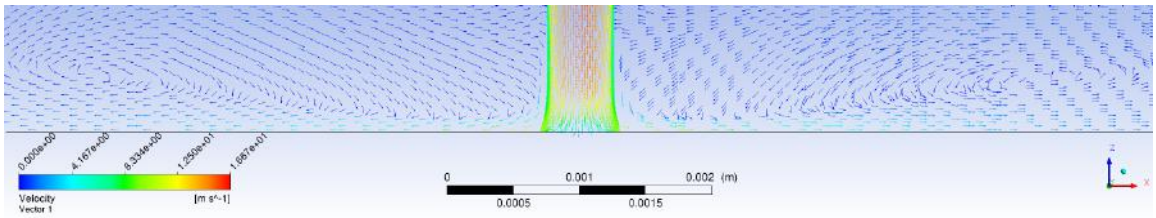

Figure 4.24: ANSYS CFX velocity vectors of jet impingement test section

To determine the quality of the CFD model the pressure drop from the simulations can be compared to actual pressure data collected during the experimental runs. The CFD simulation predicted a pressure drop over the test section of 29 psi with the actual measured pressure drop of 37 psi. This correlates to a percent difference

of 19% between the actual measured value and the simulated CFD model.

4.9 Erosion Modeling

The largest source of error during jet impingement dissolution experiments of magnetite oxide comes from the quality of the sintering of the magnetite pellets. The recommended temperature and conditions for the sintering of magnetite provided poorly sintered pellets that cause a large increase in the removal rate due to the erosion of granular magnetite. The dissolution rates differ greatly between Runs 1.1 (7.94E-9 g/cm^{2}s) and 1.3 (4.88E-11 g/cm^{2}s) with the interior structure of the two pellets being the difference between the two experiments that can be compared in Figure 4.3 and 4.7. To model and estimate the effect of this erosion, a similar approach has been used by Lang [23] and Phromwong [24] to understand the effects of erosion in FAC. Mohajery [6] used the same model to understand these effects on the jet impingement study.

To use this model, the shear stress of the impinging jet is needed as was found in Section 4.7. In this model, it is assumed that the dissolution rates measured in small grain pellets are the sum of the removal from dissolution and the removal of particles due to erosion. This is shown in Equation 4.1.

$$k\Delta C = k_d \Delta C + \frac{\rho f \Sigma_{i=1}^{J} \frac{\pi}{6} (d_i)^3}{Area * t_{total}} \tag{4.1}$$

where $\Delta C = C_{eq} - C_{bulk}$ (C_{bulk} assumed to be zero), d_i is the diameter of spherical particle number i (cm), ρ is the density of magnetite (g/cm^3), $f = 0.723$ (weight proportion of iron in magnetite), $Area$ is the area over which the dissolution takes place (cm^2), and t_{total} is the total time of the experiment (s).

The term on the left is the total measured removal rate where the first term on the

right side is the contribution from the dissolution where k_d is the dissolution rate constant measured with a well-sintered pellet. The second term on the right hand side of Equation 4.1 is the estimate for the removal of particles due to erosion. To estimate the effect of erosion it was assumed that the particles varied between 0.2-5 μm for Run 1.1 and between 2-10 μm for Run 1.2. This was estimated with the use of ImageJ and the SEM pictures of the interior of each pellet. A random number generator, using a half-normal probability distribution, was used to determine the size of the particle removed at any instant. The smaller the particle, the higher the probability that the particle will be removed. The spalling time, or the time to remove the given particle is given by Equation 4.2. Figure 4.25 shows the half-normal probability distribution and the amount of removed particles based on the size of each particle. The spalling time is also shown to increase parabolically as the size of the particle increases.

$$\theta_i = g * \frac{d_i^2}{\tau k_d C_{eq}} \tag{4.2}$$

where θ_i is the spalling/ erosion time of particle i (s), τ is the shear stress (Pa) and g is the spalling time constant (g·Pa/cm^4). The spalling times are summed until their time reaches the total experiment time.

$$\Sigma_{i=1}^{J} \theta_i = t_{total} \tag{4.3}$$

Equations 4.1, 4.2 and 4.3 were solved simultaneously to determine the spalling time contant and the total number of removed particles seen in Equations 4.7 and 4.8 respectively. To solve these equations the volumetric mean diameter (d_{30}), surface mean diameter (d_{20}) and volume/surface mean diameter (d_{32}) must be introduced

and are defined by Equations 4.4, 4.5 and 4.6.

$$d_{30}^3 = \int_0^\infty d^3 f(d) dd = \Sigma_{i=1}^n d_i^3 f(d) \Delta d \tag{4.4}$$

$$d_{20}^2 = \int_0^\infty d^2 f(d) dd = \Sigma_{i=1}^n d_i^2 f(d) \Delta d \tag{4.5}$$

$$d_{32} = \frac{d_{30}^3}{d_{20}^2} \tag{4.6}$$

where d_{30} is the volumetric mean diameter (cm), d_{20} is the surface mean diameter (cm), d_{32} is the volume/surface mean diameter (cm), $f(d)$ is the probability distribution function of particles (cm^{-1}) and Δd is the change in the particle diameter (cm). These diameter values are used to replace d_i and describe the particles by providing a mean value that is related to the surface area or volume. The Sauter Mean Diameter (D_{32}) is larger then the arithmetic mean and will provide a better characterization of the mean particle diameter due to surface area being an important parameter in the overall erosion process.

$$g = \frac{\pi d_{32} \rho f \tau k_d}{6 * Area(k - k_d)} \tag{4.7}$$

$$N = \frac{t_{total} \tau k_d \Delta C}{d_{20}^2 g} \tag{4.8}$$

where N is the total number of particles removed during the experiment. The detailed Matlab code can be referenced in Appendix C.

For Run 1.1 an average shear stress of 330 Pa was found from the CFD model to find a spalling time constant of 0.108 g·Pa/cm^4, that resulted in a total number of 1.23E7 particles removed during the total time of the experiment (672 hours). This resulted in an average removal depth of 50.8 μm for a removal of 2.51E-4 grams, where the measured mass of magnetite removal was 2.17E-4 grams. The mass loss over time

is seen in Figure 4.26, which shows a linear removal of magnetite due to erosion. Over short duration (minutes) the mass loss will be random due to the spalling time of each particle size but over the duration of an experiment the mass loss follows a linear behaviour. For Run 1.2 an average shear stress of 230 Pa was found from the CFD model to find a spalling time constant of 0.091 g·Pa/cm^4, that resulted in a total number of 3.63E6 particles removed during the total time of the experiment (240 hours). This resulted in an average removal depth 19.8 μm for a removal of 8.08E-5 grams, where the measured mass of magnetite removal was 5.89E-5 grams. The dissolution does not contribute very much as its rate is two orders of magnitude smaller then the overall removal rate. This program overestimates the mass loss of the magnetite pellet due to erosion, as the initial stages of sintering will slightly protect the pellet surface from erosion.

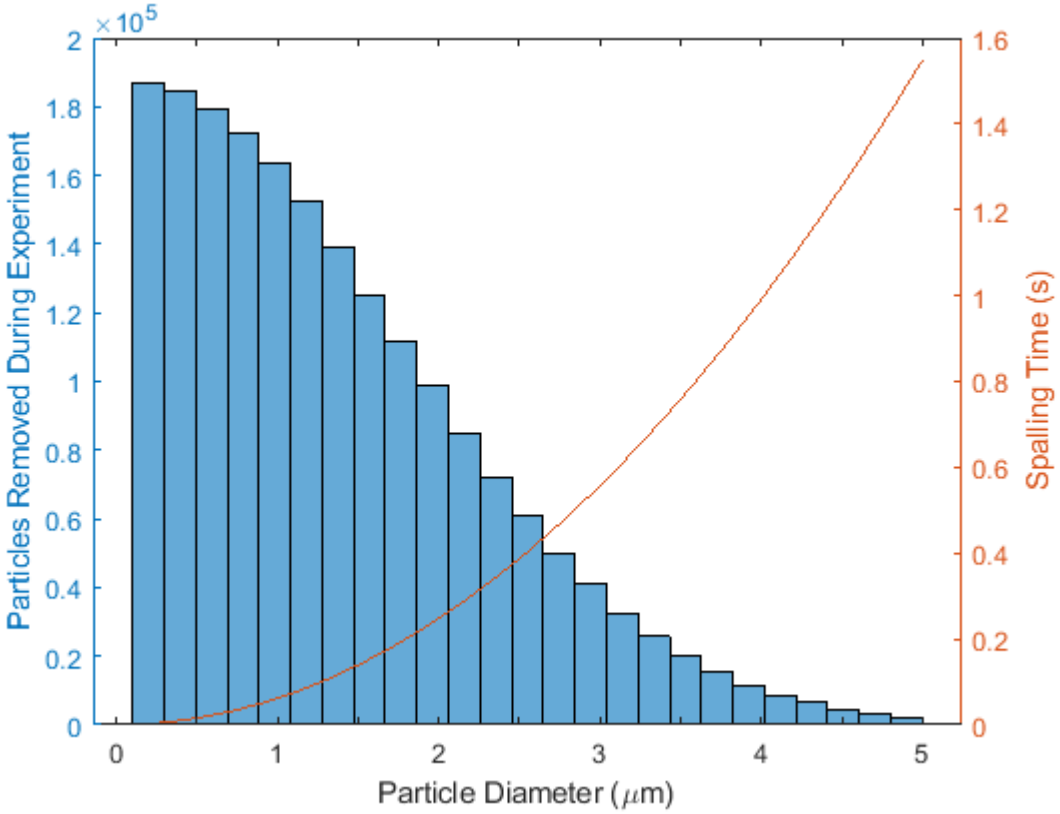

Figure 4.25: Half-normal probability distribution and the corresponding spalling times for Run 1.1

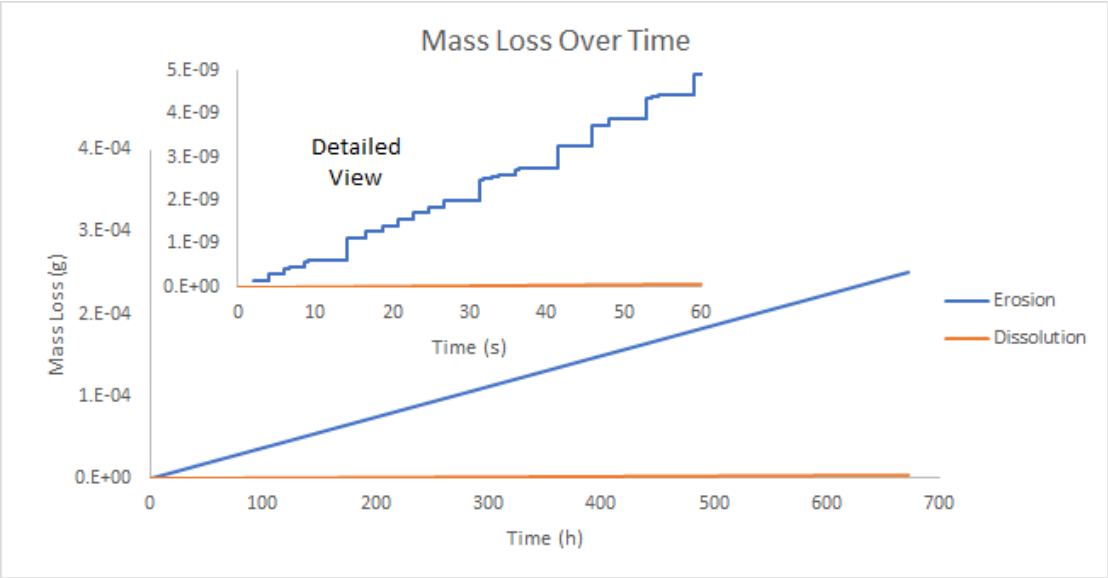

Figure 4.26: Predicted mass loss over time from the erosion MATLAB program for Run 1.1

Chapter 5

Conclusions

To determine the dissolution rate constant of magnetite at various chemistry conditions at 140°C, jet impingement experiments over a sintered magnetite pellet were completed. The chemical conditions tested during this study included the typical feedwater coolant conditions for CANDU and PWR systems. Measuring the volume of dissolved magnetite with the use of a profilometer proved to be sensitive enough for a majority of the experimental runs. From the results collected the following conclusions could be made:

- 1300°C with a heating/cooling rate of 20°C/min for a duration of 10 hours under an argon atmosphere was found to be the optimum parameters to sinter small grain (0.1-0.5μm) magnetite pellets to withstand the erosion of discrete particles created from jet impingement dissolution studies. The consistency of the pellets varies depending on the sintering parameters and has a large influence on the measured dissolution rate constant. Poorly sintered pellets showed a removal rate of roughly 160 times higher than properly sintered pellets due to particle removal due to erosion. Only well-sintered pellets should be used for reliable dissolution values.

- The dissolution rate constant of magnetite in ammoniated water chemistry with a $pH_{25^\circ C}$ of 9.2 and at 140°C was found to be 0.037 mm/s with a dissolution rate of 4.88E-11 g/cm^{2}s.

- The addition of high levels of hydrazine in ammoniated chemistry at 140°C resulted in a lower dissolution rate constant of 0.022 mm/s with a dissolution rate of 2.94E-11 g/cm^{2}s. This agrees with results from FAC studies as the addition of hydrazine in an absence of oxygen reduced the FAC rate but increased the FAC rate with oxygen present due to the reduction in oxidizing potential [54].

- The addition of FFAs at neutral pH conditions and at 140°C resulted in a dissolution rate constant of 0.76 mm/s and a dissolution rate of 1.06E-8 g/cm^{2}s for the initial injection phase of the FFA addition. For the equilibrium level of FFA concentration a dissolution rate constant of 0.61 mm/s and a dissolution rate of 8.48E-9 g/cm^{2}s was found. These results show a 65% and 72% reduction in the dissolution rate constant compared to a dissolution experiment by Mohajery [6] at the same chemistry conditions with no FFA addition. This results shows a significant decrease of the dissolution rate of magnetite and shows the protective nature of the FFA on the oxide surface. The higher dissolution rate constant during the FFA injection phase is due to the film taking multiple days to form on the loop and pellet surface.

- The addition of FFA at a $pH_{25^\circ C}$ of 9.2 and at 140°C caused a reduction in the dissolution rate constant to a point that was below the measurable limit. This study should be completed over a longer duration to create measurable results.

Chapter 6

Recommendations

The following recommendations on this experimental study based on the results are:

- The dissolution experiment could be completed at a wider range of conditions that are not typical of feedwater conditions for CANDU and PWR systems.
- The dissolution experiment could investigate different oxides such a nickel ferrite and investigate the effects of the addition of chromium to the magnetite oxide.
- A non-destructive testing method should be applied to the pellets to determine their quailty of sintering before exposing them in an experimental run.
- Single crystals could be used instead of sintered pellets to remove an erosion effect for the jet impingement flow although Mohajery found very little difference between a single crystal and a well sintered pellet. The single crystal was more difficult to acquire, to mount, and its purity was suspect.

References

[1] H. Abe, *Characteristics of Scalloped Surface and its Relation to FAC Rate of Carbon Steel Piping Elbow*. The Japan Society of Mechanical Engineers No. 847, Vol. 83, pp. 16-00453, 2017

[2] M. Vepsäläinen, *Magnetite dissolution and deposition in NPP secondary circuit*. VTT technical Research Centre of Finland, 2010

[3] P.V. Balakrishnan, *A Radiochemical Technique for the Study of Dissolution of Corrosion Products in High Temperature Water*. The Canadian Journal of Chemical Engineering No. 3, Vol. 55, pp. 357-360, 1977

[4] R.W. Tizzard, E.J. Dewar, A.L. Crandlemire, *Magnetite Solubility and Dissolution Rate Measurement*. Nova Scotia Research Foundation Corporation, 1981

[5] L.D. de Pierrefeu, *The Dissolution Behaviour of Magnetite Electrodes in High-Temperature Water*. Master's Thesis, University of New Brunswick, Chemical Engineering Dept., 2009

[6] K.M. Moghaddam, *The Dissolution Rate Constant of Magnetite in Water at Different Temperature and pH Conditions*. Doctor of Philosophy Thesis, University of New Brunswick, Chemical Engineering Dept., 2014

[7] NASA, *Corrosion Control and Treatment Manual.*, 1994

[8] R. Dooley, V. Chexal, *Flow-Accelerated Corrosion of Pressure Vessels in Fossil Plants.* International Journal of Pressure Vessels and Piping No. 2-3, Vol. 77, pp. 85-90, 2000

[9] V. Kain, *Flow Accelerated Corrosion and its Control Measures for the Secondary Circuit Pipelines in Indian Nuclear Power Plants.* Journal of Nuclear Materials No. 1-2, Vol. 383, pp. 86-91, 2008

[10] H. Okada, S. Uchida, M. Naitoh, J. Xiong, S. Koshizuka, *Evaluation Methods for Corrosion Damage of Components in Cooling Systems of Nuclear Power Plants by Coupling Analysis of Corrosion and Flow Dynamics (V) Flow-Accelerated Corrosion under Single- and Two-phase Flow Conditions.* Journal of Nuclear Science and Technology, Vol. 48, pp. 65-75, 2011

[11] D.H. Lister, *A Fundamental Study of Flow-Accelerated Corrosion in Feedwater Systems.* Power Plant Chemistry, Vol. 10, pp. 659-667, 2008

[12] B. Villien, Y. Zheng, D.H. Lister, *The Scalloping Phenomenon and its Significance in Flow-Assisted-Corrosison.* in Proceedings of the Twenty Sixth Annual CNC-CNA Student Conference, Toronto, 2011

[13] K.D. Efird, *Jet Impingement Testing for Flow Accelerated Corrosion.* Corrosion 2000, paper 52, 2000

[14] A.J. Bird, *Effects of Surface Morphologies on Flow Behavior in Karst Conduits.* in Proceedings of 15th International Congress of Speleology, Texas, pp. 1417-1421, 2009

[15] D.H. Lister, P. Gauthier, J. Goazczynski, J. Slade, *The Accelerated Corrosion of CANDU Primary Piping*. in Proceedings of JAIF International Conference on Water Chemistry in Nuclear Power Plants, Japan, 1998

[16] E.C. Potter, G.M.W. Mann, *The Fast Linear Growth of Magnetite on Mild Steel in High-Temperature Aqueous Conditions*. British Corrosion Journal, Vol. 1, pp. 26-35, 1965

[17] J.E. Castle, H.G. Masterson, *The Role of Diffusion in the Oxidation of Mild Steel in High Temperature Aqueous Solutions*. Corrosion Science No 3-4, Vol. 6, pp. 93-96, 1966

[18] G.J. Bignold, R. Garnsey, G.M.W. Mann, *High Temp. Aqueous Corrosion of Iron Development of Theories of Equilibrium Solution Phase Transport Through a Porous Oxide*. Corrosion Science No.4, Vol. 12, pp. 325-326, 1972

[19] J. Robertson, *The Mechanism of High Temperature Aqueous Corrosion of Steel*. Corrosion Science No. 11-12, Vol. 29, pp. 443-465, 1989

[20] B. Dooley, D.H. Lister, *Flow-Accelerated Corrosion in Steam Generating Plants*. Power Plant Chemistry No. 4, pp. 194-244, 2018

[21] D.H. Lister, *Corrosion Products in Power Generating Systems*. in Proceedings of International Conference on Fouling of Heat Transfer Equipment, pp. 135-200, Troy, New York, 1979

[22] G.J. Bignold, C.H.D. Whalley, K. Garbett, I.S. Woolsey, *Mechanistic Aspects of Erosion-Corrosion Under Boiler Feedwater Condition*. Water Chemistry of Nuclear Reactor Systems 3, Vol. 1, pp. 219-226, 1984

[23] L.C. Lang, *Modelling the Corrosion of Carbon Steel Feeder Pipes in CANDU Reactors*. Master's thesis, University of New Brunswick, Chemical Engineering Dept., 2000

[24] P. Phromwong, *Experimental and Modelling Study of Flow and Material Effects on Steel Corrosion Under Typical Power Plant Coolant Conditions*. PhD thesis, University of New Brunswick, Chemical Engineering Dept., 2013

[25] K.S. Venkateswarlu, *Water Chemistry: Industrial and Power Station Water Treatment*. New Delhi: New Age International (P) Ltd., 1996

[26] S.J. Zinkle, G.S. Was, *Materials Challenges in Nuclear Energy*. Acta Materialia No. 3, Vol. 61, pp. 735-758, 2013

[27] I. de Curieres, *The Evolution Of Chemistry In PWR Nuclear Power Plants: Overview And Safety Perspectives*. in Proceedings of Nuclear Plant Chemistry Conference, pp. 202-210, 2014

[28] S. Ranganath, D.W. Sandusky, T.L. Chapman, G.M. Gordon, E. Kiss, *Proactive Approaches to Assure the Structural Integrity of Boiling Water Reactor Components*. Nuclear Engineering and Design No. 1-2, Vol. 124, pp. 53-70, 1990

[29] *Enhanced CANDU 6 Technical Summary*. tech. rep., CANDU Energy Inc., 2012

[30] *Boiling Water Reactor Simulator with Passive Safety Systems*. tech rep., International Atomic Energy Agency, 2009

[31] D.M. Angrove, *Magnetitie: Structure, Properties, and Applications*. Nova Science Publishers, New York, 2011

[32] A.E. Regazzoni, G.A. Urrutia, M.A. Blesa, A.J.G. Maroto, *Some Observations on the Composition and Morphology of Synthetic Magnetites Obtained by Different Routes*. Journal of Inorganic and Nuclear Chemistry No. 7, Vol. 43, pp. 1489-1493, 1981

[33] T. Sugimoto, E. Matijevic, *Formation of Uniform Spherical Magnetite Particles by Crystallization from Ferrous Hydroxide Gels*. Journal of Colloid and Interface Science, Vol. 74, pp. 227-243, 1980

[34] E. Matijević, P. Scheiner, *Ferric Hydrous Oxide Sols: III. Preparation of Uniform Particles by Hydrolysis of Fe(III)-Chloride, -Nitrate, and -Perchlorate Solutions*. Journal of Colloid and Interface Science, No. 3, Vol. 63, pp. 274-277, 1978

[35] M. Basset *Deposition of Magnetite Particles onto Alloy-800 Steam Generator Tubes*. Master's Thesis, University of New Brunswick, Chemical Engineering Dept., 1998

[36] C. Lu, *Precipitation and Dissolution of Iron Oxide in High Temperature Water*. Master's Thesis, University of New Brunswick, Chemical Engineering Dept., 1998

[37] A. Iljinas, S. Tamulevičius, *Deposition of Fe_3O_4 Thin Films by Reactive Magnetron Sputtering and Solid State Reaction*. Materials Science No. 2, Vol. 14, pp. 110-114, 2008

[38] F.H. Sweeton, C.F. Baes Jr., *The Solubility of Magnetite and Hydrolysis of Ferrous Ion in Aqueous Solutions at Elevated Temperatures*. The Journal of Chemical Thermodynamics No. 4, Vol. 2, pp. 479-500, 1970

[39] P.R. Tremaine, C.J. Leblanc, *The Solubility of Magnetite and the Hydrolysis and Oxidation of Fe^{2+} in Water to 300˚C*. Journal of Solution Chemistry No. 6, Vol. 9, pp. 415–442, 1980

[40] P. Berge, C. Ribon, P.S. Paul, *Effect of Hydrogen on the Corrosion of Steels In High Temperature Water*. Corrosion No. 5, Vol. 33, pp. 403-414, 1977

[41] E.W. Thornton, *The Dissolution of Magnetite in 0.06 Molal Boric Acid Solution at Elevated Temperature*. in Proceedings of Coordinated Research Programme Meeting on Investigation of Fuel Element Cladding Interaction with Water Coolant in Power Reactors ander Topical Meeting on Water Chemistry in Nuclear Energy Systems, 1986

[42] M. McLaughlin, *Investigations of Corrosion-Product Behaviour Under a Variety of Nuclear Reactor Coolant Conditions*. Master's Thesis, University of New Brunswick, Chemical Engineering Dept., 2012

[43] D.T. Chin, C.H. Tsang, *Mass Transfer to an Impinging Jet Electrode*. Journal of the Electrochemical Society No. 9, Vol. 125, pp. 1461-1470, 1978

[44] K.L. Hsueh, D.T. Chin, *Mass Transfer of a Submerged Jet Impinging on a Cylindrical Surface*. Journal of the Electrochemical Society No. 9, Vol. 166, pp. 1845-1850, 1986

[45] D.T. Chin, K.L. Hsueh, *An Analysis Using the Chilton—Colburn Analogy for Mass Transfer to a Flat Surface from an Unsubmerged Impinging Jet*. Electrochimica Acta No. 5, Vol. 31, pp. 561-564, 1986

[46] H.M. Hofmann, M. Kind, H. Martin, *Measurements on Steady State Heat Transfer and Flow Structure and New Correlations for Heat and Mass Transfer*

in Submerged Impinging Jets. International Journal of Heat and Mass Transfer No. 19-20, Vol. 50, pp. 3957-3965, 2007

[47] IAPWS TGD8-16, *Technical Guidance Document: Application of Film Forming Amines in Fossil, Combined Cycle, and Biomass Power Plants*. IAPWS (International Association for the Properties of Water and Steam), 2016

[48] S. Odar, *Use of film forming amines (FFA) in nuclear power plants for lay-up and power operation*. Advanced Nuclear Technology International, 2017

[49] Framatome, *Film-Forming Amines: Corrosion Protection and Preservation of the Water-Steam Cycle*. Framatome, 2018

[50] C. Lertsurasakda, *Investigation of Flow-Accelerated Corrosion under Two-Phase Flow Conditions*. Doctor of Philosophy Thesis, University of New Brunswick, Chemical Engineering Dept., 2013

[51] P.R. Tremaine, J.C. Leblanc, *The solubility of nickel oxide and hydrolysis of Ni^{2+} in water to 573 K*. The Journal of Chemical Thermodynamics, Vol. 12, No. 6, pp. 521-538, 1980

[52] B. Sagot, G. Antonini, A. Christgen, F. Buron, *Jet impingement heat transfer on a flat plate at a constant wall temperature*. International Journal of Thermal Sciences No. 12, Vol. 47, pp. 1610-1619, 2008

[53] K. Sasaki, G.T. Burstein, *Erosion–corrosion of stainless steel under impingement by a fluid jet*. Corrosion Science No. 1, Vol. 49, pp. 92-102, 2007

[54] D. Lister, S. Uchida, *Reflections on FAC Mechanisms*. Power Plant Chemistry No. 10, Vol. 12, pp. 650-661, 2010

Appendix A

Mass Transfer Calculations

To calculate the mass transfer coefficient from the Sherwood number in Equation 2.18 a number of other parameters must be determeined first. It is assumed that Fe^{2+}, $Fe(OH)_2$, $Fe(OH)_3$, Fe_3O_4, FeO and Fe_2O_3 are all species begin transfered and an average Sherwood number was found. The dynamic viscosity of water at varying temperatures was calculated by using Equation A.1 [43].

$$\mu_W = 0.0168\rho_W t^{-0.88} \tag{A.1}$$

where μ_W is the dynamic viscosity (mPa·s or cP), t is the temperature (°C) and ρ_W is the density of water (kg/m^3).

The diffusivity of each oxide species can then be determined using the Siddiqi-Lucac correlation in Equation A.2.

$$D_{AW} = 2.98E-7\mu_W^{-1.026}V_A^{-0.5473}T \tag{A.2}$$

where D_{AW} is the diffusivity of species A in water (cm^2/s), V_A is the molar volume of species A (cm^3/mol) and T is the absolute temperature (K).

The Schmidt number was calculated for each species using Equation A.3, which could then be used to calculate the mass transfer rate coefficient in Equation A.4.

$$Sc = \frac{\mu_W}{\rho_W D_{AW}} \tag{A.3}$$

$$k_m = \frac{D_{AW} Sh}{d_0} \tag{A.4}$$

where d_0 is the 0.5 mm jet diameter.

A summary of the results for the mass transfer rate coefficient for each trial can be found in table A.1.

Table A.1: Average mass transfer coefficients for each run condition

Run No.	Temperature (°C)	Flow Rate (mL/s)	Re	Sh	k_m (mm/s)
1.2	140	1.89	22000	208	5.21
1.1	140	2.33	28000	243	6.15
2.2, 5	140	3	36000	293	7.43
1.3, 2.1, 3, 4	140	4	48000	364	9.22

Appendix B

Experimental Procedure

To measure the dissolution of magnetite with the use of the recirculating water loop the following steps must be followed:

- Fill the reservoir with de-ionized water.
- Saturate the ion-exchange with ammonia and flow de-ionized water through the ion exchange column until the pH is lower than the desired pH.
- Adjust the pH of the coolant with ammonia hydroxide and measure the pH with an Accumet Research AR20 pH/conductivity meter from Fisher Scientific.
- Begin to purge the reservoir with the desired purging gas to remove dissolved oxygen. This can take up to a week to remove all of the dissolved oxygen.
- Measure the dissolved oxygen with a CHEMets test kit to ensure low oxygen levels.
- Add any other chemicals to the loop, such as FFAs or hydrazine, to the loop via the rubber septum.

- Prepare the magnetite oxide pellet by wrapping it with Teflon tape to ensure a tight fit when fitting the pellet in the Teflon holder in the impinging jet test section.

- Loop 2: Gradually increase the loop heater to roughly 150°C and check for any leaks that can occur within the loop. A rope heater will be used for a precise temperature at the test section as heat loss occurs between the heater and test section.

  Loop 3: Gradually increase the pre-heater to 60°C and the main heater to roughly 150°C and check for any leaks that can occur within the loop.

- Ensure the cooling water is turned on for the coolant to return to room temperature.

- Loop 2: Set the loop pressure via the pressure relief valve to ensure the coolant does not boil at the set temperature.

  Loop 3: Set the loop pressure via the back-pressure regulator to ensure the coolant does not boil at the set temperature.

- Vacuum the test section to remove any oxygen that can be introduced to the system. Open the inlet and outlet valves to the test section before closing the bypass line.

- Loop 2: Adjust the power to the rope heater with the variable autotransformer to ensure the temperature is 140°C at the test section.

- Check the pH, oxygen, conductivity and temperature of the coolant periodically during the run.

- Open the test section bypass line and close the inlet/outlet valves when the

run is finished. Allow the test section to cool down and remove the test section from the loop. Argon is used to dry the magnetite sample.

- Analyze the magnetite sample with Raman, SEM and profilometry techniques.

One magnetite pellet can be used for multiple runs if the surface dissolution is only minor and can be removed by polishing. The surface should be examined with SEM and Raman to ensure the surface dissolution or any precipitates are removed.

Appendix C

Modeling Erosion Matlab Program

The following code was written in Matlab to determine the effect of erosion on removing the grains from poorly sintered magnetite pellets.

```
format long
clc
clear all
%(Constants at 140C and pH 9.2)
koverall=0.685; %(Overall measured removal rate constant cm/s)
kd = 0.003; %( Dissolution rate constant cm/s)
C = 13E-9; %( Solubility gfe/cm 3)
a = 0.1E-4; %(minimum of particle diameter cm)
b = 5E-4; %(maximum of particle diameter cm)
ta=1397; %(average shear stress over the crater area pa)
texp= 504*3600; %(total time of the experiment s)
ro=5.2; %(density of the magnetite g/cm3)
f=167.5/231.5; %(converting factor g magnetite to g iron)
r= 0.06; %(radius of crater cm)
```

```
area= pi*r^2; %(area of crater cm2)
t=0;
delx = a;
x = [a:delx:b]; %(creates matrix of particle sizes from a-b)

d = randsample(x,10*504*3600,true, normpdf(x,a,(b-a)/3)); %(generating
pdfd = normpdf(x,a,(b-a)/3); %(freq / sum(freq) / (bin(2)-bin(1)));
pdfd = pdfd / sum(pdfd) / delx;
d20 = sqrt(sum(pdfd.*x.^2)* delx);
d30 = (sum(pdfd .* x.^3) * delx)^(1/3);
d32 = d30^3 / d20^2;
g = (pi * d32 * ro * f * ta * kd) / ((koverall - kd)*area*6) %(Constant
N = texp*ta*kd*C/(g*d20^2) %( Number of particles removed)
%(volume and thickness of particles removed at 1 s intervals)
j=0;
ttotal=0;
n=0;
while ttotal < 1080000 %(Removal of particles for entire experiment)
j=j+1;
tloop=0;
thick=0;
i=n;
while tloop < 1 %(Removal of particle in 1 second interval)
i=i+1;
thick=thick+pi*d(i)^3/(6*area);
tloop=tloop+g*d(i)^2/(ta*kd*C);
```

```
end
T(j)=tloop;
ttotal=tloop+ttotal;
V(j)=thick;
n=i;
end
%(accumulation of thickness removal)
for i=1:j
S=0;
for k=1:i
S=V(k)+S;
end
G(i)=S; %(Thickness of removed material)
end
```

Vita

MScE Candidate:

Aaron James Turner

University attended:

2017-2019 MScE Chemicall Engineering, University of New Brunswick

2013-2017 BSc Mechanical Engineering, University of New Brunswick

Publications:

D.H. Lister, A. Turner, S. Weerakul, *Effects of Oxide Dissolution on Material Transport in Reactor Coolant Systems.* IAEA Technical Workshop, CANDU Owners Group Offices, Toronto, Canada, November 25-28, 2019